FLOW FIELD AND LOADING ANALYSIS
ON A WRAP-AROUND FIN MISSILE

THESIS

Thomas C. McIntyre
Second Lieutenant, USAF

AFIT/GAE/ENY/97D-04

19980210 031

Disclaimer

The views expressed in this thesis are those of the author and do not reflect the official policy or position of the United States Air Force, the Department of Defense, or the United States Government.

FLOW FIELD AND LOADING ANALYSIS ON A WRAP-AROUND FIN MISSILE

THESIS

Presented to the Faculty of the Graduate School of Engineering

of the Air Force Institute of Technology

Air University

Air Education and Training Command

In Partial Fulfillment of the Requirements for the

Degree of Master of Science in Aeronautical Engineering

Thomas C. McIntyre, B.S.

Second Lieutenant, USAF

December 1997

AFIT/GAE/ENY/97D-04

FLOW FIELD AND LOADING ANALYSIS ON A WRAP-AROUND FIN MISSILE
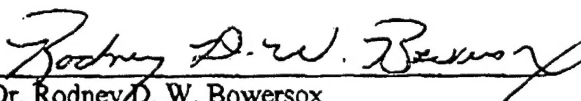
Thomas C. McIntyre

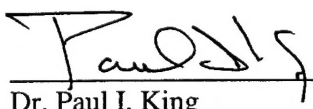### Second Lieutenant, USAF

Approved:

_____

Major Jeffery K. Little
Committee Chairman

3 Dec. 97
Date

_____

Dr. Rodney D. W. Bowersox
Committee member

1 Dec '97
Date

_____

Dr. Paul I. King
Committee member

12/3/97
Date

Dedication

This work is dedicated to the memory of Dave Driscoll. His work at the AFIT model shop

helped many students, including myself.

Acknowledgments

Table Of Contents

List of Figures

List of Tables

List of Symbols

English Symbols

Symbol	Definition
C_l	TSP calibration constant
C_L	Rolling moment coefficient
c_p	Specific heat at constant pressure
c_v	Specific heat at constant volume
d	Missile diameter
dx	Pixel width
dy	Pixel height
F	Force due to pressure
i	Pixel column marker
I	Pixel luminescence
I_0	Pixel reference luminescence
I_{ref}	Pixel luminescence at T_{ref}
j	Pixel row marker
k	Sequential image marker
K_q	Stern-Volmer constant
L	Rolling moment
l	Length of actual fin surface covered by pixel depth
M	Mach number
P	Pressure
P_{O_2}	Partial pressure of oxygen

q	Dynamic pressure
R	Universal gas constant
Re	Reynolds number
r	Radius to pixel location
T	Temperature
T_{ref}	Reference temperature
V	Velocity

Greek Symbols

Symbol	Definition
α	Angle of Attack
γ	Ratio of specific heats, c_p/c_v
ε	Percentage error of a given quantity
μ	Dynamic viscosity of air, angle of fin curvature
ρ	Density

Subscripts

Symbol	Definition
∞	Free stream quantity
c	Fin chord, used as a length reference
d	Missile diameter, used as a length reference
error	Error quantity for a given variable
fit	Variable that has been curve-fitted
i	X-coordinate location

imax	Image pixel width, in integers
j	Y-coordinate location
jmax	Image pixel depth, in integers
meas	Variable measured directly
t	Free stream total quantity, tangential component

Abbreviations

Abbreviation	Definition
AEDC	Arnold Engineering Development Center
AFIT	Air Force Institute of Technology
ARF	Aeroballistics Research Facility
CCD	Charge-Coupled Device
CFD	Computational Fluid Dynamics
DCAT	Direction-Controlled Anti-tank
MLRS	Multiple Launch Rocket System
PSP	Pressure-Sensitive Paint
PtOEP	Platinum octaethylporphyrin
TSP	Temperature-Sensitive Paint
VMT	Variable Mach Tunnel
WAF	Wrap-Around Fin
YAG	Yttrium aluminum garnet

Abstract

Wrap-around fin (WAF) missiles offer packaging benefits but experience rolling moments due to the curved fin design. Rolling moments stabilize unguided projectiles, but cause guidance and control problems for future guided applications. Understanding the flow field in the vicinity of the fins is critical to future missiles. Fin pressure profiles were characterized with pressure-sensitive paint. Two rectangular four-fin constructions were tested—one solid and one with a rectangular hole (slotted fin). Static pressure data were divided by free-stream total pressure for presentation. Tests were conducted at Mach numbers of 2.15, 2.28, 2.41, 2.86, 3.25, 3.50 and 3.83. Reynolds numbers based on missile diameter ranged from 4.0×10^6 to 1.3×10^7. Mach 2.86 pressure profiles on the solid fin were compared to computational fluid dynamic (CFD) predictions on a single wall-mounted fin. The four-fin model pressure distributions agreed with CFD, verifying that a single wall-mounted fin captures relevant WAF aerodynamics. Slotted fin pressure profiles were similar to solid fin profiles, except in the vicinity of the slot.

Schlieren photography and oil flow visualization supplemented pressure data, providing velocity information on the WAF surface and revealing density gradients in the fin region. All measurement techniques verified CFD predictions of flow field aerodynamics about a single fin.

This testing assumed that pressure observations made in the fin region were creating rolling moments magnitudes observed in other experimental testing. In order to confirm this, pressure sensitive paint images were edited for fin data only, saved as text matrices, and integrated with computer code to derive rolling moments and rolling moment coefficients. Solid fin data confirmed negative rolling moment magnitudes and roll-off rates measured in past experiments and in CFD predictions. Slotted fin rolling moment coefficients were slightly larger than solid fin results because of the larger fin area.

FLOW FIELD AND LOADING ANALYSIS ON A WRAP-AROUND FIN MISSILE

Chapter 1 - Introduction

1.1 Background

Wrap-around fin (WAF) missiles have been studied extensively, largely because of the packaging advantages they offer. Curved fins are wrapped around the missile body during storage, using considerably less space than traditional missile fins. Upon deployment, fins lock into position using a spring mechanism. The advent of stealth technology has made these cylindrical projectiles desirable, since internal missile storage would reduce an aircraft radar cross-sectional signature. But certain aerodynamic qualities of WAF missiles must be controlled before this type of armament can become a potential guided missile.

The rolling moment generated by WAF missiles presents the largest guidance and control problem for these projectiles. At subsonic velocities and zero angle of attack, rolling moment is positive. The missile rolls toward the convex side of the fin, the side that is exposed when fins are wrapped around the body. A rolling moment reversal occurs at Mach 1.0, as pressure distributions change in the fin region. At supersonic velocities, rolling moment is negative—the missile rolls toward the concave, or cupped, side of the fin. Characterizing the aerodynamics in the fin region of a WAF is the first step for controlling future missile applications.

While rolling moment is a source of the WAF control problem, it also provides a source of stability that has resulted in the proliferation of unguided WAF rockets. Rolling motion generated by the fin region results in inertial stability when the missile is constructed properly. Proper construction has been a large subject of investigation in unguided WAF rocket history.

1

1.2 Previous WAF Research

Exhaustive WAF missile research began in the early 1970s, when the U. S. Army Missile Command, Redstone Arsenal, funded investigations of WAF projectiles at the U. S. Air Force Arnold Engineering Development Center (AEDC). The study by Dahlke [9] focused on a four-fin model with varying fin configurations at Mach numbers of 0.3 to 1.3. This study yielded force and moment data in all three coordinate axes. Basic research took years for the Army to complete. As late as 1983, rockets with combinations of WAFs and straight fins were being tested by the Redstone Arsenal [33]. The U. S. Naval Ordnance Laboratory also had a great interest in WAF projectiles. Naval WAF research was motivated by the tube-launched, sea-going possibilities of WAFs. Early naval studies were conducted at the Massachusetts Institute of Technology, utilizing a WAF rocket at Mach 4.25 [32]. Studies by Regan were conducted on a 10-caliber spinner projectile, which yielded magnus force and moment data, normal forces, and pitching moment data [21]. Naval research continued at the Naval Surface Weapons Centers' Dahlgren Laboratory. Incompressible wind tunnel testing was conducted at angles of attack ranging from 0 to 90 degrees [10].

Basic WAF research was not limited to the United States. The Australian Defense Scientific Service (Weapons Research Establishment) conducted small angle of attack testing from Mach 0.5 to 2.4. Rolling moment reductions were made on models designed at Eglin AFB, by modifying the manner in which fins deploy, which had a degradation on static stability [22]. The problem uncovered by the Australians was a cause-and-effect relationship between rolling moment and pitch stability. This roll-pitch coupling has been a major issue in WAF research. Even recently, numeric studies have been conducted by the Aligarh Muslim University in India, in order to capture the roll-pitch coupling of WAF projectiles [5].

Once the basic research of the 1970s had resolved aerodynamic characteristics of general WAF behavior, real-world applications began to take form. The Redstone Arsenal funded tests on two

WAF-controlled rockets. The shoulder-fired Direction-Controlled Antitank (DCAT) missile was tested in AEDC wind tunnels at Mach numbers ranging from Mach 0.64 to 2.5. The tests measured side force and normal force coefficients for varying yaw and pitch angles, employing both a wrap-around fin and a straight fin as potential stability surfaces [16]. The AVCO Assault Breaker model was also tested at AEDC over a Mach number range of 0.6 to 1.3, and at angle of attack variations of -4 to 27 degrees [14]. The Mark IV WAF rocket resulted from initial Australian testing. This six-finned configuration was later tested on a ballistic range, using a 384 mm gas gun [20]. The widest use of WAF rockets has appeared in the U. S. Army Multiple Launch Rocket System (MLRS). A recent study at AEDC found drag coefficient variations due to production variations in MLRS fin thickness, roughness, and overall geometry [6].

The U. S. Army has been conducting advanced WAF research at the Aberdeen Proving Ground in Maryland [17]. Roll damping effects were studied for projectiles with straight and curved fins. Semi-empirical roll damping curve fits were found for different fin configurations. The advent of computational fluid dynamics (CFD) permitted rolling moment calculations which could be compared to experimental data. Three-dimensional, Navier-Stokes codes characterized WAF projectile behavior at Mach 1.3 to 3.0 and compared data to AEDC and NASA experimentation results, showing relatively good agreement [12].

In the late 1980s the U. S. Air Force became interested in the possibility of a guided WAF missile. The Wright Laboratory Armament Directorate began a series of studies which investigated a generic WAF construction in free-flight tests [34]. CFD made it possible to compare aerodynamic characteristics to ballistic data, which were recorded at the Aeroballistic Research Facility at Eglin AFB. Comparisons for a generic WAF model were made for Mach numbers of 2.75 to 5.15 [31]. This preliminary research led to efforts that considered different missile body and fin configurations [27] and base cavity models [2]. Different fin deployment systems, for both straight and curved

3

fins, were considered and tested in free-flight and with CFD [4]. Rectangular holes were placed in the regular solid fin models (slotted fins), in order to reduce rolling moments [3]. The slotted fin models tested in the Aeroballistic Research Facility did not display the characteristic rolling moment reversal at Mach 1.0. Rolling motion was always negative, or in the direction of fin curvature, which would simplify control requirements for an air-to-air guided missile.

With the exception of CFD, previous testing failed to capture the relevant aerodynamics that caused the unique behavior of WAF projectiles. The behavior of various missile geometries has been investigated, but no data was taken to examine flow field characteristics. Under sponsorship by the Wright Laboratory Armament Directorate, the Air Force Institute of Technology (AFIT) began conducting WAF flow field analyses about a single fin. Studies examined the fin experimentally [15] and numerically [29] at Mach 2.8. CFD studies were also conducted on the fin from Mach 2.5 to 5.0, and experimentally at Mach 4.9 [28]. The AFIT studies assumed that a single WAF captures the relevant aerodynamics of a full, three-dimensional model. This assumption was never verified experimentally. Also, while pressure data were found using CFD, determination of WAF pressure profiles were not performed experimentally prior to the current research.

1.3 Flow Field Description

The testing conducted at AFIT characterized the flow field about a single wall-mounted WAF at Mach 2.9 and Mach 4.9, both experimentally and numerically [15, 28]. This section summarizes the qualitative results of these tests. The flow field was similar for both Mach numbers, only in varying degrees of strength. According to the experimental and numerical data, the fin is preceded by a detached shock wave, which forms a lamda shock at the fin-body intersection. The shock is stronger on the convex side, and more oblique on the concave side.

On the concave side of the fin, an expansion region follows the detached shock. Fin curvature causes flow compression immediately following the expansion region. As flow continues down the fin, velocity patterns diverge from the center of the fin. Numerical methods suggest a strong triangular section of high pressure centered on the fin.

On the convex side of the fin, flow passes through the more normal portion of the detached shock. The convex fin curvature results in a strong expansion region, or favorable pressure gradient. This pressure region was also triangular in shape, centered on the fin. The most unique feature of the convex side is a vortex formed at the fin-body intersection. The vortex lies close to the lower portion of the fin, causing higher pressures as it proceeds downstream, increasing in size and strength.

1.4 Problem Statement and Research Goals

There were several areas in WAF research that needed to be explored by the current work. In addition to the solid fin rolling moment reversal at Mach 1.0, other studies have suggested that another rolling reversal may exist in the Mach 4.0-5.0 range [15,31]. The possibility of these trends was a concern in the current WAF studies. Also, the previous AFIT studies required validation of the single-fin assumption. Slotted fin aerodynamics had not been researched in detail. Experimental and CFD pressure data for this fin are not present in any of the historical works mentioned. Rolling moment data and flow field characteristics were not published in the few slotted-fin papers available.

The gaps in WAF aerodynamics were to be filled with the present research. Specifically, there were five primary goals to be solved by experimentation. First, continuous pressure data was to be obtained on both solid and slotted three-dimensional WAF models. Second, an analysis was to be performed on the major flow field characteristics on the three-dimensional models, and compared to single-fin results. Also, qualitative velocity information was required on fin surfaces for both solid and slotted three-dimensional models. Next, using pressure data, rolling moment information

5

was needed for both solid and slotted fin models. Comparisons would be made with past data where possible. Finally, all testing needed to be conducted over the largest Mach range possible, at zero angle of attack.

The means to accomplish these goals was possible with the aid of the Wright Laboratory Armament Directorate, under Air Force Contract F33610-90-C-2507.

1.5 Summary of Research Method

Continuous pressure data in the fin region could not have been found experimentally without pressure-sensitive paint (PSP) technology. Traditional static pressure taps and transducers would permit approximately twenty data points on each side of the fin. This would require two fin models to be constructed, with pressure tubes exiting the fin surface not being tested. But when used with a charge-coupled device (CCD) camera, PSP emissions yield data with resolution as fine as the CCD camera will permit, using only one wind tunnel model. Pressure data were therefore obtained using the PSP method and were compared to the CFD single-fin model of Reference [28]. PSP theory and associated calibration requirements are described in detail in Chapter 2.

Flow field analysis, the second research goal, was possible through PSP data, surface oil flow visualization, and schlieren photography. Streaks of high and low pressure, coupled with oil separations and streaks, were used to determine flow field phenomenon adjacent to the fin surface. Oil flow visualization also provided qualitative velocity information on the WAF models, which was compared to CFD velocity profiles of a single fin. Schlieren images verified shock locations and vortex structures.

Pressure data from PSP images were integrated across each side of the fins to extract rolling moments and roll moment coefficients. Images consisted of large ASCII text matrices of data, which were edited for fin data only. These edited files were used for rolling moment calculations. The key

6

assumption made in this analysis was that shear forces created negligible rolling moments. Rolling moment data for both solid and slotted fin models were obtained. Solid fin rolling moment data were compared to CFD estimates in Reference [28]. The limited availability of slotted fin rolling moment data prevented comparison of these data.

PSP, schlieren, and oil flow data are only as good as the camera resolution used to capture data. In the present work, this characteristic became very important when considering the entire length of the WAF missile. While the fin region generates the anomalous behavior of WAF missiles, it takes up a very small portion of the total missile volume. Images capturing the entire length of the missile present poor resolution with limited data points in the fin region. This resolution issue may be viewed in Figures 1 and 2, which show characteristic schlieren and PSP images, respectively. Both convey a great deal of information about the missile body, which is of little interest at zero angle of attack. In these images, little information is revealed in the fin region, the primary region of interest. As a result, the nose and central fuselage were ignored, and all data was taken in the vicinity of the fins only.

Figure 1. Schlieren Image
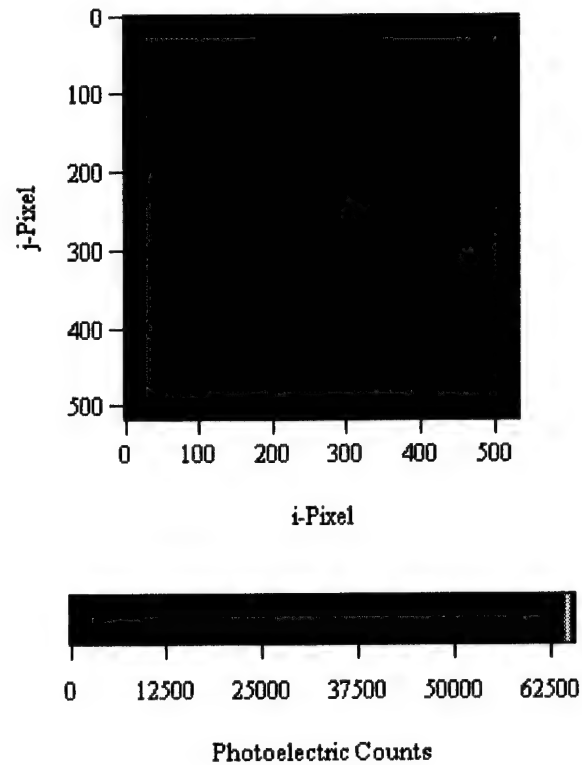
Figure 2. Raw PSP Image

The following chapters all deal intensively with the data recording and analysis. Chapter 2 describes the equipment used, PSP method and theory, and details of the schlieren and oil flow methods. Chapter 3 presents the results of PSP testing and rolling moment analysis, schlieren, and oil flow data, along with a flow field analysis. Conclusions and recommendations are summarized in Chapter 4.

Chapter 2 - Experimental Methodology

2.1 WAF Models

Two WAF models were supplied by the Wright Laboratory Armament Directorate for primary testing. These models were previously fabricated for use in the Aeroballistics Research Facility (ARF), Eglin AFB, a free-flight analysis laboratory. The AFIT model shop mounted each missile with a sting support and placed static pressure ports for PSP confirmation. The fuselage was composed of aluminum, and the nose cone and fins were constructed of steel. Models dimensions are presented in Figures 3 and 4. A photograph of both models follows this in Figure 5.

Each three-dimensional model had a missile diameter of 1.91 cm, which was used for scaling all other model dimensions. Each model, with a length of 19.1 cm, had a fin with 45 degree beveled leading and tip edges. The first model, using the traditional WAF style, had a fin that was completely solid in nature. The second had a rectangular hole, or slot, cut into the center of the fin. An important consideration in comparing each model is that the chord lengths are not identical, while every other dimension matches. The solid fin has a chord length of 1.02 cm, whereas the slotted fin chord length measures 1.46 cm.
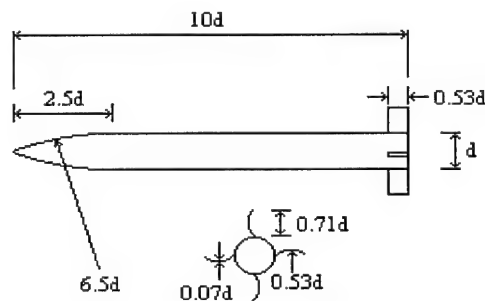
Figure 3. Solid Fin Model

9
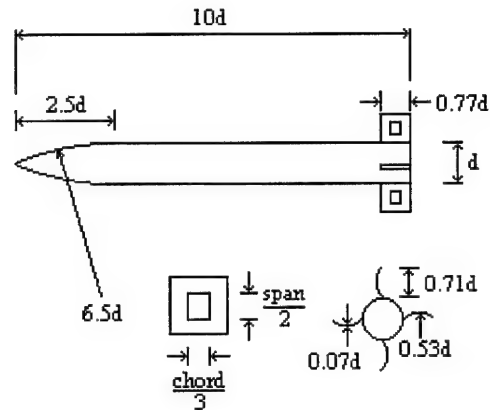
Figure 4. Slotted Fin Model
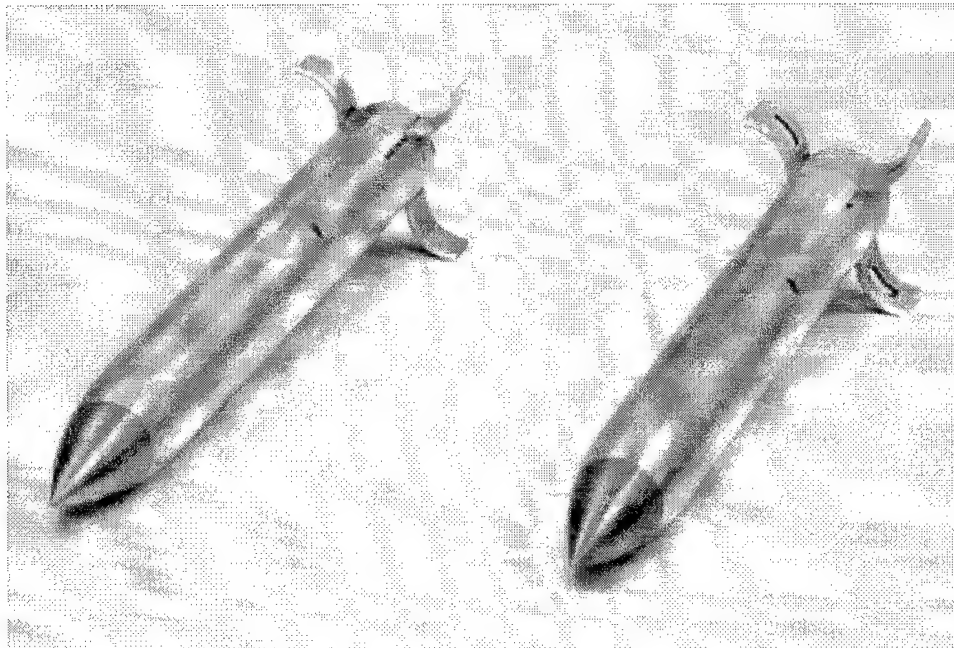
Figure 5. Both WAF Models

The third model tested was obtained from previous research efforts at AFIT [28]. The aluminum model consisted of a solitary fin on a 1.59 cm cylinder body. The cylinder body blended into a wall mount over a length of 7.95 cm. The fin had a chord length of 2.03 cm, or 0.64 body diameters (d). It also had leading and tip edges beveled at 45 degree angles. A schematic of the model is presented in Figure 6. A photograph of the model may be viewed in Figure 7. The model

was designed for the smaller AFIT Mach 2.9 wind tunnel. A primary goal in this fin design was to obtain the largest possible fin for study without creating tunnel blockage.
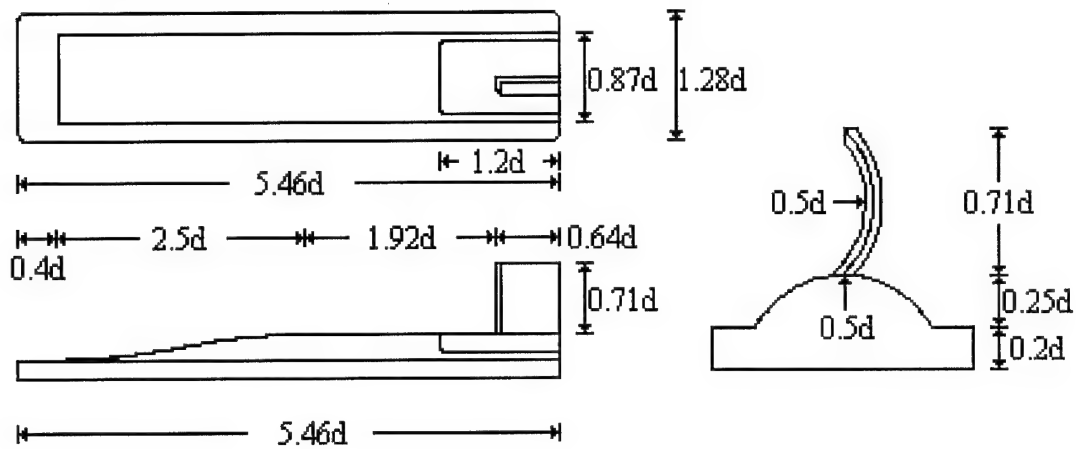
Figure 6. Wall-Mounted Fin Schematic
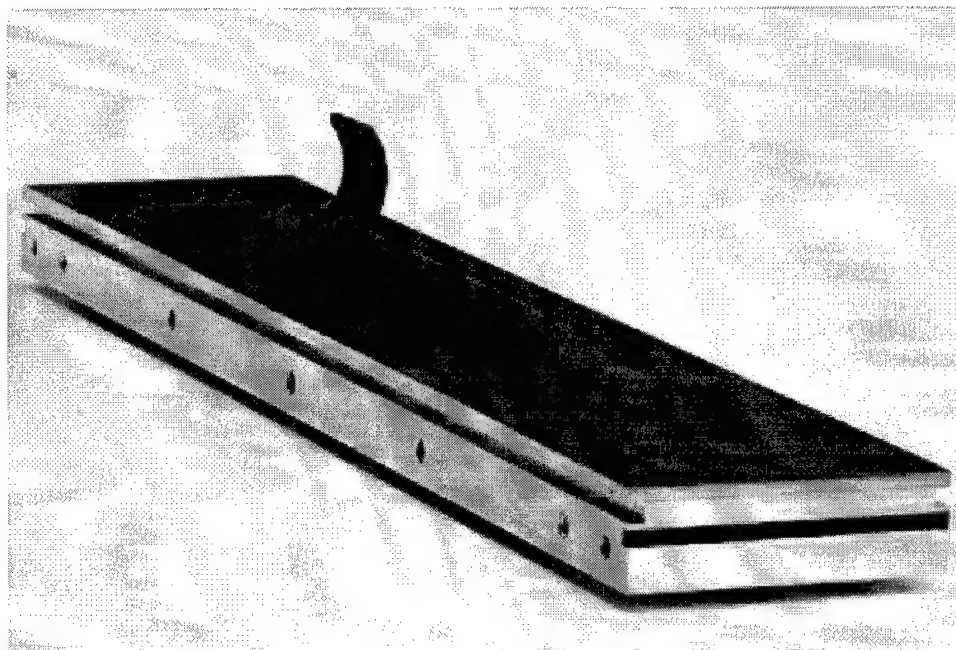
Figure 7. Single-Fin Model

11

2.2 AFIT Variable Mach Wind Tunnel

The three-dimensional WAF configurations were tested in the AFIT Variable Mach Wind Tunnel (VMT). This blow-down facility exhausts directly to atmosphere. The test section is 54.61 cm long with a square 15.24 cm cross-section. The 22.65 m^3 air supply reservoir limits testing times to 40 seconds or less, depending on Mach settings. The throat size and Mach setting are adjusted by sliding a nozzle block into the desired location. Tunnel total pressure variation is adjusted with a 15.24 cm butterfly valve, powered by a 6,895 kPa hydraulic pump. Valve position is controlled with a feedback servo system, adjusted for desired tunnel stagnation pressure. The supply reservoir is recharged with two 37.28 kW compressors, accompanied by two desiccant-type air dryers. The compressors took approximately 45 minutes to recharge a completely empty reservoir. A tunnel diagram may be viewed in Figure 8. This is followed by a photograph of the tunnel stagnation tank and test section, Figure 9. In the image, air flows from right to left.

WAF models were mounted in the center of the test section at zero angle of attack. The oblique shock created by the nose of each model reflected off of the test section walls and would potentially impinge on the model downstream. Early schlieren testing indicated that Mach 2.15 was the lowest setting at which models could be tested without shock impingement on the fins. Higher Mach settings resulted in impingements further downstream, outside of the field of interest.
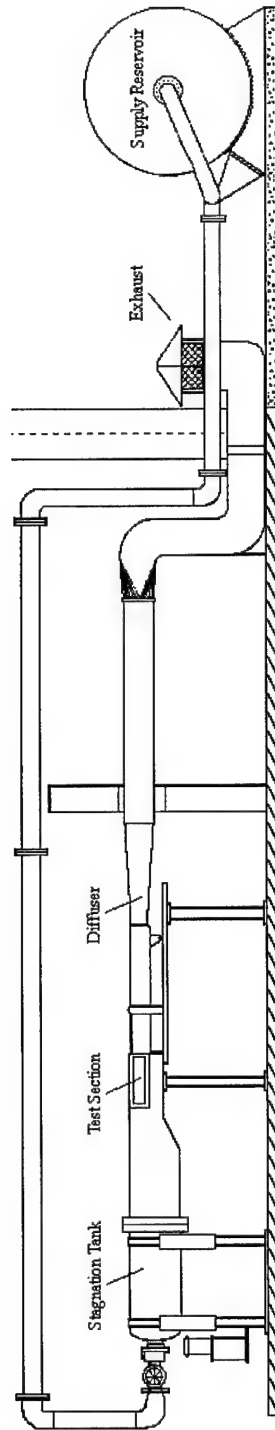
Figure 8. AFIT Variable Mach Wind Tunnel
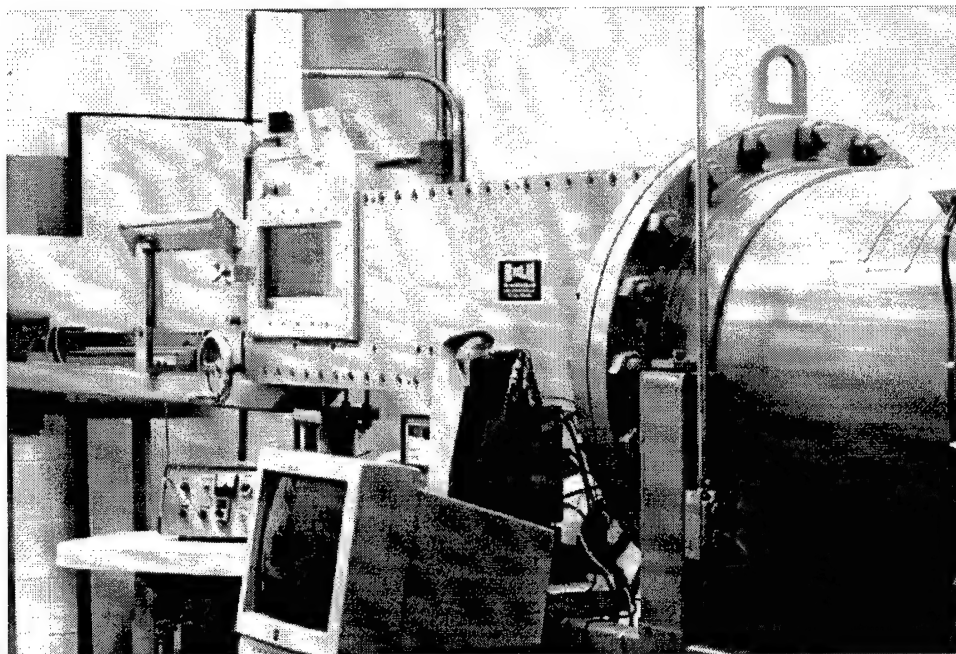
Figure 9. AFIT VMT Test Section

2.3 AFIT Mach 2.9 Wind Tunnel

The AFIT Mach 2.9 Wind Tunnel was used solely for testing the wall-mounted WAF model. This tunnel is also blow-down in nature, but with downstream evacuation. The test section is 33.0 cm long with a square 6.35 cm cross-section. The evacuation reservoir limits test times to 30 seconds or less, depending on the stagnation pressure selected. Supply air is provided by AFIT building compressors. The 7.46 kW evacuation pump requires 5 minutes to empty the evacuation reservoir. A schematic and photograph of the tunnel may be viewed in Figures 10 and 11. The WAF model was mounted on the Test Section 1 ceiling during testing.
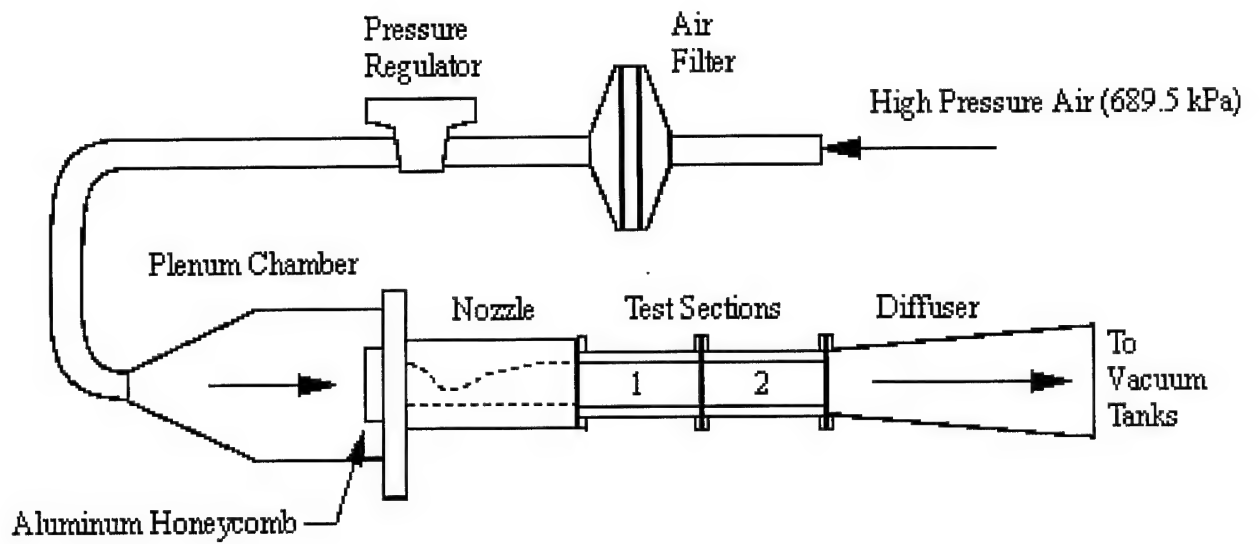
Figure 10. AFIT Mach 2.9 Wind Tunnel Schematic
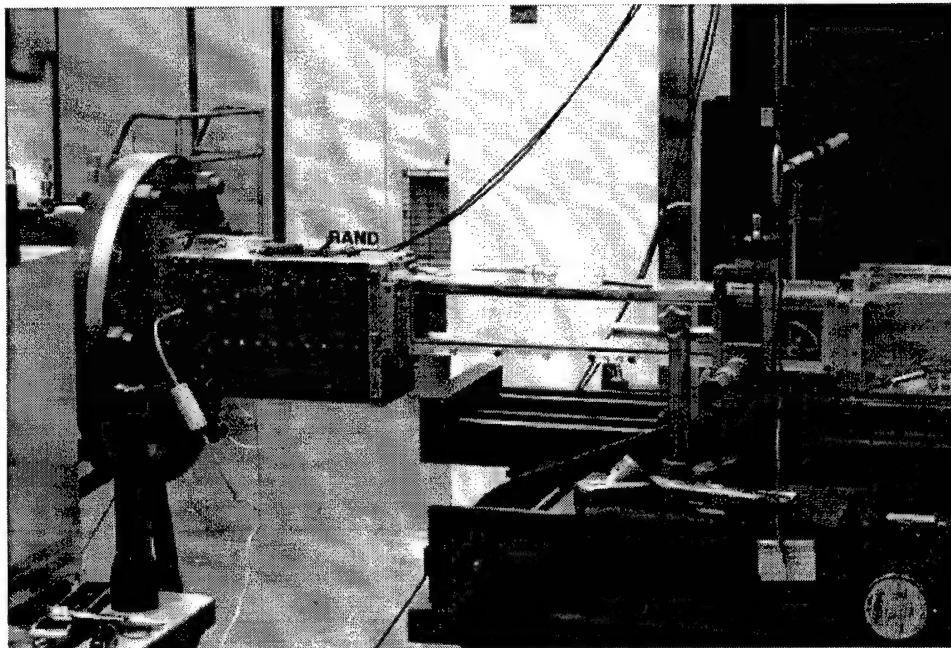
Figure 11. AFIT Mach 2.9 Wind Tunnel

2.4 Tunnel Instrumentation

Free-stream pressure data was essential when non-dimensionalizing data for comparison with past results. Free-stream total and static pressures were recorded in both the VMT and Mach 2.9 tunnel, each tunnel using a slightly different setup. In the VMT, total pressure was recorded in the plenum, or stagnation tank. Static pressure was recorded in the test section, at approximately half of the missile length (schlieren testing assured that shocks were not reflecting prior to the pressure port). The total pressure tap was connected to an Endevco 3,447.3 kPa gauge pressure transducer (maximum rated pressure). The static pressure port was connected to an Endevco 103.4 kPa absolute pressure transducer. Each transducer was connected to an Endevco model 4428A voltage amplifier, which contains a Wheatstone bridge circuit for interpreting transducer voltage changes. The total pressure bridge was calibrated with a hand-held Amtek T-740 pneumatic tester to within ± 2.068 kPa. The static pressure bridge was calibrated with an MKS (NGS Division) Type PVS-6 Portable Calibration System to within ± 0.3447 kPa. Total temperatures were also recorded in the stagnation tank using an Omega thermocouple and an Omega P2 cable connector, which contains the bridge circuit.

The VMT pressure transducers and thermocouple were connected to a National Instruments AT-MIO-16 12-bit successive approximation analog-to-digital (A/D) board. The board sent digitized data to an Intel 486 processor, using the Labview computer program, version 3.1.1. Data were recorded during runs at 2 Hz, yielding a data point every 0.5 s, which matched the camera shutter speed. Ambient pressures, which would be helpful in PSP measurements, were recorded from a Druck DPI 141 Resonant Sensor Barometer, with an error of ± 0.169 Pa.

The Mach 2.9 tunnel had a much simpler instrumentation setup. A total pressure port in the plenum chamber and a static pressure port in the test section (ahead of the wall-mounted WAF model) were connected to Endevco 344.7 kPa gauge pressure transducers. The transducers were connected

16

to Endevco model 4428A voltage amplifiers, which were calibrated to read pressure data. Because the operating conditions of this tunnel were more stable, pressures were simply read and recorded during the test, with a variation of ± 0.689 kPa. Plenum total temperature was also recorded visually, using an Omega thermocouple and an Omega P2 cable connector.

2.5 PSP Technique

2.5.1 Theory

PSP technology has been well-documented and is becoming an important measurement tool in experimentation [11, 13, 18, 19, 30]. This non-intrusive measurement technique achieves nearly-continuous pressure data collection over a surface. Measurements are based upon the phenomenon of photoluminescence, a combination of fluorescence and phosphorescence. The details of this technique are provided in this section.

Probe molecules, sensitive to both pressure and temperature, are embedded in a binder and applied to the surface of the test object. The molecules are illuminated by a high-energy, short wavelength of light, thus exciting them to a higher state. When ignoring temperature effects, the excited probe molecule then returns to the ground state in one of two ways. First, the molecule may simply emit a lower-energy photon. Second, if an oxygen molecule is present, it will return to the ground state by collisional deactivation. Energy is transferred to the oxygen when it collides with the probe molecule, and is then carried downstream out of the field of interest. The partial pressure of oxygen in the airflow determines how many collisions will occur. This oxygen-quenching phenomenon can be modeled with the Stern-Volmer relationship [19]:

$$\frac{I_0}{I} = 1 + K_q P_{O_2} \tag{1}$$

where I is the luminescence, I_0 is the luminescence in the absence of oxygen, K_q is the Stern-Volmer constant, and P_{O_2} is the partial pressure of oxygen. Variations in temperature affect both I_0 and K_q.

17

A third way that probe molecules may return to their ground state is through energy transfer within the binder material. The molecular free volume within the binder is dependent on temperature. Changes in temperature result in free volume changes, which affect energy transfer of the probe molecules to the binder. This, in turn, affects the luminescence of a probe molecule. Temperature changes can be modeled with the relation:

$$T = T_{ref} + C_l \ln \left(\frac{I_{ref}}{I} \right) \tag{2}$$

where T is temperature, T_{ref} is a reference temperature, C_l is a calibration constant, I_{ref} is the luminescence at T_{ref}, and I is luminescence [18]. This equation is the basis for temperature-sensitive paints. All pressure-sensitive paints are temperature-sensitive to a small degree, however, and follow the characteristics of this equation.

2.5.2 Experimental Procedure

The Stern-Volmer equation was applied by taking images at a reference pressure condition (ambient pressure or "air off") and at the test condition ("air on"). The ratio of the two images was the basis for pressure determination, when matched against a calibration curve. The ratio process accounts for angularity variations over the surface of the test subject. A background noise image was also taken, with excitation light turned off. This image was subtracted from both "air off" and "air on" images.

Calibration was achieved by painting a square aluminum plate with probe molecules, placing this in a pressure chamber with a window to allow image acquisition, and subjecting it to pressures ranging from 5.0 to 105.0 kPa at room temperature. Images were taken at ambient pressure and at each test pressure, and ratioed. Air pressure was maintained with a Druck DPI500 Digital Pressure Controller. The pump used to supply the controller was a Welch DuoSeal Vacuum Pump (model 1402). This calibration curve may be viewed in Figure 12. A correlation coefficient of 0.999 was

18

drawn between calibration points and the curve fit seen in this figure. When calibrating wind tunnel data, however, the atmospheric pressure during the test differed slightly from the atmospheric pressure recorded during calibration. This difference in ambient pressures was taken into account with the aid of the reduction code PSP.EXE, whose algorithm may be viewed in Appendix A. The code simply changes the reference intensity, I_0 which corresponds to current atmospheric pressure.
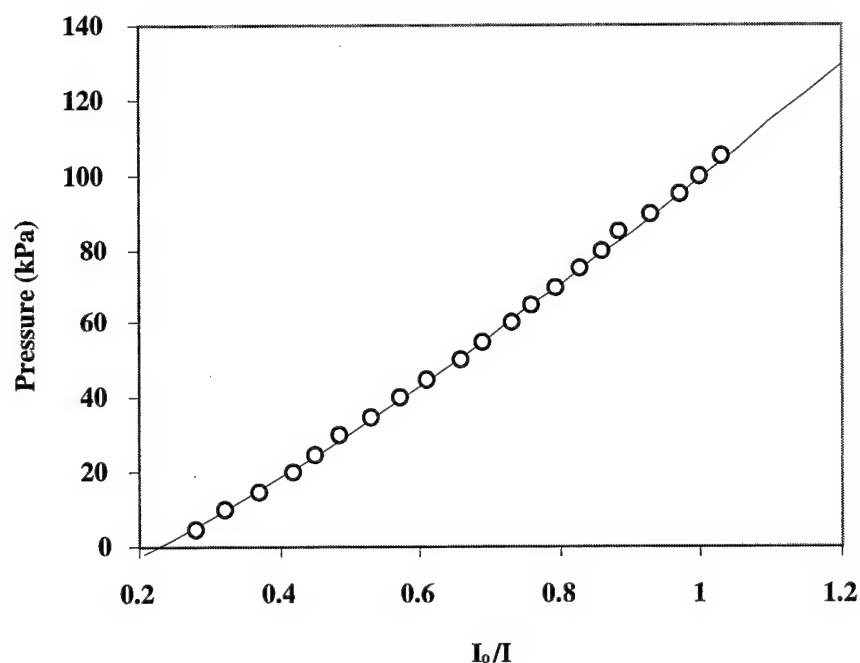
Figure 12. PtOEP Pressure Calibration

The probe molecule used in the current research was platinum octaethylporphyrin (PtOEP). Though PtOEP displays temperature sensitivities, the 12-second testing times and 30-minute minimum tunnel recharge periods prevented missile surfaces from cooling excessively. Though many different probe molecules exist for pressure- and temperature-sensitive paints, this one was chosen because of the wind tunnel windows. Because they are made of glass, only visible spectrum emis-

19

sions and excitation waves are readily permissible. Other probe molecules, such as pyrene, emit radiation in the ultraviolet range, which does not pass through ordinary glass [13].

PtOEP molecules were pioneered at the Air Force Arnold Engineering Development Center (AEDC) for use in the AEDC Propulsion Wind Tunnel [24–26]. The maximum excitation wavelengths of PtOEP are at 380 and 540 nm, with red emissions at 650 nm. Probe molecules were diluted in toluene such that the mixture was saturated. All models, including the calibration plate, were coated with a primer layer of flat white Krylon titanium dioxide paint. The primer layer prevented changes in PSP emissions due to color variations in model construction, and provided a surface for probe molecule adherence. The PtOEP/toluene mixture was sprayed onto the primer layer with an air brush until a solid pink coating was observed. Because of the ratioing nature of the Stern-Volmer equation, the paint layer did not have to be consistent in probe molecules or thickness over the model.

A Pixel Vision scientific-grade, air-cooled charge-coupled device (CCD) camera was used to record images, using a 516 x 516 pixel monochrome CCD and 50 mm lens. The camera lens was covered by a red filter to capture only PSP emissions. Images were processed with a 166 MHz Pentium V processor. The paint was excited with a Spectra-Physics Millennia continuous wave Yttrium Aluminum Garnet (YAG) laser at 532 nm. The 0.6 Watt laser light was taken from a laser table through a glass fiber optic cable with a 50 μm inner core and 250 μm outer core. Emitted cable light was directed onto a ground glass diffuser, and onto the test subject in the wind tunnel. A schematic of the setup may be viewed in Figure 13. The same type of setup was used for calibration.
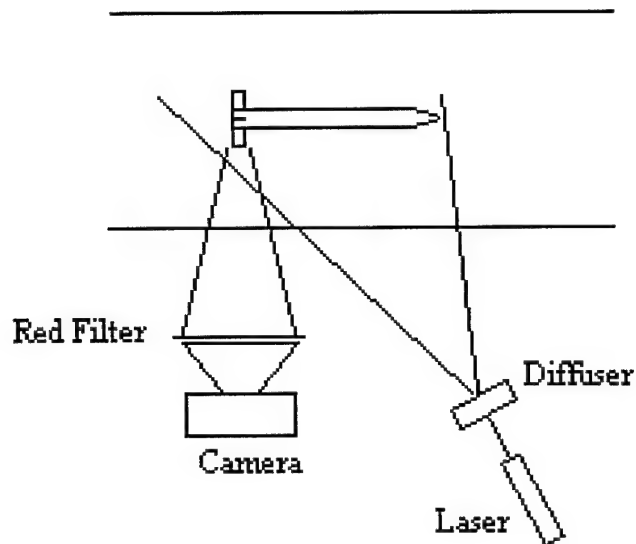
Figure 13. PSP Experimental Setup

The CCD used in this camera was 55 ±5 % efficient. The camera requires two photons to produce a guaranteed photoelectron, or one "count". The CCD used a 16-bit analog-to-digital converter, resulting in a maximum count level of 65,535. In raw data form, the CCD image was processed as a 516 x 516 matrix of integers. Laser intensity and shutter speed was adjusted to use the maximum range of the CCD without saturating it with too much light. The shutter speed was set at 0.5 s.

Ten images were recorded during the calibration procedure, background, and "air off" conditions. The text matrices of these images were averaged into one image using the program IM-AGE_AVG1.EXE, whose algorithm may be viewed in Appendix A. This procedure helped minimize errors from the photo efficiency of the CCD. The blow-down nature of the wind tunnels prohibited this averaging process during "air on" conditions, as static pressure was not constant. The variation of static pressure was slow enough to allow a constant-pressure assumption during the 0.5 second shutter speeds, however.

2.6 Rolling Moment Analysis

As mentioned previously, PSP data were used to determine rolling moments of the missile. Many bibliographic works cited in the PSP theory suggest that aerodynamic loads may be determined with paint data. But none of the papers referenced actually demonstrate this concept, a central topic of the present work. The research intended to resolve the pressure field in the vicinity of the WAF, and ensure that these fields were capturing the rolling tendencies observed in past experimentation. In order to perform this analysis, four assumptions were made about the data.

First, the missile was assumed to be at zero angle of attack. During tests, angle of attack variations of ±0.8 degrees were noted, permitting such an assumption. Second, the missile was oriented at zero roll angle, meaning convex and concave sides of the fins were completely parallel to the photographic plane. Pixel measurements confirmed the validity of this assumption, by comparing the vertical length of the convex and concave sides of the fin in the same image. The two lengths should have been the same if the missile was oriented at zero roll angle. The measured pixel lengths varied by ±6 pixels at maximum in the vertical, or j-direction. On the average, however, there was ±2 pixel variation out of a 140-pixel data field in the j-direction.

Third, the pressure was assumed constant at each pixel. More than 100 pixels in the i- and j-directions permitted this assumption, creating a 0.1 mm resolution in the fin region. This resolution was on the same order of magnitude as the surface roughness height of the steel used to construct the fins. Finally, it was assumed that viscous shear forces did not contribute to the rolling moment.

The last assumption was the only source of error that could not be quantified with the present measurement techniques. One viscous CFD result at Mach 2.9 existed in Reference [28], and was used to quantify error involved in this assumption. Another important drawback to this analysis lay in the leading edge pressures. Because the high stagnation pressures fell beyond the calibration range of the PtOEP probe molecules, these data had to be neglected in the data analysis. Again,

22

using the CFD results from Reference [28], the leading edge rolling moment contribution error was quantified.

Rolling moments were calculated using a Cartesian coordinate system. The system placed the x-axis (i-direction) out the nose of the missile, and the y-axis (j-direction) at the base of the model, pointing vertically. Rolling moments were found by multiplying the pressure at each pixel by the pixel height and width, and multiplying that by the distance to the missile center line. The equation for the rolling moment contribution of either side of a fin is presented in summation form:

$$L = \sum_{j=1}^{j\,\text{max}} \sum_{i=1}^{i\,\text{max}} \left[P_{i,j} \left(dx \right) \left(dy \right) r_j \right] \tag{3}$$

In this equation, whose derivation is presented in Appendix B, rolling moment is denoted by L, the pressure at pixel location (i,j) is given by $P_{i,j}$, pixel width and height are denoted by dx and dy, respectively, and pixel radius is denoted by r_j. The values imax and jmax refer to the fin width and height in pixels. These values were found by editing PSP images for fin data only. These edited images were saved as rectangular text matrices, with matrix width and height known as imax and jmax. The values dx and dy were the same because the camera used a square 516 x 516 CCD. This number was found by taking a known length in the image, the missile diameter, and dividing it by the number of pixels that comprised the missile diameter in the image. The values of L for both convex and concave fins were added together and multiplied by four (there were four fins on the three-dimensional models). By convention, concave moments were negative, convex moments were positive. The value of r_j was found by the following equation:

$$r_j = r + j(dy) - \frac{dy}{2} \tag{4}$$

In this equation, r is missile radius, and j is the j-location of the current pixel. This ensures that r_j is determined at the center of the pixel.

23

Rolling moments were non-dimensionalized by traditional means for comparison with other studies:

$$C_L = \frac{L}{q_\infty A d}$$ (5)

In this equation, q_∞ is free stream dynamic pressure, A is missile cross-sectional area, and d is missile diameter. The values obtained with this equation were compared to CFD data obtained in past studies [12, 28, 31].

2.7 Oil Flow Visualization Technique

Oil flow patterns were used to determine velocity profiles over the three-dimensional WAF models. Past research efforts have conducted oil flow visualizations of a single wall-mounted model [1]. Profiles were compared to CFD data from Reference [28] at Mach 2.9. Velocity contours also yielded some information about viscous shear damping that was affecting rolling moment. Shear forces are undetectable with PSP.

The technique utilized fluorescent, powdered yellow dye, coded A-14-N, diluted in silicon oil. Because the boundary layer thickness on the missile body was much larger than on the fins, different viscosity oils had to be used on each part. The fin required 200 cS oil mixed with pigment, whereas the body required 50 cS oil. The dye was illuminated with two 115 V Blak-Ray B-100A ultraviolet lamps. Images of the oil were taken during runs using a Nikon DCS 420 color digital camera, using an ISO 200 setting and a shutter speed of 1/30th of a second. A schematic of the oil flow visualization technique may be viewed in Figure 14.
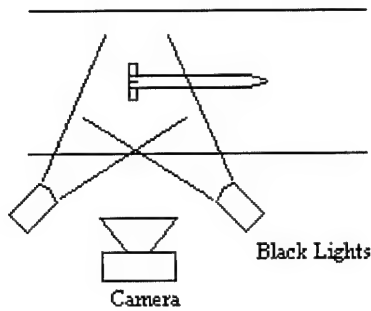
Figure 14. Oil Flow Visualization Setup

2.8 Schlieren Setup

Schlieren photographs were obtained with a continuous-wave light source and a spark light source. The continuous source used a mercury-vapor lamp at 120 V. The spark light source produced a burst of light approximately 150 ns in duration. The Cordin model 5401 point light source operated at 10 kV, using a Cordin model 5205 power supply. With room lights dimmed, the digital camera shutter was opened long enough for the light of one spark to be recorded (2.5 s). A vertical knife edge was used in order to resolve shock locations in front of the WAF. Color schlieren photographs were also taken, using a red-blue color slide in place of the knife edge. A diagram of the schlieren setup may be seen in Figure 15.
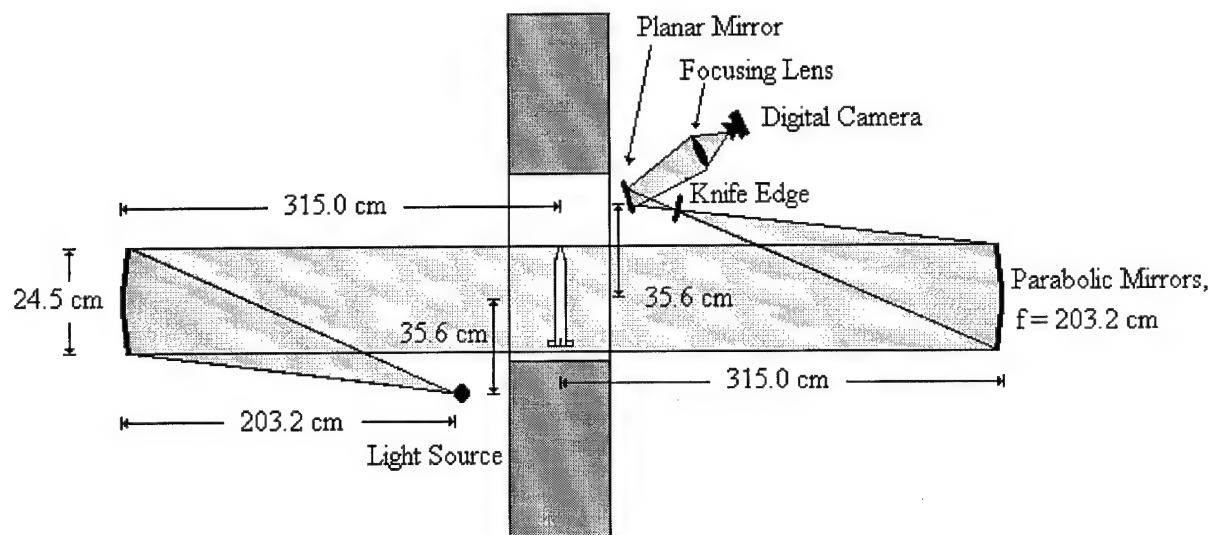
Figure 15. Schlieren Setup

26

Chapter 3 - Results and Flow field Analysis

The PSP data was the primary and most revealing source of information. Shocks, vortices, and other aerodynamic features are easily resolved using these results. These data are presented and compared to CFD results, providing essential validation for both techniques. Oil flow visualization results display velocity information which is also compared to CFD results for a single fin. Schlieren images display shock locations which verifies the information observed in both PSP and oil flow results. The last section of this chapter describes the overall flow field using the three data measurement techniques. Solid fin data are presented first in each section, followed by slotted fin data. Error analysis for all data is presented in Appendix B.

3.1 PSP Results

Pressure data are non-dimensionalized with free-stream total pressure. This makes comparison with CFD data possible. This also makes data points comparable at each Mach number, which would otherwise be impossible due to the blow-down nature of the wind tunnel. In general, agreement is good between these data and Reference [28], which uses a chord length of 0.64d, versus 0.53d. Agreement is also good when compared to Reference [12], which uses a chord length of 1.75d. That is, the data in the first third of this chord agrees well with experimental data.

The maximum error in Mach number was due to pressure calibration error values. As shown in Appendix B, the maximum Mach number error, or norm, was ± 0.0047.

3.1.1 Solid Fin

Results are presented for the two solid fin models tested. The three-dimensional model data were the most important in this study, and are presented first. This is followed by the wall-mounted model, in which comparisons are drawn between CFD, the wall-mounted model, and the three-dimensional model.

27

3.1.1.1 Three-Dimensional Model

Testing was conducted at zero angle of attack. Mach numbers tested include 2.15, 2.28, 2.41, 2.86, 3.25, 3.50, and 3.83. The tunnel Reynolds numbers varied, depending on total pressure. Total temperature had little effect, as it did not vary much. Representative plots of wind tunnel total pressure and temperature may be viewed in Appendix C. At all Mach numbers, the large total pressures required were depleted from the reservoir only seconds after testing began. This results in different Reynolds values for each image processed. Reynolds numbers ranged from 9.7 x 10^6 at Mach 2.15 to 3.4 x 10^6 at Mach 3.83, decreasing linearly with increasing Mach number.

To prevent cooling effects on the PtOEP paint, only the first three images were used from each run. The probe molecules emit at 650 nm, or light red in the visible spectrum. Images captured were red monochrome, which was false-colored using photograph reduction software. Color bars were manipulated to reveal important aerodynamic characteristics in the fin region.

Images at each Mach number can be viewed in Figures 16, 17, and 18. The application of the Stern-Volmer equation caused an important phenomenon in each image. The slight movement of the model during "air on" images had to be accounted for in data reduction. Using the computer program PSP.EXE, movement corrections were made in the plane of the image. But because this was only a two-dimensional correction, error was caused by the slight roll of the missile. The roll caused false pressure data to be recorded around the body of the missile, which may be viewed in each PSP figure.
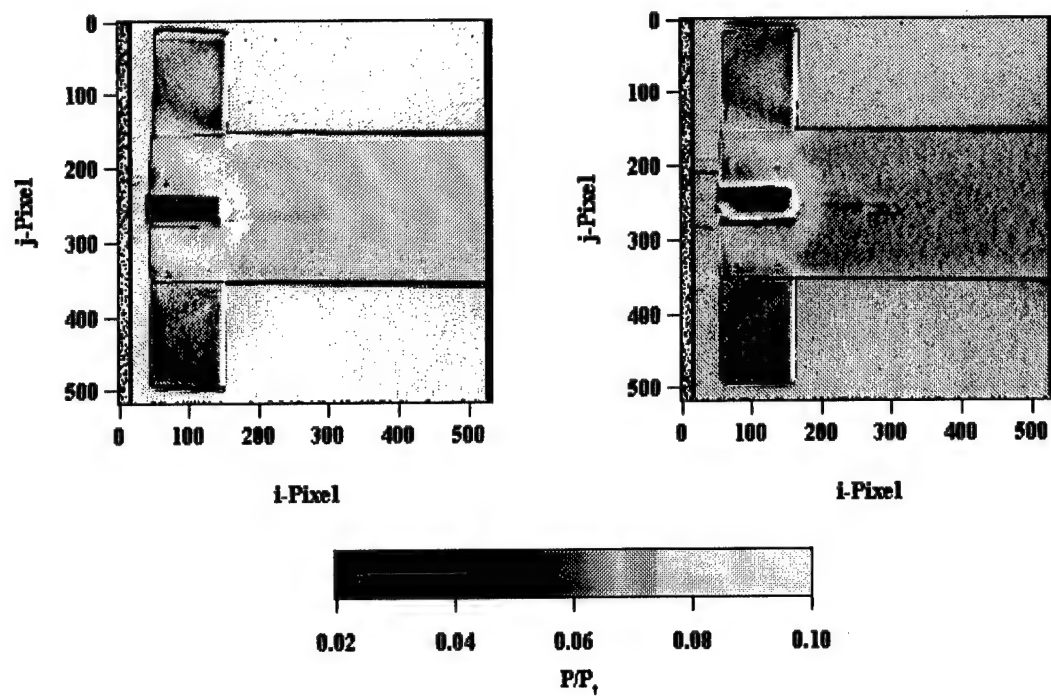
Figure 16. Solid Fin PSP Images at Mach 2.15 (left) and 2.28 (right)
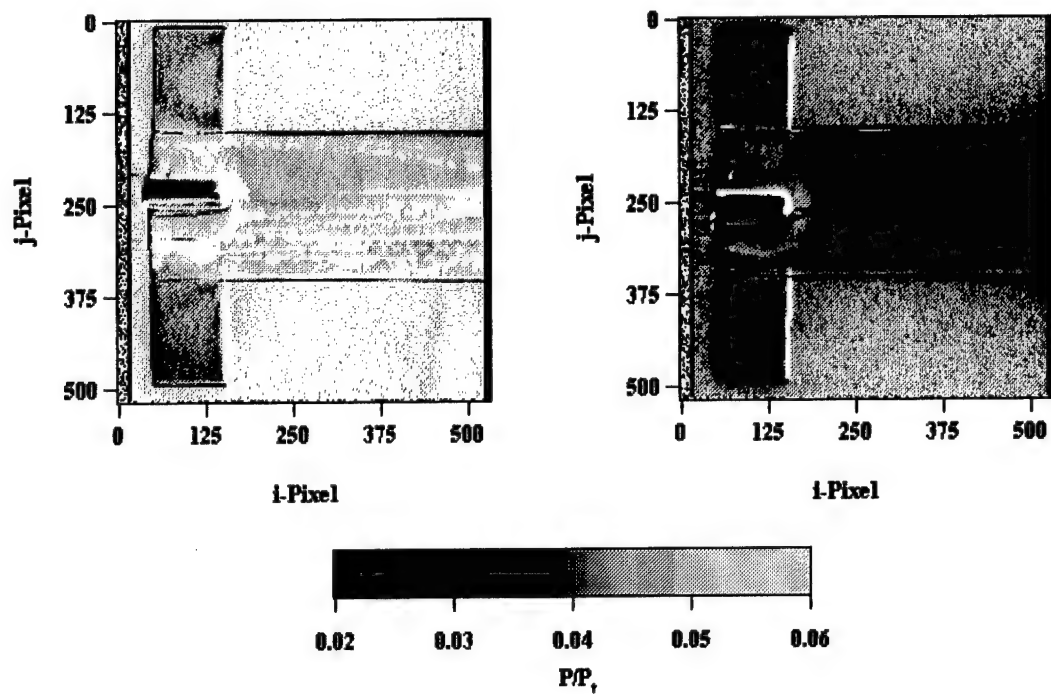
Figure 17. Solid Fin PSP Images at Mach 2.41 (left) and 2.86 (right)
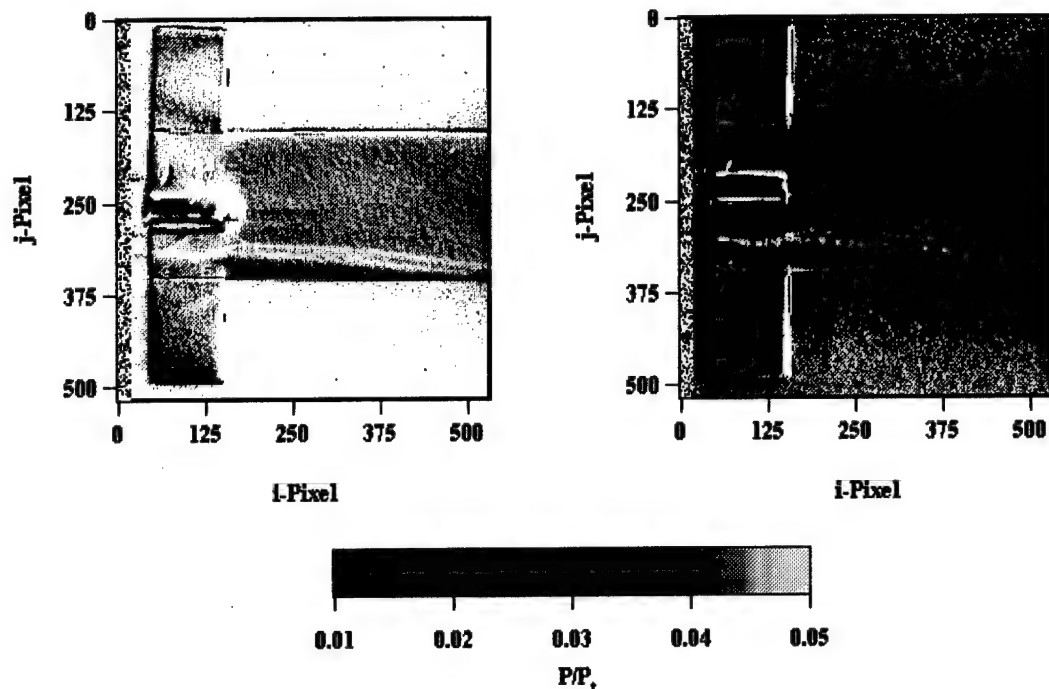
Figure 18. Solid Fin PSP Images at Mach 3.25 (left) and 3.50 (right)

A static pressure port was installed on the side of the model to verify PSP values on the fuselage. While this port did verify pressure magnitudes, it began to contaminate data downstream. During testing, water vapor began to condense out of the tube connected to the transducer. The PtOEP paint became irreparably damaged as condensation instantly crystallized in the low static temperatures of the supersonic flow. Evidence of the most severe damage may be viewed in the Mach 2.41 image in Figure 17. The missile was rotated 90 degrees counter-clockwise for further testing, which is at the bottom of the missile in the Mach 2.86 image. Though fin paint was not damaged, usage of the static port was discontinued to prevent further contamination.

The leading edge of the fin lay in supersonic airflow, which is evidenced by the bow shock in all three figures. The stagnation pressures seen by the leading edge lie far beyond the range of the PtOEP probe molecule. The large amount of oxygen-quenching occurring at the leading edge

31

resulted in no photon emissions, which corresponds to high pressure on the calibration curve. The pressures are off the scale, as shown in each figure, depicted by white.

3.1.1.2 Wall-Mounted Fin and CFD Comparison

This portion of research helped validate previous research efforts at AFIT. The CFD pressure computations of Reference [28] were never verified experimentally. The study also made a key assumption about WAF behavior at zero angle of attack. The study assumed that a single wall-mounted fin would capture all of the aerodynamic features witnessed by a three-dimensional model. Because the research of Reference [28] was so exhaustive, validation for this assumption was required. Mach 2.9 was the only data point taken using the single-fin model.

Results of testing are presented in Figure 19. Data at the top are CFD results from Reference [28]. Following these are single-fin results from the AFIT Mach 2.9 wind tunnel. Finally, three-dimensional WAF data are shown again, edited for comparison. All major flow features discovered with CFD were resolved in testing. Triangular regions of high pressure on both sides of the fin were resolved, an important factor in the rolling moment. Detailed flow descriptions follow the results of oil flow testing. Good agreement was also achieved between the single-fin results and the full configuration. This validates the single-fin assumption and provides support for the data obtained in the AFIT Variable Mach Tunnel (VMT).
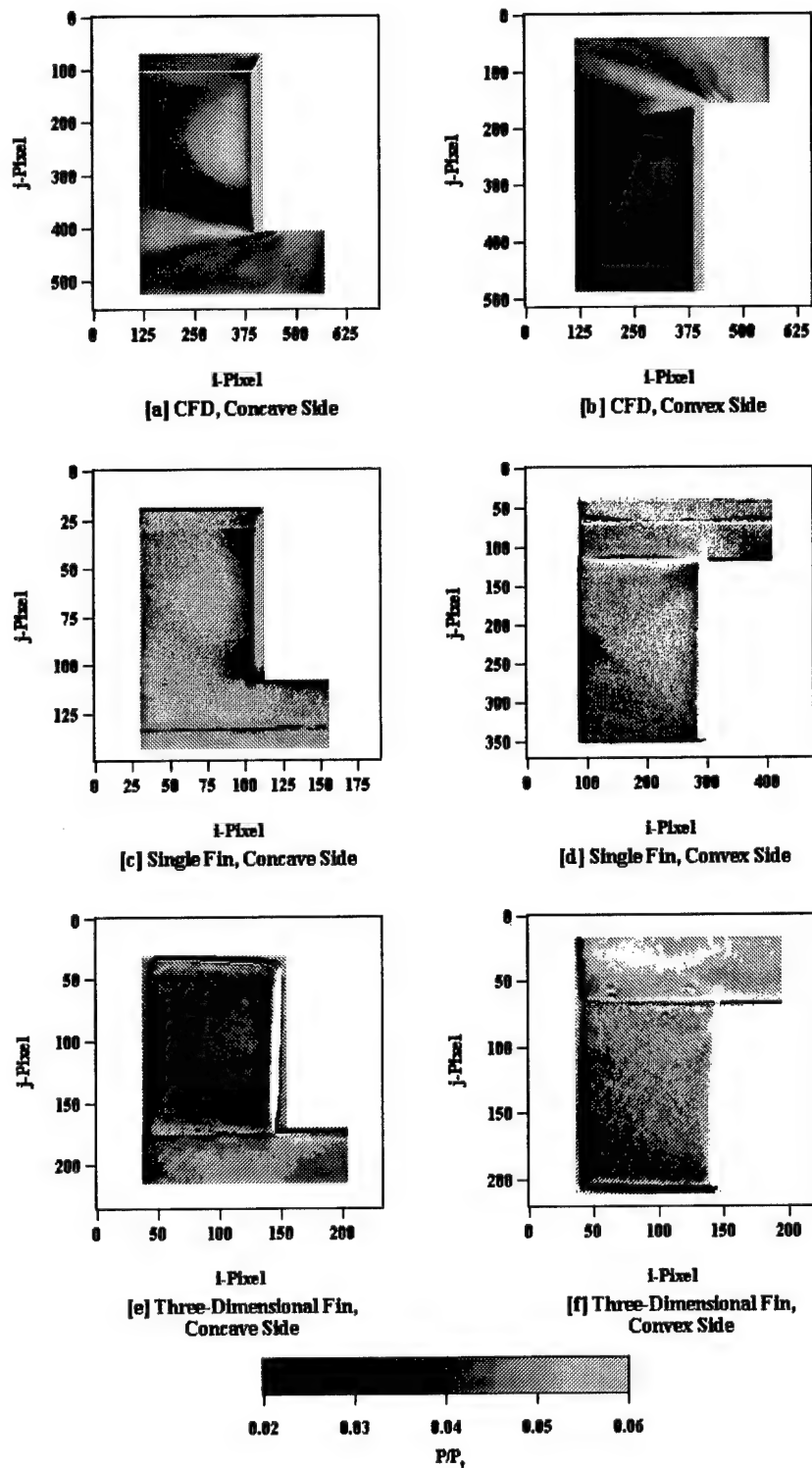
[a] CFD, Concave Side

[b] CFD, Convex Side

[c] Single Fin, Concave Side

[d] Single Fin, Convex Side

[e] Three-Dimensional Fin,
Concave Side

[f] Three-Dimensional Fin,
Convex Side

Figure 19. Comparison of Techniques at Mach 2.9

33

Although the wall-mounted fin and three-dimensional model differed in size, the Reynolds numbers compared well. The Reynolds number used for comparison was based on chord length, represented by the equation:

$$Re_c = \frac{\rho_\infty V_\infty c}{\mu_\infty} \tag{6}$$

Free stream density and velocity were found with wind tunnel total pressure, static pressure, and total temperature data. Viscosity was fixed at 1.7×10^{-5} N-s/m^2. The Re_c value for CFD computations was fixed at 3.4×10^5, while the three recorded PSP images had Re_c values of 2.44×10^5, 3.78×10^5, and 3.24×10^5. This dynamic similarity between CFD and PSP images justifies comparing the data of different models from different tunnel conditions.

PSP measurements on the wall-mounted fin were more difficult to obtain because of model construction. Because only one CCD camera was available, images of each side of the fin were taken during independent tests. Repeated testing resulted in PSP wear, which is witnessed in image [c] in Figure 19. The aluminum body was resistant to underlying white primer coating. On the aft, center portion of the convex side of the fin, a white primer bubble changed the geometry of the fin. This resulted in a spot of high pressure which is evident in image [d] of Figure 19. Other than these faulty areas, good agreement was achieved.

3.1.2 Slotted Fin

Slotted fin testing was only performed in the VMT. Surface pressure data was not presented in any of the bibliographical works cited, so no direct comparison could be drawn. PSP images are presented in Figures 20, 21, and 22. During these tests, the static pressure port was not connected to the transducer tubing, preventing damage. Mach numbers 2.28 and 3.83 could not be tested due to wind tunnel damage sustained during tests.
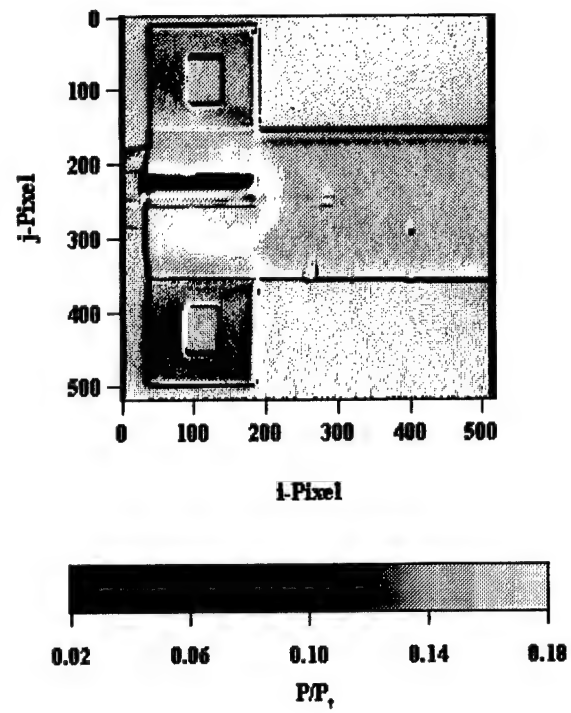
Figure 20. Slotted Fin PSP Image at Mach 2.15
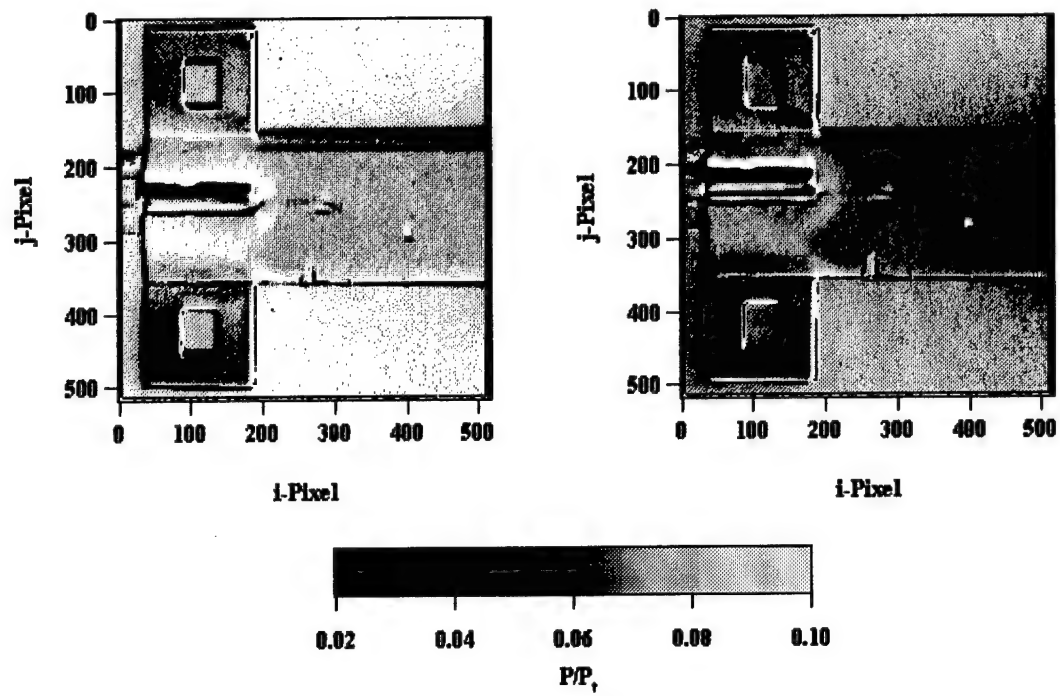
Figure 21. Slotted Fin PSP Images at Mach 2.41 (left) and 2.86 (right)
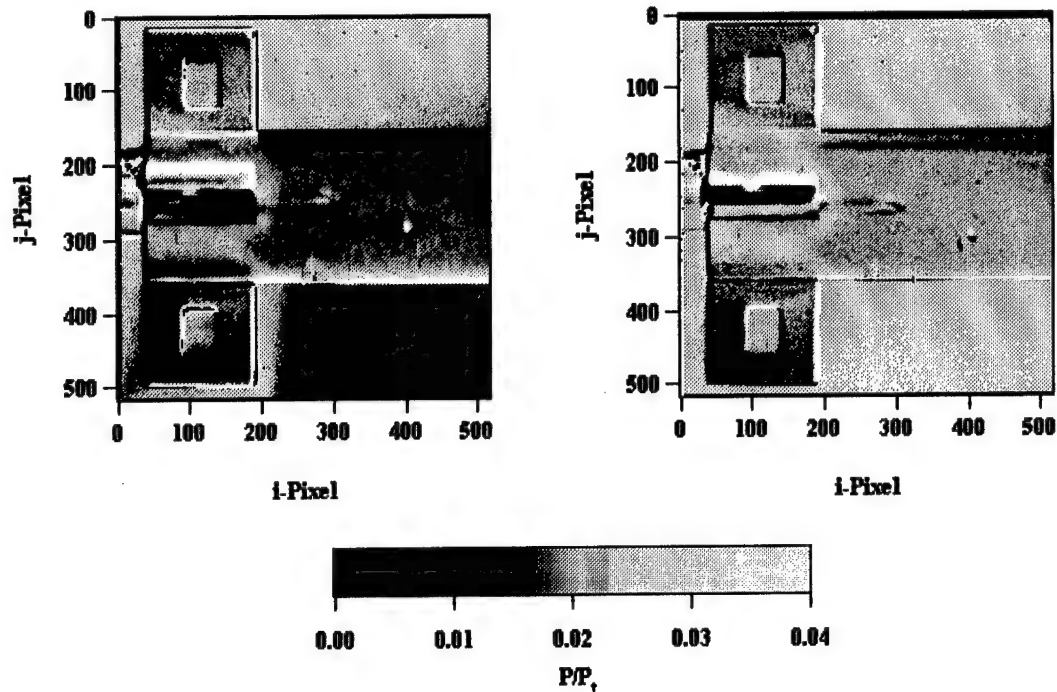
Figure 22. Slotted Fin PSP Images at Mach 3.25 (left) and 3.50 (right)

3.2 Rolling Moment Analysis

3.2.1 Solid Fin

Rolling moments were computed, and then non-dimensionalized with dynamic pressure, missile cross sectional area, and missile diameter. The data were plotted against Mach number, revealing trends that were matched in past testing. That is, as Mach number increases, the rolling moment coefficient decreases in an asymptotic nature. At supersonic velocities, the rolling moments are negative, where the x-axis points out the nose of the model. Figure 23 presents rolling moments computed, while Figure 24 presents the rolling moment coefficients.
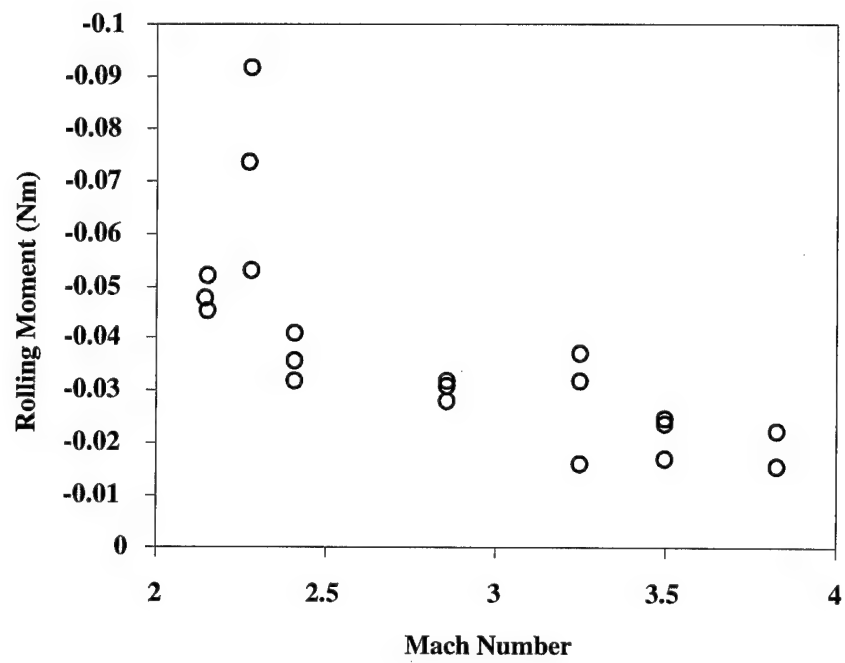
Figure 23. Solid Fin Rolling Moments
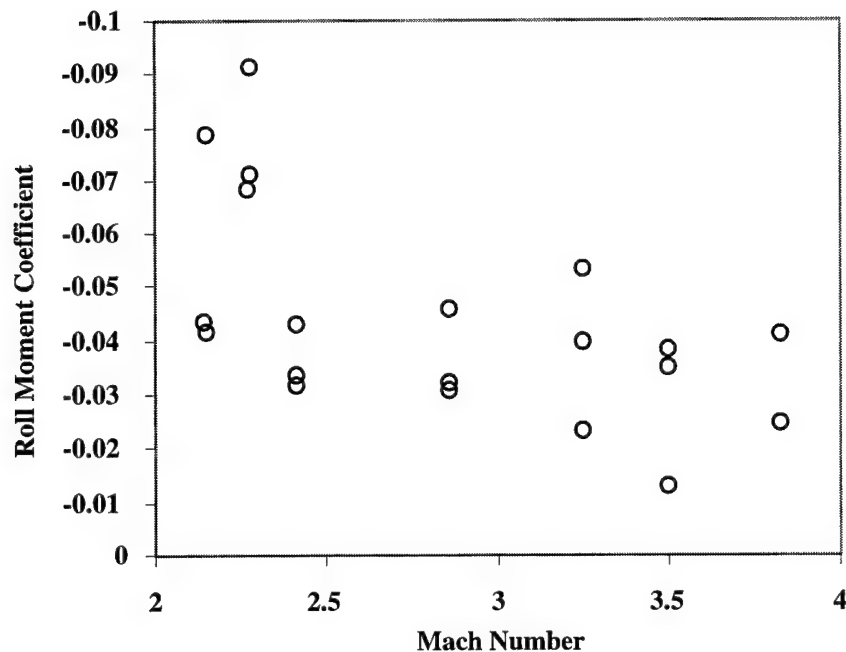
Figure 24. Solid Fin Rolling Moment Coefficients

The scatter of the data in these graphs can be attributed to free stream Reynolds number variations. Reference [12] cites that tests conducted by McDonnell Douglas, AEDC, NASA Langley, and NASA's Jet Propulsion Laboratory all confirm that Reynolds number variation causes data scatter. The blow-down nature of the tunnel used in the present study resulted in total pressure variations that slowly change as the reservoir discharges. These changes in total pressure affect the Reynolds number, which varied rolling moments. Tunnel Reynolds number variations may be viewed in Appendix C. Reynolds numbers are plotted for different Mach numbers at the point when the PSP image was taken. Missile length was used as the reference length for these Reynolds number calculations.

The PSP data were intended to resolve the pressure field in the vicinity of the fin. As seen in the rolling moment graphs, the PSP data also capture the rolling moment tendencies observed in

past data, fulfilling a major goal of this study. These data are compared to the single-fin CFD results of Reference [28]. The CFD data were chosen for comparison because of the geometric similarity between the fin in that study and the current fin geometry. The fin had chord length of 0.64d, when compared to the 0.53d length in the current research. Both fins had blunt leading edge, beveled at 45 degrees. Figure 25 presents average rolling moment coefficients from Figure 24, with error bars corresponding to the standard deviation of each data point. The data are compared with two viscous CFD calculations at Mach 2.9 and 5.0, and to inviscid calculations ranging from Mach 2.5 to 4.0 [28].
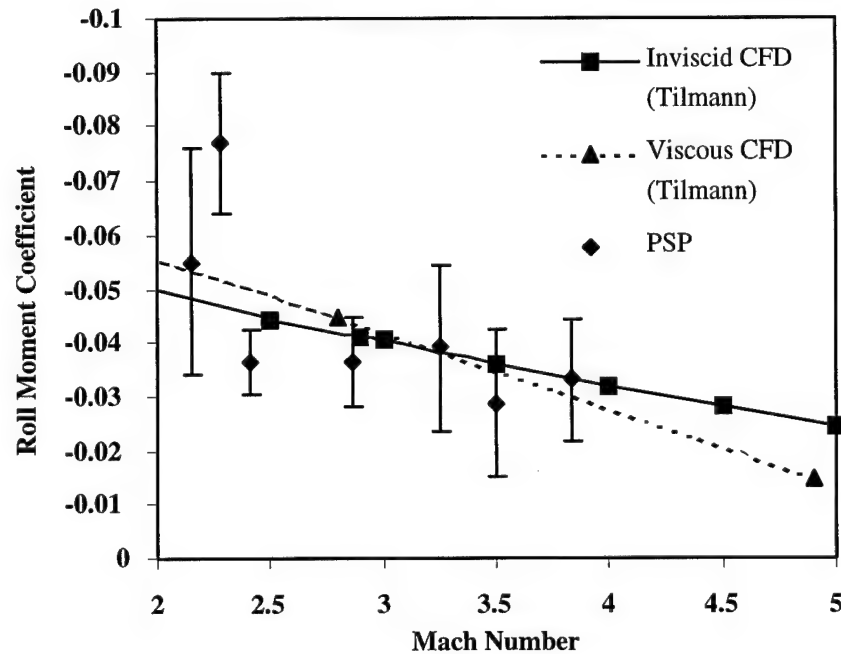
Figure 25. Solid Fin Rolling Moment Coefficient Comparison

The Mach 2.4 data point lay slightly above the other points, causing concern. But this point was retained because no errors could be found in the pressure images and wind tunnel data. Because WAF negative rolling moments peak around the sonic barrier, this point still agrees with the general

40

data trend. Also, as the error analysis shows in Appendix B, all data compare well with CFD data when considering error bounds. An average rolling moment coefficient error of ±0.00656 was noted for all solid fin data.

Comparison of data to other studies was only performed on an order-of-magnitude basis and with respect to general data trends. A swept leading edge WAF was studied in Reference [31], using a chord length of 1.46d at the root, sweeping to 0.64d at the tip. Rolling moments were calculated for this fin using an implicit Euler CFD code. The data compare well with PSP data, ranging from -0.084 at Mach 2.0 to -0.053 at Mach 4.0, with roll-off rates in the same asymptotic fashion. Rolling moments and roll-off rates also compared well in magnitude with those found in Reference [12]. That study used a chord length of 1.75d and a 45-degree beveled leading edge, and a fin curvature radius of 2.415d. There were only six experimental data points in the same Mach range as the present study, and these points showed scatter due to Reynolds number variations. But these agreed in magnitude with the PSP rolling moment calculations.

A rolling moment analysis was not performed on the single wall-mounted fin because of the nature of the PSP data recorded. As previously mentioned the leading edge paint was worn away from repeated testing. The primer layer of paint caused a bump on the convex side, changing fin geometry and contaminating pressure results. Because of poor pressure readings in these areas, rolling moment calculations were not attempted.

3.2.2 Slotted Fin

Rolling moments were obtained for the slotted fin. Despite the area removed by the slot, the long chord length gave the slotted fin 28.6 % more area than the solid fin. Rolling moments were expected to be comparable in magnitude to the solid fin because of this fact. Figure 26 presents the

41

rolling moments derived from PSP images for the slotted fin. Figure 27 presents the rolling moment coefficients determined from free stream parameters.
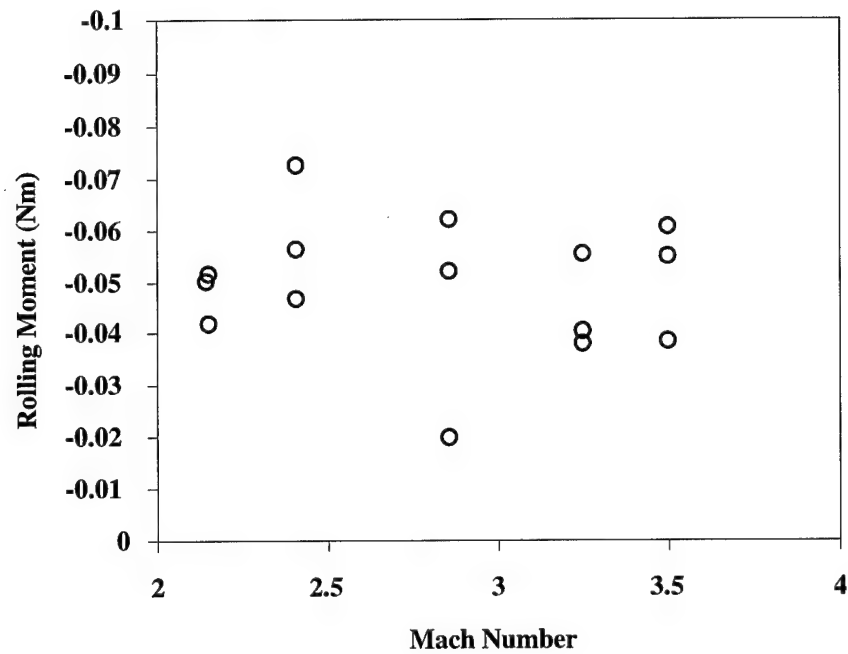
Figure 26. Slotted Fin Rolling Moments
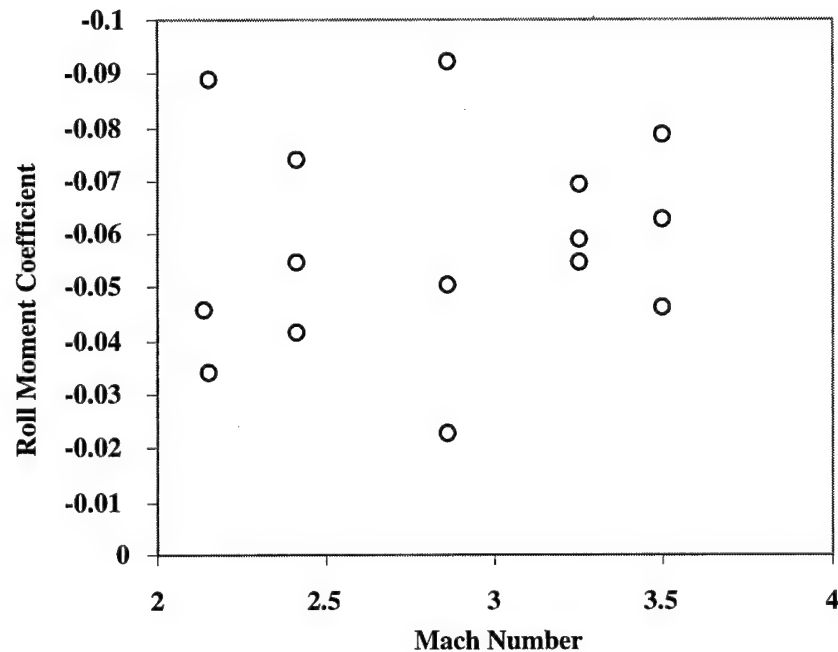
Figure 27. Slotted Fin Rolling Moment Coefficients

Slotted fin rolling moment data was inherently more difficult to obtain because of the slot. As the missile deflected in the tunnel, false pressure data were created around the missile. These data were ignored when the fin was isolated, but data in the slot also had to be removed. The location of the slot had to be determined and the false data deleted. This was a difficult task to perform in the two-dimensional plane of the PSP image, and resulted in the data scatter which is seen in the slotted fin rolling moment figures. Coupled with the Reynolds number rolling moment dependence, the scatter in the data are accounted for. The data capture the negative rolling moment tendencies of slotted WAF projectiles, and signal that the PSP data was capturing the relevant pressure data. Also, the error associated with slotted fin rolling moment coefficients was higher than the solid fin, averaging ±0.00771 for all data points.

Only one paper could be found for slotted fins that matched the current geometry [3]. Unfortunately, this paper did not present any rolling moment coefficient data, and could not be compared to the present research. The paper does cite that slotted fin ballistics testing revealed that no roll reversal occurs for slotted fins. Furthermore, at Mach number above 1.5, roll rates did not change with increasing Mach number. This would correspond to Figure 27, which hints that the roll moment coefficient is fairly constant, around -0.06.

3.3 Oil Flow Visualization Results

3.3.1 Solid Fin

Oil flow patterns for the missile confirmed shock locations and regions of varying pressure on both the concave and convex sides of the fin. In locations with higher pressure, the amount of oil decreases, displaced by higher pressure. Areas of separation were also noted behind the fin and fuselage as small volumes of oil recirculated behind the missile. Comparisons of CFD velocity streamlines and oil flow patterns at a Mach 2.9 condition are shown in Figures 28 and 29, where both sides of the fin were cropped for ease of comparison. Despite only having one fin with a longer chord length, the data on the fin itself compare well with wind tunnel data of the three-dimensional fin. Velocity profiles diverge towards the aft center portion of the fin, and diverge from the surface at the bottom of the fin. The missile body itself does not compare well, as the other fins cause a shock compression in the flow field between the fins. But as indicated by PSP comparisons, this compression was not significant enough to affect fin surface pressures. The bow shock caused by the fin is evident on the body, seen by the dark region prior to the fin. Areas of higher pressure on the fin are also evident.
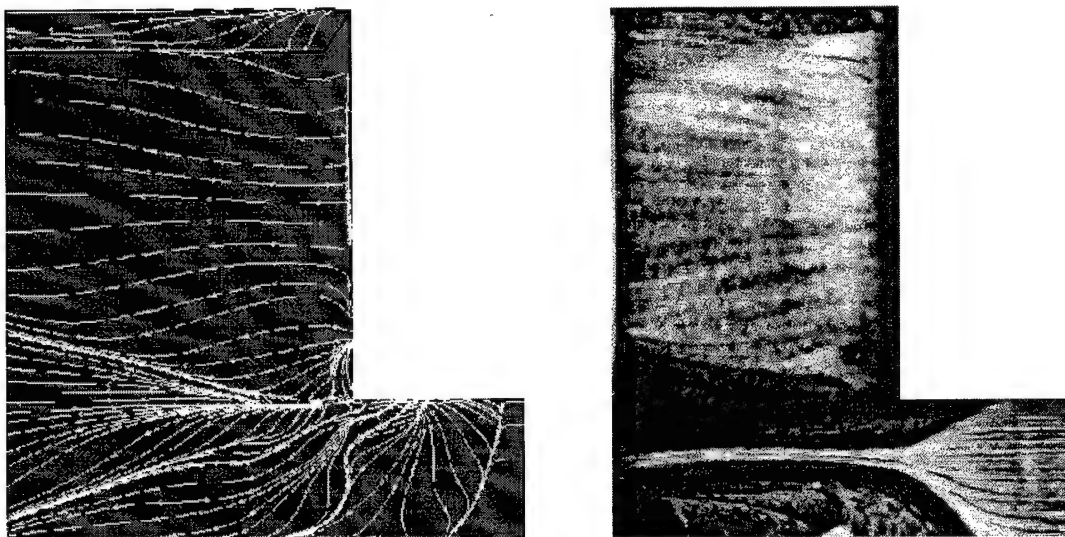
Figure 28. Concave Fin Streamline Comparison of CFD (left) and Experimental Data (right) at Mach 2.9
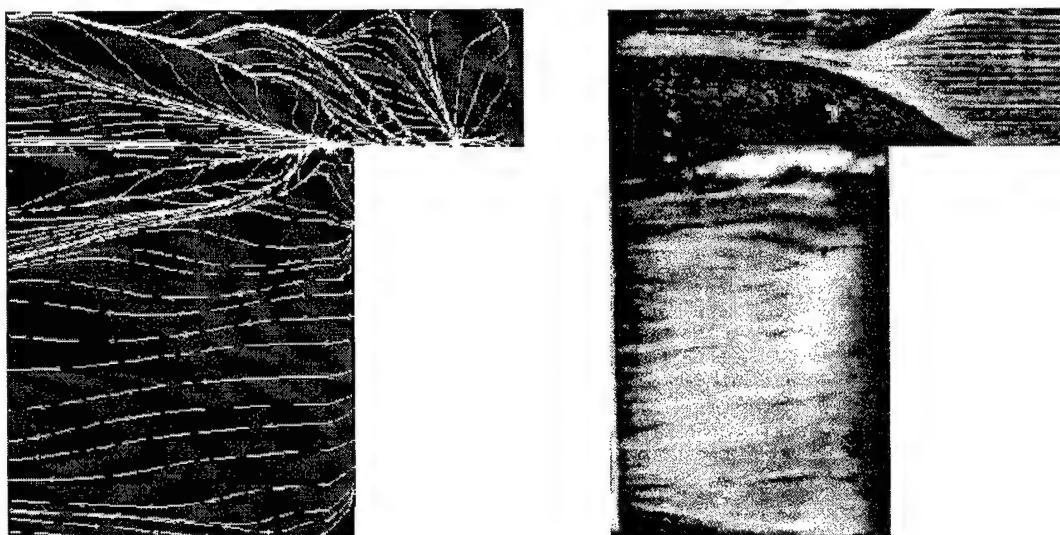
Figure 29. Convex Fin Streamline Comparisonof CFD (left) and Experimental Data (right) at Mach 2.9

At varying Mach numbers, the profile changes slightly. Oil profiles at Mach 2.15, 2.86, and 3.83 are presented in Figures 30, 31, and 32, respectively. At Mach 2.15, streamlines diverge in the same pattern as at Mach 2.86, but in a more dramatic manner. At Mach 3.83, little variation occurs on the concave fin (top). On the convex fin (bottom) strong flow gradients are noticed near the

45

fuselage, and are more pronounced at high Mach. Images at intermediate Mach numbers appear very similar to these images, making a smooth transition in appearance. Remaining images are shown in Appendix C.

PSP measurements correspond well with features shown in oil flow images. On the concave side of the fin, the region of boundary layer compression adjacent to the missile body may be clearly viewed by the displaced oil. Oil was also displaced on the leading edge, as expected. The effects of fin curvature are seen as oil diverges on the aft portion of the concave fin. This agrees with PSP images, as pressure decreases on the aft portion of the fin. Oil patterns on the convex side of the fin do not show a distinct steak line where the vortex occurs. When PSP images are compared to oil flow patterns, the location of the vortex is resolved. Figure 32 provides the best evidence of the vortex using oil flow visualization. On the body, the lamda shock location is displayed clearly by oil displacement preceding the fin. This also agrees well with PSP results.

Figure 30. Solid Fin Oil Flow Pattern at Mach 2.15
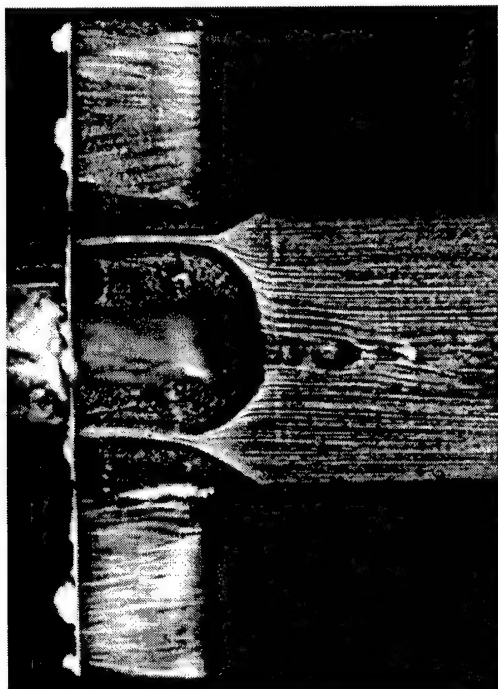
Figure 31. Solid Fin Oil Flow Pattern at Mach 2.86
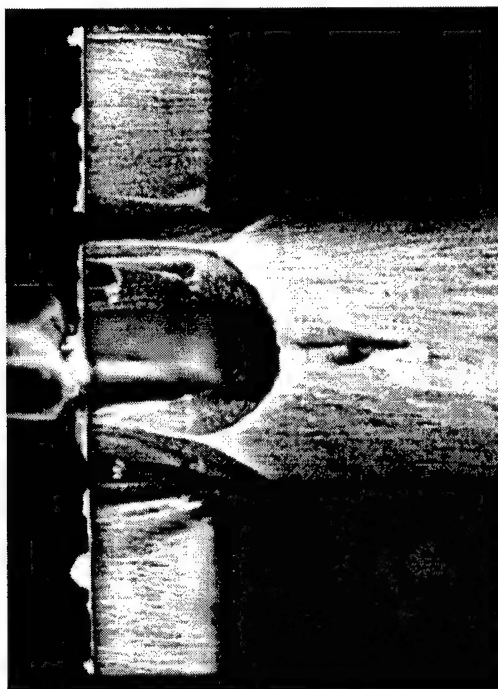
Figure 32. Solid Fin Oil Flow Pattern at Mach 3.83

3.3.2 Slotted Fin

Oil flow patterns for the slotted fin closely parallel those of the solid fin. Prior to the slot itself, the flow appears indistinguishable from the solid fin. Data for Mach 2.15, 2.86, and 3.83 are presented in Figures 33, 34, and 35. On the concave side of the fin (top), the oil appears thicker directly aft of the slot. This would correspond to a lower static pressure, agreeing with PSP data and indicating that pressure relief was occurring at the slot. Only on the bottom portion of the concave slot does the flow pattern appear affected. Small volumes of oil remain inside of the slot, in a recirculation zone just aft of the leading portion of the fin. The convex side of the fin shows signs of pressure relief from the concave side. The bottom, aft corner of the fin shows a downward flux of oil, proceeding away from the body. The same location on the concave fin displays velocity vectors pointing slightly upwards, toward the body. All other flow patterns on the fins match in a qualitative sense. Images at intermediate Mach numbers can be viewed in Appendix C.

PSP images compliment the oil flow images. Similar to the solid fin, the region of boundary layer compression on the concave fin is clearly marked by the displaced oil. On the convex side, the vortex structure is marked by displaced oil, prior to the slot. Vortex location is confirmed by PSP data. Using PSP images, it was determined that pressure was exhausting to the convex side of the fin. This determination was confirmed by oil flow near the tip of the convex side of the fin, as flow diverges away from the body. The missile body oil flow images also confirmed PSP results, displaying the location of lamda shocks by oil displacement.

48
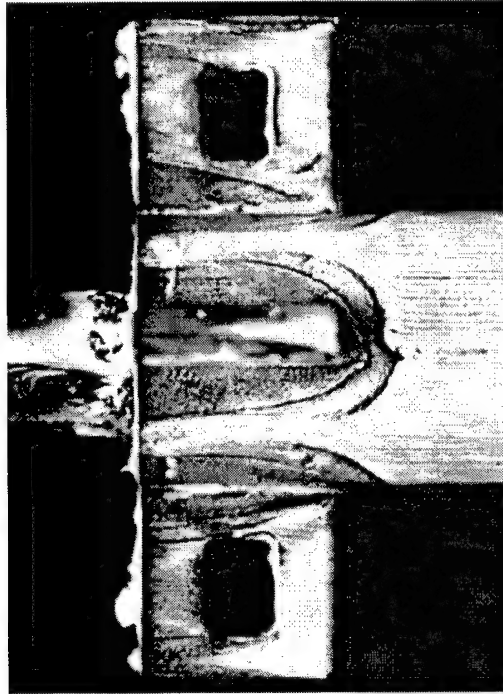
Figure 33. Slotted Fin Oil Flow Pattern at Mach 2.15
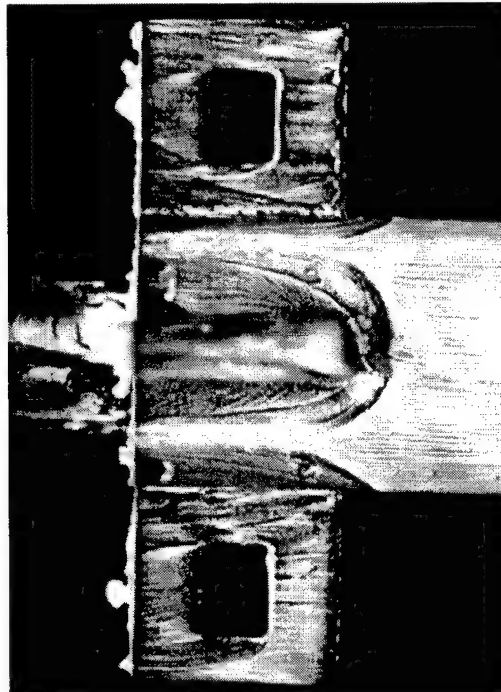
Figure 34. Slotted Fin Oil Flow Pattern at Mach 2.86

49
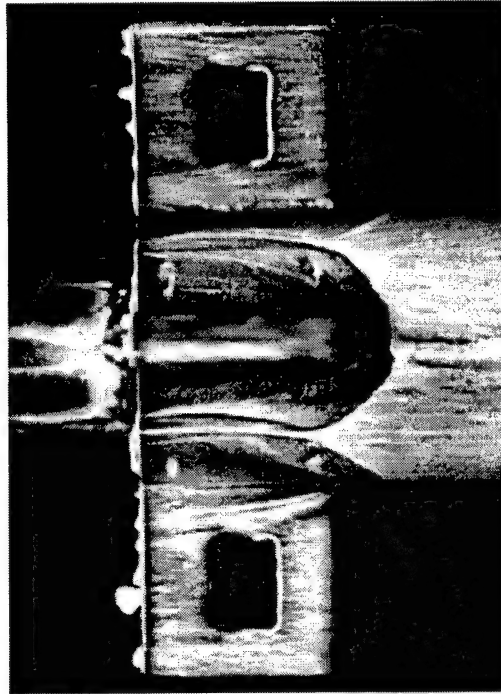
Figure 35. Slotted Fin Oil Flow Pattern at Mach 3.83

3.4 Schlieren Results

The two light sources utilized for schlieren photography resulted in different images, but both revealing important flow characteristics. Images for both light sources are presented for each fin. Color schlieren images were found with the spark source, using a color film slide. The slide used red and blue pigments separated by a narrow green stripe measuring 1.27 mm. The slide's vertical green stripe was used in place of the knife edge. While changes in red and blue are more discernible to the naked eye, the slide blurred the fin region of the missile. An example of the color schlieren image may be viewed in Appendix C.

3.4.1 Solid Fin

Using the continuous-wave light source, time-averaged, first derivatives of density were observed [8]. The images confirmed shock phenomenon observed in past testing [15,28], and revealed

50

some qualities of shock/boundary layer interactions. A vertical knife edge was used to resolve vertical shock structures in front of the fin, which would have been nearly invisible with a horizontal knife edge. Figures 36, 37, and 38 present continuous-wave schlieren images at Mach 2.15, 2.86, and 3.83. In each image, the boundary layer is seen on the body and envelopes approximately 20% of the fin region. The intersection of the normal fin shock and the boundary layer resulted in a lamda shock seen at the bottom leading edge corner of each schlieren image. In Figures 37 and 38 the oblique shock generated from the nose of the missile can be seen.

Figure 36. Solid Fin Continuous-Wave Schlieren Image at Mach 2.15

Figure 37. Solid Fin Continuous-Wave Schlieren Image at Mach 2.86

Figure 38. Solid Fin Continuous-Wave Schlieren Image at Mach 3.83

The spark light source provided more detail about the flow field upstream and within the vicinity of the model. Because the spark duration was approximately 150 ns, virtually instantaneous flow details were observed. Figures 39, 40, and 41 yield qualitative information about the free stream turbulence intensities of the wind tunnel. Each image displays a slightly different version of the lambda shock observed previously, indicating that the lambda shock is a time-averaged phenomena. This is most probably due to intermittent turbulent nature of the boundary layer at this fuselage length. Boundary layer vortices of subsonic air mixed with supersonic free stream air result in the intermittent lambda shock. Fin normal shocks and missile nose shocks were unaffected by free stream turbulence intensities.

Figure 39. Solid Fin Spark Schlieren Image at Mach 2.15
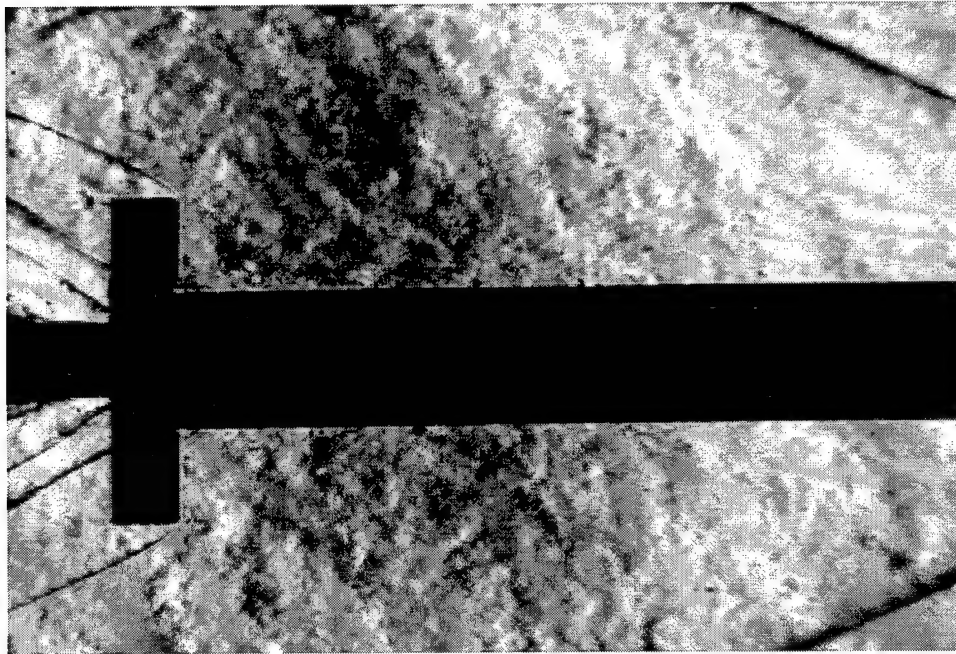
Figure 40. Solid Fin Spark Schlieren Image at Mach 2.86
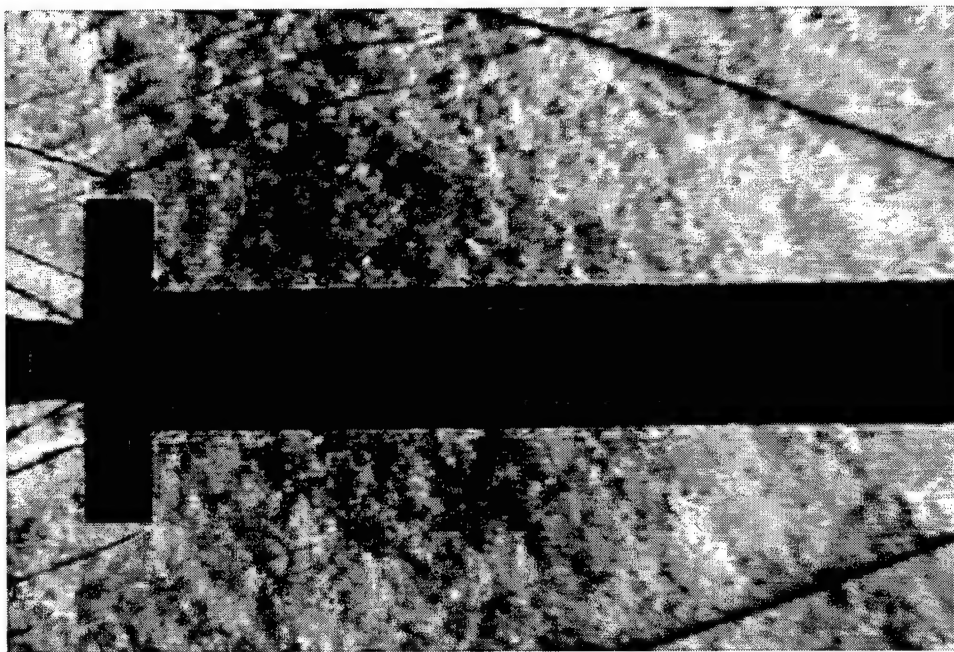
Figure 41. Solid Fin Spark Schlieren Image at Mach 3.83

54

3.4.2 Slotted Fin

Schlieren images for the slotted fin were very similar to the solid fin, as expected. Images are displayed for Mach 2.15, 2.86, and 3.83 in Figures 42, 43, and 44. Boundary layers on the top of the missile, however, appear thicker than on the bottom, indicating that the missile was at a small angle of attack. Further investigations with a digital photograph imaging program revealed that angles of attack were positive, ranging from +0.4 to +0.8 degrees. The added visibility created by the slot revealed little additional flow information.

When comparing solid fin and slotted fin images, the vortex location changes due to pressure relief by the concave fin. At Mach 2.15, the vortex can be seen exiting behind the fin in Figure 42 at almost 75% of fin span. In contrast, the solid fin vortex exits at only 50% of fin span, as seen in Figure 36. Schlieren images compliment PSP and oil flow techniques and conclusions by confirming shock locations and by revealing vortex locations behind the missile.
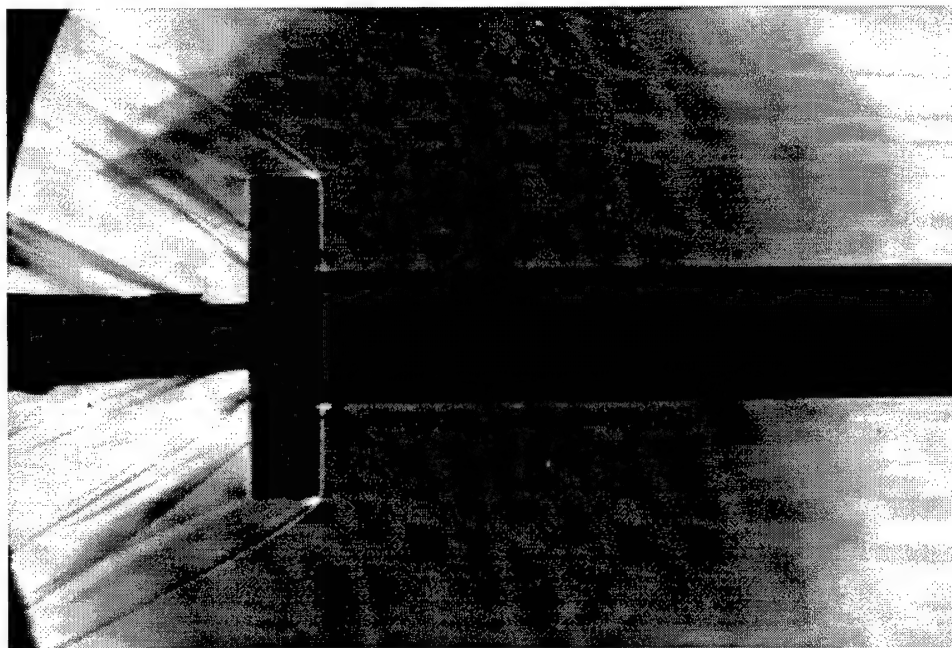

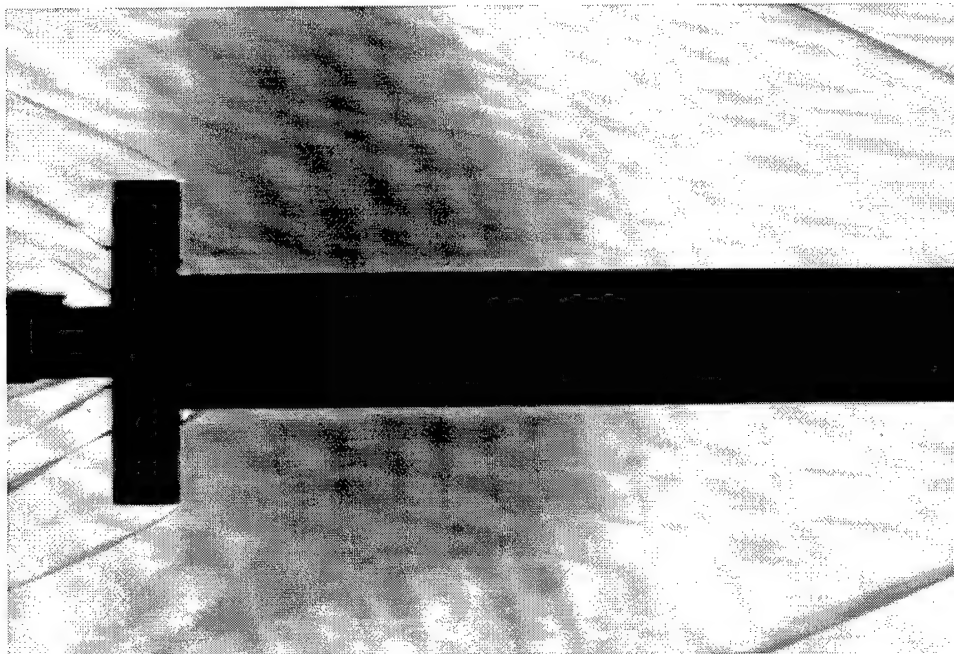Figure 42. Slotted Fin Continuous-Wave Schlieren Image at Mach 2.15
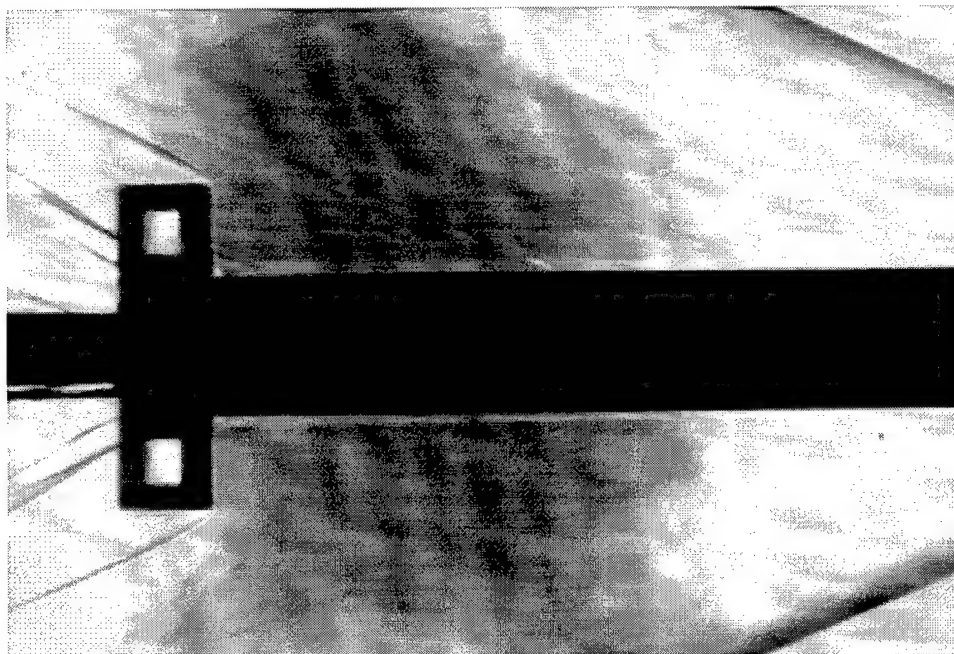
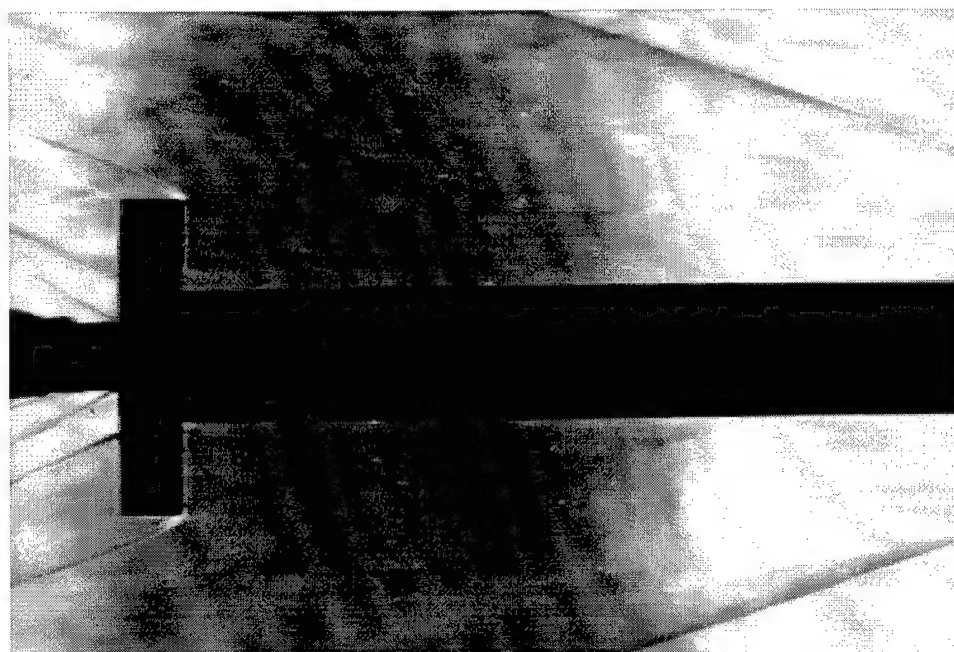Figure 43. Slotted Continuous-Wave Schlieren Image at Mach 2.86
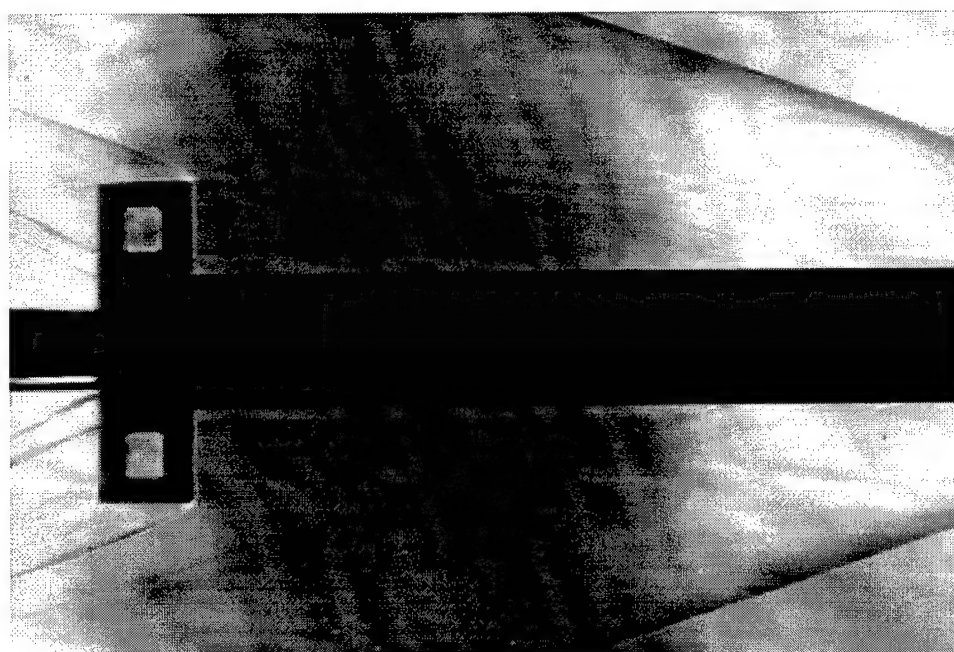
Figure 44. Slotted Fin Continuous-Wave Schlieren Image at Mach 3.83

Spark images were also similar to the solid fin, revealing no new information. Characteristic images at identical Mach numbers may be viewed in Figures. Additional Mach number images, both continuous-wave and spark light source, may be viewed in Appendix C.
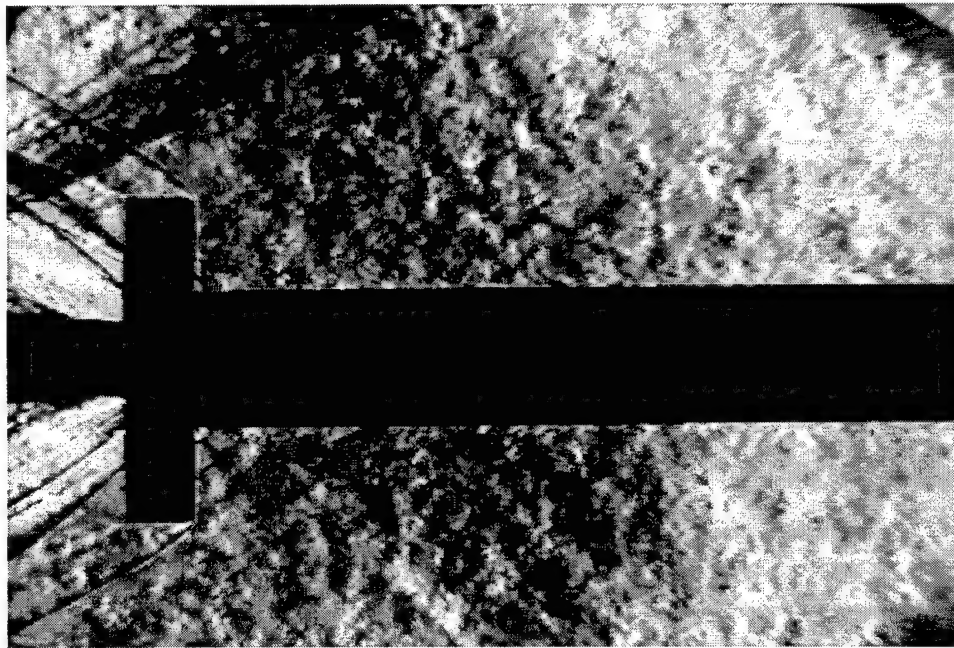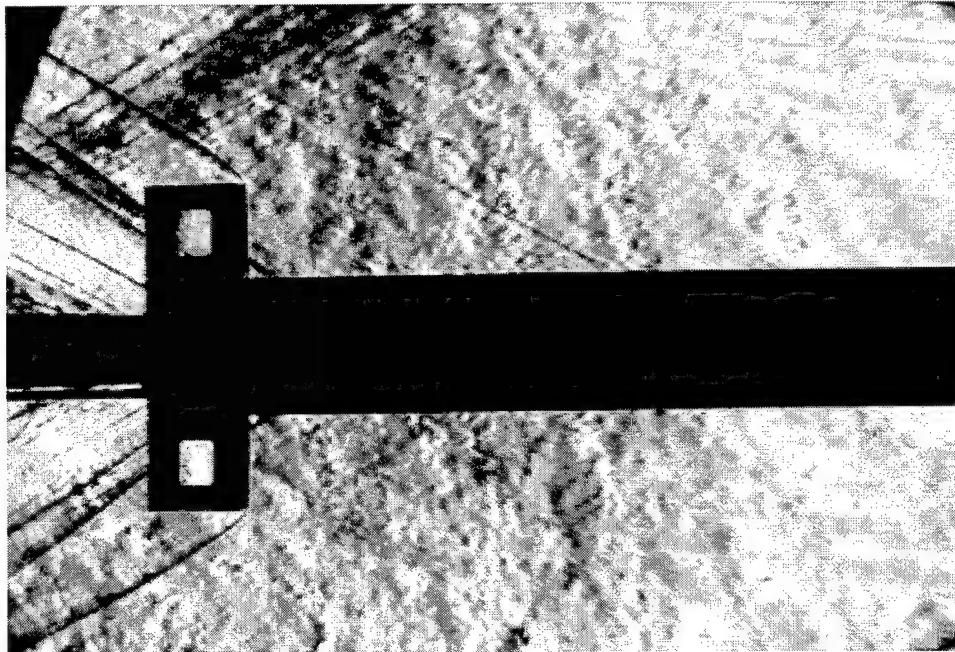

Figure 45. Slotted Fin Spark Schlieren Image at Mach 2.15
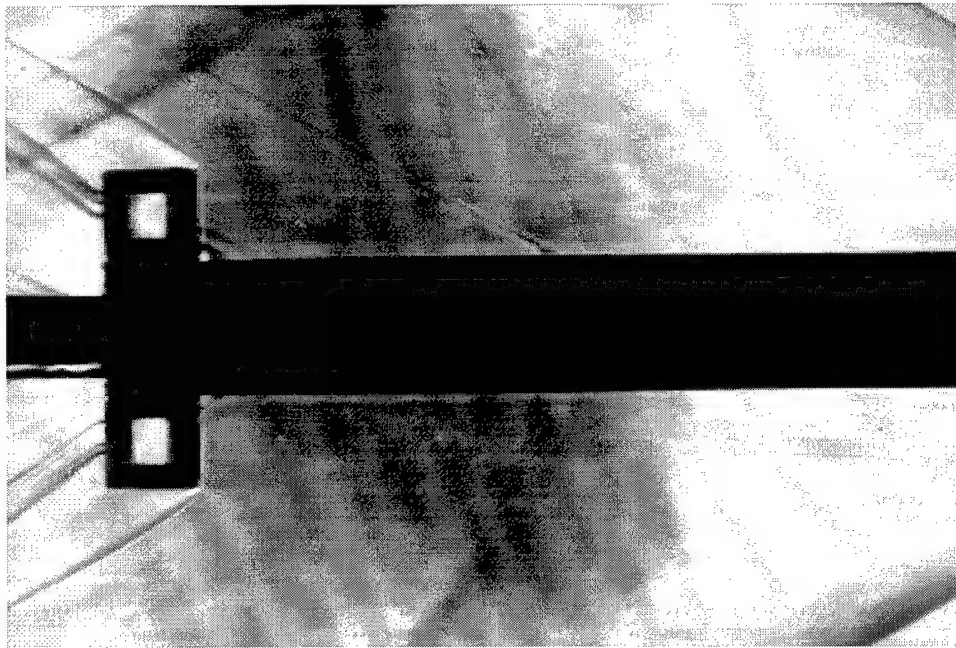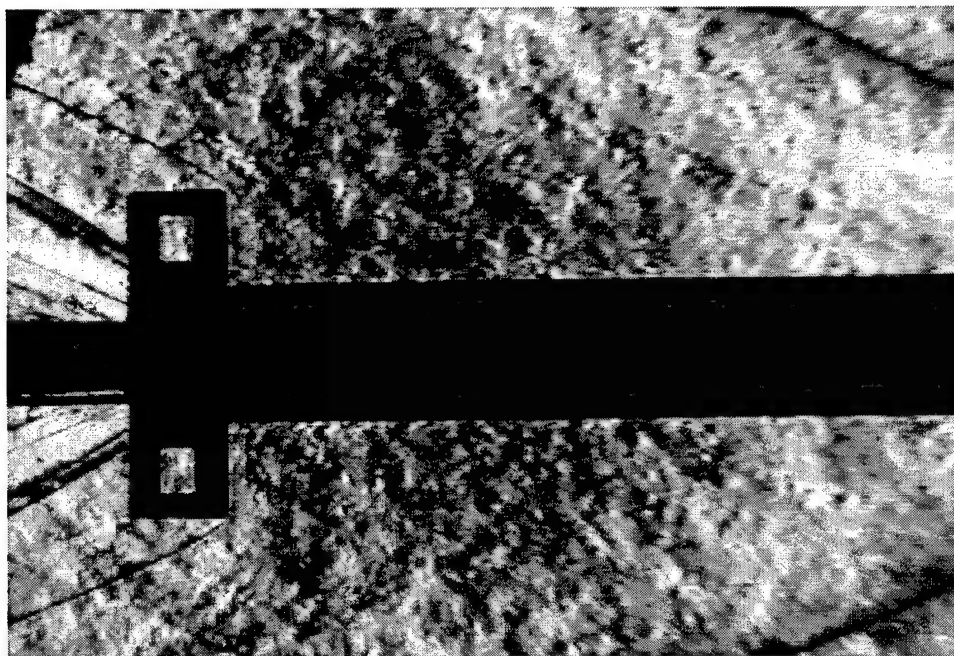
Figure 46. Slotted Fin Spark Schlieren Image at Mach 2.86
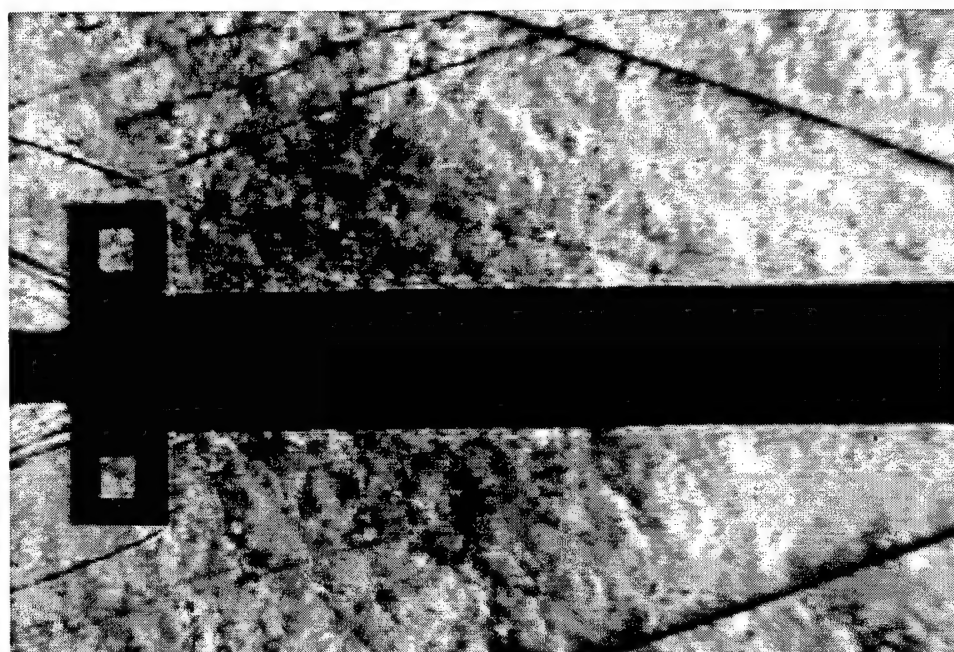
Figure 47. Slotted Fin Spark Schlieren Image at Mach 3.83

3.5 Overall Flow field Analysis

Utilizing information from all three research methods, data were used to interpret the overall flow field characteristics which result in the unique behavior of WAF projectiles. Because testing was performed primarily at zero angle of attack, this analysis only covers a small portion of the total flight envelope. PSP and schlieren tests at Mach 2.86 were conducted on the solid fin at +5.0 and -5.0 degrees angle of attack, with negligible effects on the fin pressure and density distributions. This analysis is therefore assumed to adequately cover angles of attack up through this range.

3.5.1 Solid Fin

Concave fin pressures shown in part [e] of Figure 19 are key to understanding WAF rolling moments. On the leading edge of the fin, pressures on the order of free stream stagnation are expected and observed. Immediately following the leading edge is a lip of low pressure, which persists through approximately 10% of the chord length. This was most likely caused by an expansion region which follows the detached shock in front of the fin. The location and detached nature of this shock may be noted in Figure 36, at a lower Mach number. Following the lip of low pressure is a triangular region of high pressure, which is evident in all tests of both models. This region resulted from the compressive effects of fin curvature. On the bottom portion of the concave fin another region of high pressure results from boundary layer compression. The interaction of fin and fuselage boundary layers results in a compression that increases in size and strength during the entire chord length. On the aft portion of the concave fin, flow diverges away from the mid-span position. This results from the triangular region of high pressure that was common to all Mach settings.

The convex fin pressures displayed in part [f] of Figure 19 show the effects of a vortex generated at the intersection of the body and leading edge of the fin. The vortex is displayed well in Figures 16, 17, and 18, which have been adjusted to visualize primary flow structures, such as the

59

vortex. The structure grows in size and strength as it proceeds downstream at varying angles from the body, ranging between 25 and 45 degrees. The effects of the vortex appear to diminish at mid-span, as the fin location diverges away from the vortex position. That is, at mid-span, the fin begins to curve in the opposite direction when compared to the curvature adjacent to the missile body. This direction of curvature is opposite of the vortex location, resulting in reduced vortex pressure effects. Schlieren images confirm the presence of the vortex, best seen in Figure 36. A tubular structure may be seen on the top and bottom fins, exiting at approximately mid-span, right where PSP data indicate the vortex exits. Increasing Mach appears to decrease the angle at which the vortex departs the fuselage, ranging from 45 degrees at Mach 2.15 to approximately 25 degrees at Mach 3.83. Oil flow patterns in Figure 29 also confirm the presence of the vortex. The convex fin stagnation region is similar to the concave side of the fin. A small region of boundary layer compression also occurs on the concave side of the fin, though not as dramatic.

The body of the missile is dominated by shock interactions from each fin. The lamda shocks, evident from schlieren imaging and oil flow visualization, intersect between the fins at approximately the fin leading edge location. The lambda shock, when viewed with the oil flow images of Figures 30, 31, and 32, is more normal on the convex side of the fin, which contributes to the vortex structure. The shock is more oblique, or weaker, on the concave side. Seen aft of the lambda shock, but just prior to the fin, are the remnants of the detached fin shock striking the fuselage. This is seen most clearly in the oil flow figures.

Results found with measurement techniques matched hot-wire, pitot, and CFD data measured in References [15,28]. This helps validate the single-fin assumption used in these studies.

3.5.2 Slotted Fin

The slotted fin flow regime was found to be very similar to the solid fin, despite the presence of the slot. On the concave side of the fin, the high pressures normally caused by fin curvature were exhausted to the convex side. This effect may be viewed in Figure 42. The same concave leading edge lip of low pressure may be seen in each slotted fin PSP image. Boundary layer compression also occurred on the bottom of the fin, in a similar manner to the solid fin. But because the fin chord length was slightly longer, the compression region increased, which increased the rolling moment contribution of the fin. The presence of the slot did not appear to affect the pressure distribution on the aft portion of the concave fin. But the momentum flux that resulted from pressure relief allowed flow to proceed directly to the aft portion of the fin, without diverging like the solid fin. Comparison of oil flow patterns in Figures 30 and 33 reflect these descriptions.

The convex fin pressure distribution was relatively unaffected by the presence of the slot. Momentum relief from the concave side of the fin appeared to press the vortex away from the fin surface, preventing it from affecting the pressure distribution on the aft portion of the fin. The vortex was not entirely dispersed, however. It may be viewed in slotted fin schlieren images, such as Figure 45. Evidence of momentum flux may also be viewed in Figure 33, where a triangular region of oil has been dispersed on the aft, central portion of the fin.

The flow field on the body was also undisturbed by the slot. The longer chord length of the slotted missile increased the distance over which shocks were interacting, but this did not affect the fins. Because of the supersonic velocities between fins, it was unlikely that the flow field in this region was disturbed by the slot.

61

Chapter 4 - Conclusions and Recommendations

This study builds on a wealth of past WAF research, exhaustively studying this projectile in the fin region. The experimental goals of the study were chosen to fill the gaps in previous research. The first goal was to obtain continuous pressure data about the fins. Second, flow field characteristics needed to be obtained on the three-dimensional models, verifying that flow field properties about a single-fin model were qualitatively identical. Third, qualitative velocity measurements were required for the fin region on the three-dimensional models. Also, verification was required for the PSP data. Specifically, if the PSP data were capturing the relevant pressure profiles about the fin, then this data should integrate and yield rolling moments similar to those obtained in previous studies. All of these goals were accomplished successfully over the largest Mach number range possible.

The pressure data predicted by CFD compared well to data observed with PSP. Future air-to-air or other guided WAF applications will require this information for accurate guidance and control of the missile. The PSP data was intended to capture this pressure field on the WAF. But the study also needed to resolve whether or not the pressure field was causing the rolling moment magnitudes and roll-off rates observed in experimental data. When PSP data were integrated, the same rolling moment trends were observed, validating the data against other wind tunnel and ballistics studies.

Velocity profiles in the WAF vicinity revealed some information about the pressure field, and added knowledge of three-dimensional WAF behavior. Oil displacements indicated regions of higher pressure, which was evident behind shocks and in boundary layer compressions. The velocity data observed in the single-fin studies of References [1,28] matched well with the results from the three-dimensional model configurations of the present study. This validates that area of research for zero angle of attack.

62

Some information was not revealed in this study. The studies in Reference [31] obtained schlieren images of ballistic WAF projectiles, observing turbulent "bursts" over the length of the model. The study hypothesized that this could be due to intermittent pockets of laminar and turbulent flow over the body caused by the rolling motion of the model. The current study of a fixed model helped validate this hypothesis, as these bursts were not witnessed. Though WAF behavior has been investigated exhaustively, future WAF studies might examine a free-spinning model so that all viscous effects might be observed.

Future ballistics testing might consider applying PSP to the models. The technique would not be difficult to employ as long as the PSP layer is durable enough to survive the gas-gun launch. When used in an instrumented gun range, "air-off" data could be taken with the model suspended before the excitement laser, ensuring that it lies at the same angle of rotation as the free-flight position. During launch, the "air-on" data could be taken by exciting the PSP with a short duration, nano-pulsed laser. A similar laser was used briefly in the present research, using a 10 ns burst of light to take images.

This study examined a wide range of Mach configurations for solid and slotted WAF projectiles. The configurations examined were compared to past studies where possible, with good agreement obtained. The study also validates the concept that PSP technology can be used to derive aerodynamic force coefficients. As PSP science grows, so will the tools available to the experimental engineer. When combined with mature flow analysis tools such as schlieren photography and oil flow visualization, experimentation allows the engineer to explore the aerodynamic flow field in ways never before possible.

Bibliography

[1] Abate, G. L. and C. Berner. "Wind Tunnel Measurements On Wrap-Around Fins at Mach 2.06," AIAA-94-3499, August, 1994.

[2] Abate, G. L. and W. H. Hathaway. "Aerodynamic Test And Analysis of Wrap Around Fins With Base Cavities," AIAA 94-0051, January, 1994.

[3] Abate, G. L. and G. L. Winchenbach. "Aerodynamics of Missiles with Slotted Fin Configurations," AIAA 91-0676, January, 1991. Aeromechanics Division, Air Force Armament Laboratory, Eglin AFB, FL.

[4] Abate, G. L. and G. L. Winchenbach, "Analysis of Wrap-Around Fin and Alternative Deployable Fin Systems for Missiles." AGARD Conference On Flight Vehicle Integration, Ankara, Turkey, October 1995.

[5] Asrar, W., M. F. Baig and S. A. Khan. "Chaos in WAF Projectile Motion," AIAA 96-0066, January, 1996.

[6] Auman, L. M. *The Aerodynamic Characteristics of Production MLRS Wrap-Around Fins*. Technical Report RD-SS-92-10, U. S. Army Missile Command, Redstone Arsenal, AL, August 1992.

[7] Beckwith, T. G., R. D. Marangoni and J. H. Lienhard. *Mechanical Measurements* (Fifth Edition). Addison-Wesley, 1993.

[8] Bowersox, R. D. W. "Refractive Optical Flow Visualization Techniques." In Schetz, J. A. and A. E. Fuhs, editors, *Handbook of Fluid Dynamics and Fluid Machinery*, Volume II, pages 1022–39, John Wiley and Sons, Inc., 1996.

[9] Dahlke, C. W. *Experimental Investigation of Several Wraparound Fins On Bodies of Revolution From Mach 0.3 to 1.3*. Technical Report RD-TM-71-12, U. S. Army Missile Command, Redstone Arsenal, AL, September 1971.

[10] Daniels, P. and S. R. Hardy. *Roll-Rate Stabilization of A Missile Configuration With Wrap-Around Fins In Incompressible Flow*. Technical Report TR-3346, Naval Surface Weapons Center, December 1975.

[11] Donovan, J. F., M. J. Morris, A. Pal, M. E. Benne and R. C. Crites. "Data Analysis Techniques for Pressure- and Temperature-Sensitive Paint," AIAA 93-0176, January, 1993.

[12] Edge, H. L. "Computation of the Roll Moment Coefficient For A Projectile With Wrap-Around Fins," AIAA 93-0499, January, 1993.

[13] Gruber, M. R., A. S. Nejad and L. P. Goss. "Surface Pressure Measurements in Supersonic Transverse Injection Flowfields," AIAA 97-3254, July, 1997.

[14] Hodges, D. A. *Static Stability Test of A Full Scale AVCO Assault Breaker Model*. Technical Report AEDC-TSR-80-P53, Arnold Engineering Development Center, July 1980.

[15] Huffman, R. E., C. P. Tilmann, T. A. Buter and R. D. W. Bowersox. "Experimental Investigation of the Flow Structure In the Vicinity of A Single Wrap-Around Fin at Mach 2.9," AIAA 96-2450, June, 1996.

[16] Martin, T. A. and D. J. Spring. *Wind Tunnel Test Results for the DCAT Missile At Mach*

Numbers From 0.64 to 2.50. Technical Report RD-73-27, U. S. Army Missile Command, Redstone Arsenal, AL, October 1973.

[17] Mikhail, A. G. "Roll Damping For Finned Projectiles Including: Wraparound, Offset, and Arbitrary Number of Fins," AIAA 93-3460, August, 1993.

[18] Morris, M. J. and J. F. Donovan. "Application of Pressure- and Temperature-Sensitive Paints to High-Speed Flows," AIAA 94-2231, June, 1994.

[19] Morris, M. J., J. F. Donovan, J. T. Kegelman, S. D. Schwab and R. L. Levy. "Aerodynamic Applications of Pressure-Sensitive Paint," AIAA 92-0264, January, 1992.

[20] Pope, R. L. and R. E. Dudley. *Flight Tests of the MKIV Wrap Around Fin Configuration*. Technical Report WSRL-0252-TR, Weapons Systems Research Laboratory, Australia, January 1982.

[21] Regan, F. J. *Supersonic Magnus Measurements of the 10-Caliber Army Navy Spinner Projectile With Wrap-Around Fins*. Technical Report NOLTR 70-211, U. S. Naval Ordnance Laboratory, October 1970.

[22] Robinson, M. L. and C. E. Fenton. *Static Aerodynamic Characteristics of a Wrap-Around Fin Configuration With Small Rolling Moments At Low Incidence*. Technical Report WRE-TN-527 (WRD), Australian Defence Scientific Service, Weapons Research Establishment, November 1971.

[23] Ruyten, W. M. "Correcting Luminescent Paint Measurements For Self-Illumination." In *ICIASF '97 Record*, pages 3–10, 1997.

[24] Sellers, M. E. *A Comparison Of An AEDC and a Russian Developed Pressure Sensitive Paint in the AEDC Propulsion Wind Tunnel 16T*. Technical Report AEDC-TR-95-18, Arnold Engineering Development Center, 1995.

[25] Sellers, M. E. *Demonstrations Of A Pressure Sensitive Paint Data System in the AEDC Propulsion Wind Tunnel 16T*. Technical Report AEDC-TR-95-8, Arnold Engineering Development Center, 1995.

[26] Sellers, M. E. *A Wind Tunnel Test Demonstrating The Capabilities Of Pressure Sensitive Paint*. Technical Report AEDC-TSR-95-P23, Arnold Engineering Development Center, 1995.

[27] Swenson, M. W., G. L. Abate and R. H. Whyte. "Aerodynamic Test And Analysis of Wrap-Around Fins At Supersonic Mach Numbers Utilizing Design of Experiments," AIAA 94-0200, January, 1994.

[28] Tilmann, C. P. *Numerical And Experimental Investigation Of the Flowfield Near A Wrap-Around Fin*. PhD dissertation, Air Force Institute of Technology (AU), Wright-Patterson AFB, OH, 1997.

[29] Tilmann, C. P., R. E. Huffman, T. A. Buter and R. D. W. Bowersox. "Characterization of the Flow Structure in the Vicinity of A Wrap-Around Fin at Supersonic Speeds," AIAA 96-0190, January, 1996.

[30] Varner, D. R. *Pressure Sensitive Paint Measurement On A Rotor*. MS thesis, Naval Postgraduate School, 1995.

[31] Vitale, R. E., G. L. Abate, G. L. Wichenbach and W. Riner. "Aerodynamic Test and Analysis of A Missile Configuration With Curved Fins," AIAA 92-4495, August, 1992.

[32] Vlajinac, M. *Wind Tunnel Measurements of the Aerodynamic Characteristics of the 2.75 Wrap Around Fin Rocket Using A Magnetic Suspension System*. Technical Report TR 150, Massachusetts Institute of Technology Aerophysics Laboratory, December 1968.

[33] Washington, W. D. "Experimental Investigation of Rolling Moment for A Body-Wing-Tail Missile Configuration with Wrap Around Wings and Straight Tails at Supersonic Speeds," AIAA-83-2081, August, 1983.

[34] Winchenbach, G. L., R. S. Buff, R. H. Whyte and W. H. Hathaway. "Subsonic And Transonic Aerodynamics of A Wraparound Fin Configuration," *Journal of Guidance and Control*, *November-December* 6,:627–32 (1986).

APPENDIX A - PSP Reduction Algorithms

A.1 PSP Reduction Code Algorithms

Algorithms are presented for future PSP applications. The following codes were written in the C programming language. PSP images were in a 16-bit, unsigned short format. The unsigned format maximizes the resolution of the CCD A/D converter, as photons are recorded in quanta, and do not have a positive or negative sign.

A.1.1 Algorithm For PSP.EXE Pressure Reduction Code

- Iterate over pixel row, j
  - Iterate over pixel column, i
    * Read in air-on pixel photoelectric count
- Iterate over pixel row, j
  - Iterate over pixel column, i
    * Read in air-off pixel photoelectric count
- Iterate over pixel row, j
  - Iterate over pixel column, i
    * Read in background pixel photoelectric count
- Iterate over pixel row, j
  - Iterate over pixel column, i
    * Subtract background pixel photoelectric count from air-on photoelectric count
    * Subtract background pixel photoelectric count from air-off photoelectric count
    * Divide air-off photoelectric count by air-on photoelectric count (I_0/I)
- Read in test atmospheric pressure in kPa
  - $(I_0/I)_{p_{atm}} = 0.23162 + 9.5716 \times 10^{-3} P_{atm} - 2.7612 \times 10^{-5} P_{atm}^2 + 9.1774 \times 10^{-8} P_{atm}^3$
  - Iterate over pixel row, j
    * Iterate over pixel column, i
      · Divide ratioed image (I_0/I) pixel by $(I_0/I)_{p_{atm}}$
- Iterate over pixel row, j
  - Iterate over pixel column, i
    * Pixel pressure = -20.485 + 76.816 (I_0/I) + 57.238 $(I_0/I)^2$ - 14.247 $(I_0/I)^3$
- Iterate over pixel row, j
  - Iterate over pixel column, i
    * Save pixel pressure in IEEE float format

67

A.1.2 Algorithm For IMAGE_AVG1.EXE Image Averaging Code

- Iterate up to total number of images, k
  - Iterate over pixel row, j
    - Iterate over pixel column, i
      - Read in pixel photoelectric count, sum photoelectric count over k images
- Iterate over pixel row, j
  - Iterate over pixel column, i
    - Divide total pixel count by k, save average pixel value in IEEE float format

A.2 Derivation of Finite Pixel Element Rolling Moment Contribution

Consider the pressure vector **P** acting at a point on a curved fin, as in Figure 48. The angle of fin curvature at this point is given by μ.
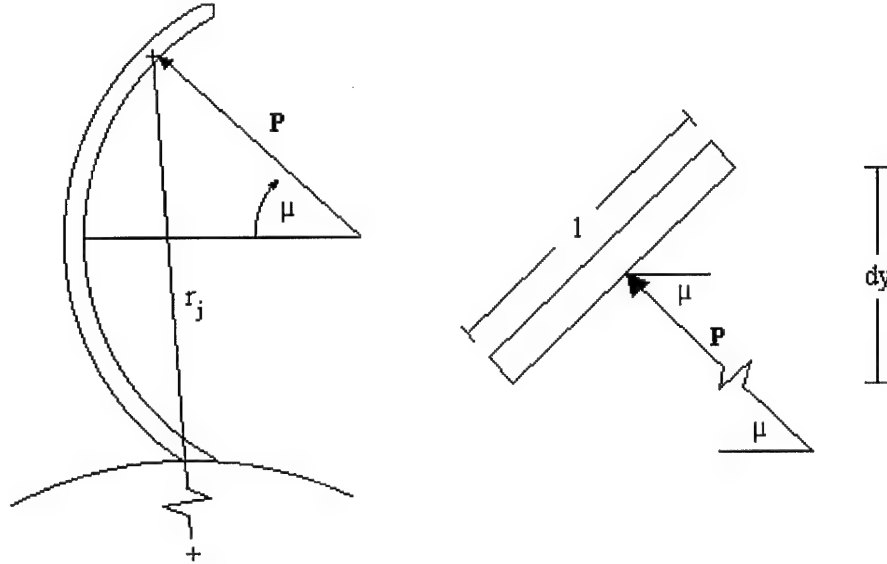

Figure 48. Pressure Acting On A WAF

When zooming into a specific pixel of length l, the variation of μ over the pixel is negligible. Given the pixel depth in the j-direction, dy, the value of l is found knowing that the pressure acts normal to the surface:

$$\sin(90 - \mu) = \frac{dy}{l} \tag{7}$$

68

$$l = \frac{dy}{\cos \mu} \tag{8}$$

The pixel length in the i-direction, dx, is also known from camera data. This value is constant on all points of the fin when oriented in the same fashion as PSP images. Knowing this, the force acting on the finite area of the fin is given by:

$$F_{i,j} = P_{i,j} l \, (dx) \tag{9}$$

$$F_{i,j} = \frac{P_{i,j} \, (dx) \, (dy)}{\cos \mu} \tag{10}$$

The component of the pressure force acting tangentially to the missile center line causes a WAF rolling moment. This is given by:

$$F_{t_{i,j}} = F_{i,j} \cos \mu \tag{11}$$

When multiplied by the distance from the center line of the missile to the pixel, r_j, the rolling moment is given by

$$L_{i,j} = F_{t_{i,j}} r_j \tag{12}$$

Which is re-written as:

$$L_{i,j} = P_{i,j} \, (dx) \, (dy) \, r_j \tag{13}$$

When all moment components are summed over the fin, the total contribution is given by equation 14:

$$L = \sum_{j=1}^{j \max} \sum_{i=1}^{i \max} [P_{i,j} \, (dx) \, (dy) \, r_j] \tag{14}$$

69

APPENDIX B - Error Analysis

Error, or scatter, exists in any experimental work. Analysis of scatter was performed for the non-dimensionalized PSP images, rolling moment analysis, and schlieren images. In all cases, the maximum error, or norm, was cited as the experimental uncertainty. Error analysis was not performed for oil flow visualization. Mach number scatter was the only uncertain parameter in these images. Error in Mach is investigated in the following section.

B.1 PSP Image Uncertainty Analysis

Inherent scatter exists in PSP calibration curve fits. The correlation coefficient, r^2, of the PSP calibration curve was 0.999, which is given by equation 15 [7]:

$$r^2 = \frac{\sum [P_{fit} - P_{meas}]^2}{\sum [P_{meas} - P_{fit}] + \sum [P_{fit} - P_{meas}]^2} \tag{15}$$

where P_{fit} is the curve-fitted pressure value and P_{meas} is the pressure measured with the Druck digital pressure controller during calibration. This yields information about error at any given point in the calibration. But because pressures were unknown during testing, the maximum norm had to be used as a guideline for pressure error. With the curve-fit data, a maximum PSP pressure error of ± 2.548 kPa resulted at any given pixel. Errors in the non-dimensionalized pressures presented in Chapter 3 required application of the Kline-McClintock uncertainty analysis [7]. The overall error in these data are represented by equation 16:

$$\left(\frac{P_{i,j}}{P_t}\right)_{error} = \sqrt{\left(\frac{\partial \left(\frac{P_{i,j}}{P_t}\right)}{\partial P_{i,j}} P_{i,j_{error}}\right)^2 + \left(\frac{\partial \left(\frac{P_{i,j}}{P_t}\right)}{\partial P_t} P_{t_{error}}\right)^2} \tag{16}$$

Which leads to the error equation:

$$\left(\frac{P_{i,j}}{P_t}\right)_{error} = \sqrt{\left(\frac{P_{i,j_{error}}}{P_t}\right)^2 + \left(\frac{-P_{i,j}}{P_t^2} P_{t_{error}}\right)^2} \tag{17}$$

This suggests that each image has an error associated with it. Calibration of the total pressure transducer resulted in a $P_{t_{error}}$ value of ± 2.068 kPa, and the value of $P_{i,j_{error}}$ was found above as

±2.548 kPa. Using the maximum norm, the largest error occurs in the Mach 2.15 slotted fin image, which is ±0.00903. Error values using equation 17 ranged from ±0.00209 to ±0.00903.

Mach number also had error because of the pressure error measurements taken in the VMT. Mach number was determined with the ratio of total to static pressure, given by the equation:

$$M = \sqrt{\frac{2}{\gamma - 1}\left[\left(\frac{P_t}{P}\right)^{\frac{\gamma-1}{\gamma}} - 1\right]} \tag{18}$$

Using equation 18, error in Mach number is given by:

$$M_{error} = \sqrt{\left(\frac{\partial M}{\partial P_t}P_{t_{error}}\right)^2 + \left(\frac{\partial M}{\partial P}P_{error}\right)^2} \tag{19}$$

This is given by equation 20:

$$M_{error} = \sqrt{\left[\frac{\left(\frac{1}{\gamma P}\right)\left(\frac{P_t}{P}\right)^{\frac{-1}{\gamma}}P_{t_{error}}}{\sqrt{\left(\frac{2}{\gamma-1}\left(\frac{P_t}{P}\right)^{\frac{\gamma-1}{\gamma}} - \frac{2}{\gamma-1}\right)}}\right]^2 + \left[\frac{\left(\frac{P_t}{P}\right)^{\frac{-1}{\gamma}}\left(\frac{-P_t}{P^2}\right)P_{error}}{\sqrt{\left(\frac{2}{\gamma-1}\left(\frac{P_t}{P}\right)^{\frac{\gamma-1}{\gamma}} - \frac{2}{\gamma-1}\right)}}\right]^2} \tag{20}$$

Application of equation 20 to each data point resulted in a maximum Mach norm of ±0.0047.

Self-illumination can be a considerable source of error in PSP measurements. This phenomena occurs when nearly-orthogonal planes coated with PSP emit and reflect off of one another. These reflected emissions are not present in the "air-off" image, and hence do not ratio out under application of the Stern-Volmer equation. Recent studies at AEDC report that self-illumination becomes critical near obtuse planar angles of 100° [23]. Angles of this magnitude were present on the convex side of the fin, at the fin-body juncture. But because the PSP layer in this region was marginal, at best, self-illumination was not a factor. All other portions of the fin region were at much shallower angles, where self-illumination does not occur.

B.2 Rolling Moment Uncertainty Analysis

The rolling moment was found using equation 21:

$$C_L = \frac{L}{q_\infty A d} \tag{21}$$

71

This equation must be broken into its constituent parts before an error analysis can be performed. The completely reduced equation is:

$$C_L = \frac{L}{\left(\frac{1}{2}\rho_\infty V_\infty^2\right)\pi r^2 \frac{r}{2}} \tag{22}$$

$$C_L = \frac{4L}{\pi \rho_\infty V_\infty^2 r^3} \tag{23}$$

The error of each part of equation 23 was found such that rolling moment coefficient error could be determined. Density errors are derived first. Test section static pressure, stagnation tank total temperature and total pressure were used to determine density, velocity, and Mach values. Static density is given by the familiar perfect gas relationship:

$$\rho = \frac{P}{RT} \tag{24}$$

Static temperature was found using the Mach relationship:

$$T = \frac{T_t}{\left(1 - \frac{\gamma-1}{2}M^2\right)} \tag{25a}$$

Substituting equation 18 into equation 25a, static temperature is re-written as:

$$T = \frac{T_t}{2 - \left(\frac{P_t}{P}\right)^{\frac{\gamma-1}{\gamma}}} \tag{26}$$

This was substituted back into the density equation, yielding:

$$\rho = \frac{P\left[2 - \left(\frac{P_t}{P}\right)^{\frac{\gamma-1}{\gamma}}\right]}{RT_t} \tag{27}$$

$$\rho = \frac{2P - P_t^{\frac{\gamma-1}{\gamma}}P^{\frac{1}{\gamma}}}{RT_t} \tag{28}$$

The Kline-McClintock error analysis is now performed on equation 28:

$$\rho_{error} = \sqrt{\left(\frac{\partial\rho}{\partial P}P_{error}\right)^2 + \left(\frac{\partial\rho}{\partial P_t}P_{t_{error}}\right)^2 + \left(\frac{\partial\rho}{\partial T_t}T_{t_{error}}\right)^2} \tag{29}$$

$$\rho_{error} = \sqrt{\left[\frac{1}{RT_t}\left(2 - \frac{1}{\gamma}P_t^{\frac{\gamma-1}{\gamma}}P^{\frac{1-\gamma}{\gamma}}\right)P_{error}\right]^2 + \left[\frac{-\left(\frac{\gamma-1}{\gamma}\right)}{RT_t}P^{\frac{1}{\gamma}}P_t^{\frac{-1}{\gamma}}P_{t_{error}}\right]^2 + \left[\frac{-\left(2P - P_t^{\frac{\gamma-1}{\gamma}}P^{\frac{1}{\gamma}}\right)}{RT_t^2}T_{t_{error}}\right]^2} \tag{30}$$

72

As mentioned previously, $P_{t_{error}}$ was ± 2.068 kPa. Static pressure error, P_{error}, was ± 0.3447 kPa. The Omega thermocouple used had a $T_{t_{error}}$ value of $\pm 0.2\,^{\circ}$C. The use of equation 30, when applied to each data point, resulted in a maximum density norm of ± 0.003325 kg/m^3. Velocity errors were found using the Mach errors found previously, and the thermocouple total temperature error. Velocity was found with the equation

$$V_\infty = M\sqrt{\gamma RT} \tag{31}$$

Substituting in equation 25a for T, this becomes

$$V_\infty = M\sqrt{\gamma R \frac{T_t}{\left(1 - \frac{\gamma-1}{2}M^2\right)}} \tag{32}$$

The error in equation 32 is given by

$$V_{\infty_{error}} = \sqrt{\left(\frac{\partial V_\infty}{\partial M}M_{error}\right)^2 + \left(\frac{\partial V_\infty}{\partial T_t}T_{t_{error}}\right)^2} \tag{33}$$

This is derived as

$$V_{\infty_{error}} = \sqrt{\left(\left[\frac{-\gamma RT_t M^2(\gamma-1)\left(1+\frac{\gamma-1}{2}M^2\right)^{-2}}{2\left(\gamma RT_t\left[1+\frac{\gamma-1}{2}M^2\right]^{3/2}\right)} + \left(\gamma RT_t\left[1+\frac{\gamma-1}{2}M^2\right]^{-1}\right)^{-1/2}\right]M_{error}\right)^2 + \left(\left[\frac{-M\gamma R\left(1+\frac{\gamma-1}{2}M^2\right)^{-1}}{2\left(\gamma RT_t\left[1+\frac{\gamma-1}{2}M^2\right]^{-1}\right)^{3/2}}\right]T_{t_{error}}\right)^2} \tag{34}$$

Using equation 34, the maximum velocity norm was $\pm 2.69 \times 10^{-5}$ m/s.

The error in rolling moment was also found using the Kline-McClintock analysis. Rolling moment was found with equation :

$$L = 4\left[\left(\sum_{j=1}^{j\max}\sum_{i=1}^{i\max}[P_{i,j}(dx)(dy)r_j]\right)_{convex} - \left(\sum_{j=1}^{j\max}\sum_{i=1}^{i\max}[P_{i,j}(dx)(dy)r_j]\right)_{concave}\right] \tag{35}$$

In this equation, rolling moment on the concave side of the fin is subtracted from the concave side, and multiplied by four. This accounts for rolling moment on both sides of the four fins. Because the values dx and dy were the same for each image (the CCD used 516 x 516 pixels), and because the same reference length was used to compute their value, this equation is simplified as:

$$L = 4\left[\left(\sum_{j=1}^{j\max}\sum_{i=1}^{i\max}\left[P_{i,j}(dx)^2 r_j\right]\right)_{convex} - \left(\sum_{j=1}^{j\max}\sum_{i=1}^{i\max}\left[P_{i,j}(dx)^2 r_j\right]\right)_{concave}\right] \tag{36}$$

73

Simplifying equation 36 can be done by assuming that the error contribution of a single fin is the same order of magnitude as all four fins:

$$L_{error} = f \left(\sum_{j=1}^{j\,\text{max}} \sum_{i=1}^{i\,\text{max}} \left[P_{i,j} \left(dx \right)^2 r_j \right] \right) \tag{37}$$

Error in rolling moment is given by

$$L_{error} = \sqrt{ \left(\frac{\partial L}{\partial P_{i,j}} P_{i,j_{error}} \right)^2 + \left(\frac{\partial L}{\partial dx} dx_{error} \right)^2 + \left(\frac{\partial L}{\partial r_j} r_{j_{error}} \right)^2 } \tag{38}$$

The derivation of rolling moment error is:

$$L_{error} = \sqrt{ \begin{array}{l} \left[\left(\sum_{j=1}^{j\,\text{max}} \sum_{i=1}^{i\,\text{max}} \left[\left(dx \right)^2 r_j \right] \right) P_{i,j_{error}} \right]^2 + \\ \left[2 \left(\sum_{j=1}^{j\,\text{max}} \sum_{i=1}^{i\,\text{max}} \left[P_{i,j} dx r_j \right] \right) dx_{error} \right]^2 + \\ \left[\left(\sum_{j=1}^{j\,\text{max}} \sum_{i=1}^{i\,\text{max}} \left[P_{i,j} \left(dx \right)^2 \right] \right) r_{j_{error}} \right]^2 \end{array} } \tag{39}$$

Now the error in pressure data at pixel (i,j) was shown to be ± 2.548 kPa. The method used to find the value of dx and dy in the program required determination of missile fuselage boundaries in the PSP image. In any given image, the boundaries were blurred by no more than one pixel on the top and bottom of the fuselage, for an error of 2 pixels. The maximum number of pixels which comprised the body in each PSP image was 199, ranging from 197 to 199. Knowing that the missile diameter was 1.905 cm (measured with a Fowler precision dial caliper, ± 0.0254 mm due to surface roughness), pixel depth was found by dividing the number of pixels by 1.905 cm. When comparing dx computed using 199 pixels to the dx value using 201 pixels, an error of ± 0.0009525 mm results. This value represents the maximum norm of dx and dy. Because dy is used to determine r_j, this value also has a maximum norm of ± 0.0009525 mm. Using equation 39, average pressures from PSP data were integrated to find errors. The maximum rolling moment norm for the solid fin was ± 0.005265 Nm. The maximum rolling moment norm for the slotted fin was ± 0.006433 Nm.

Using the errors found above, error in rolling moment coefficient may now be determined from equation 23. Maximum error percentages from dynamic pressure, ε_q, and rolling moment, ε_L, were

74

used to determine rolling moment coefficient errors:

$$C_{L_{error}} = C_L \left(1 + \varepsilon_q + \varepsilon_L\right) - C_L \tag{40}$$

This equation assumes that error in missile radius is approximately zero. Equation 40 is re-written in percentage error as:

$$\varepsilon_{C_L} = \frac{\left\|C_L \left(1 + \varepsilon_q + \varepsilon_L\right)\right| - |C_L|\|}{|C_L|} \tag{41}$$

Application of this equation resulted in a maximum norm of ±0.00994 for the solid fin, and ±0.0115 for the slotted fin. The maximum norm is not the best value over which to judge rolling moment coefficient values, as the application of equation 41 results in a large error scatter. Average rolling moment coefficient error provided more the more reasonable error values of ±0.00656 for the solid fin and ±0.00771 for the slotted fin. Appendix C contains all data in tabular form, including error values, for each rolling moment coefficient value computed. Errors are expressed in percentages.

In addition to the inherent error in the PSP measurement technique, there was error associated with the original assumptions about moment contributions of the WAF. The pressure integration technique did not include viscous contributions and their effect on rolling moment. The code used to derive rolling moments from PSP data was also used on the Mach 2.9 viscous CFD result from reference [28]. CFD pressure data were saved in a text matrix, just as the PSP data. Pressure values over the entire fin, including the leading edge, were integrated to find rolling moments. The resulting moments were 0.0022 (5.0%) larger than that computed with CFD. This small error was attributed to the viscous effects on the leading edge, and the small contribution validated the original assumption that viscous contributions were negligible.

Stagnation pressures on the leading edge lie outside of the PtOEP calibration range, and were not included in the rolling moment computations. CFD pressure estimates were integrated again without the leading edge contributions. As a result, rolling moment coefficient was underestimated by 0.011. The average rolling moment coefficient comparisons made in Chapter 3 have the same

75

roll-off rate as CFD results. This indicates that the leading edge error was not Mach-dependant. The size of this error is small when compared to the inherent error in the PSP measurement, the error which should be considered when examining the data.

B.3 Schlieren Uncertainty

Continuous wave schlieren images time-average the first derivative of density with in the flow field. Therefore, statistical errors were assumed to be small in these images. Spark schlieren images were taken assuming that the spark acted as a perfect point source at all times, located in the same position relative to the mirrors. Variations in ambient conditions resulted in spark displacement values of 0.5 cm. The effect of this offset were considered negligible. Small scratches, on the order of 1.0 mm, were present on parabolic mirrors. The mirror variations in refractive index and their effect on density variations were considered negligible.

APPENDIX C - Additional Data and Images

C.1 Tabular Data

Data are presented in tabular form for potential future comparison. Error percentages derived

in Appendix B are also placed next to measured values. Table 1 presents free stream solid fin data

from the VMT. Table 2 presents rolling moment data and error values obtained with reduction codes.

The same data are presented for the slotted fin in Tables 3 and 4.

Table 1. Solid Fin VMT Data

PSP Image	M_∞	$\pm M_{\infty_{error}}$ (%)	V_∞ (m/s)	$\pm V_{\infty_{error}}$ (%)	ρ_∞ (kg/m^3)	$\pm \rho_{\infty_{error}}$ (%)
1	2.15	0.226	525.5	5.1E-06	0.710	0.437
2	2.15	0.086	529.5	2.2E-06	1.650	0.177
3	2.15	0.101	514.6	2.6E-06	1.526	0.204
1	2.28	0.156	548.7	4.2E-06	0.722	0.342
2	2.28	0.074	533.9	2.1E-06	1.662	0.160
3	2.28	0.089	526.7	2.6E-06	1.431	0.193
1	2.41	0.000	543.9	0.0	0.812	0.322
2	2.41	0.063	562.0	1.9E-06	1.502	0.141
3	2.41	0.076	551.3	2.3E-06	1.296	0.171
1	2.86	0.000	604.1	0.0	0.653	0.143
2	2.86	0.048	598.0	2.0E-06	1.061	0.076
3	2.86	0.058	588.9	2.4E-06	0.920	0.093
1	3.25	0.000	628.6	0.0	0.619	0.122
2	3.25	0.042	630.2	2.1E-06	0.738	0.139
3	3.25	0.049	625.7	2.4E-06	0.644	0.159
1	3.50	0.000	608.9	0.0	0.891	0.079
2	3.50	0.037	623.7	2.3E-06	0.662	0.317
3	3.50	0.042	623.5	2.5E-06	0.587	0.356
1	3.83	0.033	665.2	2.1E-06	0.500	0.592
2	3.83	0.036	662.2	2.4E-06	0.453	0.734

Table 2. Solid Fin Rolling Moment Data

PSP Image	M_∞	L (Nm)	$\pm L_{error}$ (%)	C_L	$\pm C_{L_{error}}$ (%)
1	2.15	-0.046	11.30	-0.079	11.73
2	2.15	-0.052	9.86	-0.042	10.03
3	2.15	-0.048	10.72	-0.044	10.92
1	2.28	-0.053	9.92	-0.092	10.26
2	2.28	-0.092	5.72	-0.071	5.88
3	2.28	-0.074	7.13	-0.068	7.32
1	2.41	-0.032	16.01	-0.043	16.33
2	2.41	-0.041	12.58	-0.032	12.72
3	2.41	-0.036	14.34	-0.034	14.51
1	2.86	-0.031	16.41	-0.046	16.55
2	2.86	-0.032	15.94	-0.031	16.02
3	2.86	-0.028	18.06	-0.032	18.15
1	3.25	-0.038	13.86	-0.054	13.98
2	3.25	-0.032	16.32	-0.040	16.46
3	3.25	-0.016	32.32	-0.023	32.48
1	3.50	-0.017	29.94	-0.013	30.02
2	3.50	-0.025	20.75	-0.035	21.07
3	3.50	-0.024	21.51	-0.038	21.87
1	3.83	-0.016	33.29	-0.025	33.89
2	3.83	-0.022	23.35	-0.041	24.09

Table 3. Slotted Fin VMT Data

PSP Image	M_∞	$\pm M_{\infty_{error}}$ (%)	V_∞ (m/s)	$\pm V_{\infty_{error}}$ (%)	ρ_∞ (kg/m^3)	$\pm \rho_{\infty_{error}}$ (%)
1	2.15	0.227	525.5	5.1E-06	0.710	0.437
2	2.15	0.086	529.5	2.2E-06	1.650	0.177
3	2.15	0.101	514.6	2.6E-06	1.526	0.204
1	2.41	0.227	525.5	4.5E-06	0.710	0.437
2	2.41	0.086	529.5	2.0E-06	1.650	0.177
3	2.41	0.101	514.6	2.4E-06	1.526	0.204
1	2.86	0.0	604.1	0.0	0.653	0.143
2	2.86	0.048	598.0	2.0E-06	1.061	0.076
3	2.86	0.058	588.9	2.4E-06	0.920	0.093
1	3.25	0.0	628.6	0.0	0.619	0.122
2	3.25	0.042	630.2	2.1E-06	0.738	0.139
3	3.25	0.049	625.7	2.4E-06	0.644	0.159
1	3.50	0.0	608.9	0.0	0.891	0.079
2	3.50	0.037	623.7	2.3E-06	0.662	0.317
3	3.50	0.042	623.5	2.5E-06	0.587	0.356

Table 4. Slotted Fin Rolling Moment Data

PSP Image	M_∞	L (Nm)	$\pm L_{error}$ (%)	C_L	$\pm C_{L_{error}}$(%)
1	2.15	-0.052	12.42	-0.089	12.86
2	2.15	-0.042	15.19	-0.034	15.37
3	2.15	-0.050	12.77	-0.046	12.97
1	2.41	-0.057	11.17	-0.074	11.60
2	2.41	-0.073	8.70	-0.055	8.88
3	2.41	-0.047	13.46	-0.042	13.67
1	2.86	-0.062	10.26	-0.092	10.41
2	2.86	-0.052	12.28	-0.051	12.35
3	2.86	-0.020	32.18	-0.023	32.28
1	3.25	-0.038	16.28	-0.055	16.40
2	3.25	-0.055	11.27	-0.070	11.41
3	3.25	-0.041	15.38	-0.060	15.54
1	3.50	-0.061	10.28	-0.047	10.36
2	3.50	-0.055	11.41	-0.079	11.72
3	3.50	-0.039	16.09	-0.063	16.45

C.2 AFIT VMT Reynolds Number Variations

Wind tunnel Reynolds numbers varied as reservoir pressure decreased over the run. The following plots present Reynolds number variations for the solid fin and slotted fin images. The graphs shown in Figures 49 and 50 display the relative decrease of Reynolds number with increasing Mach. Reynolds numbers were based on model length.
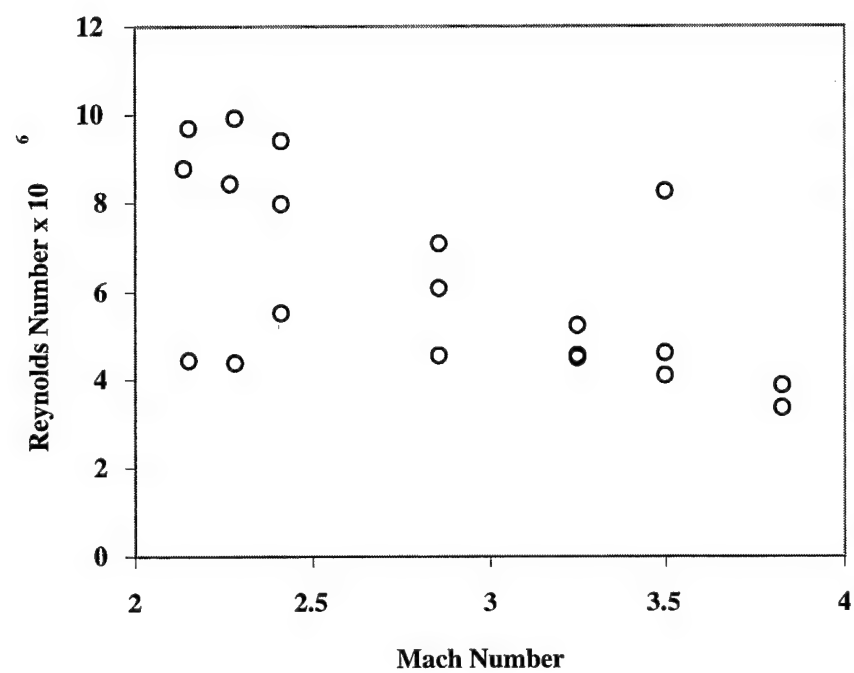
Figure 49. Solid Fin Reynolds Number Variations
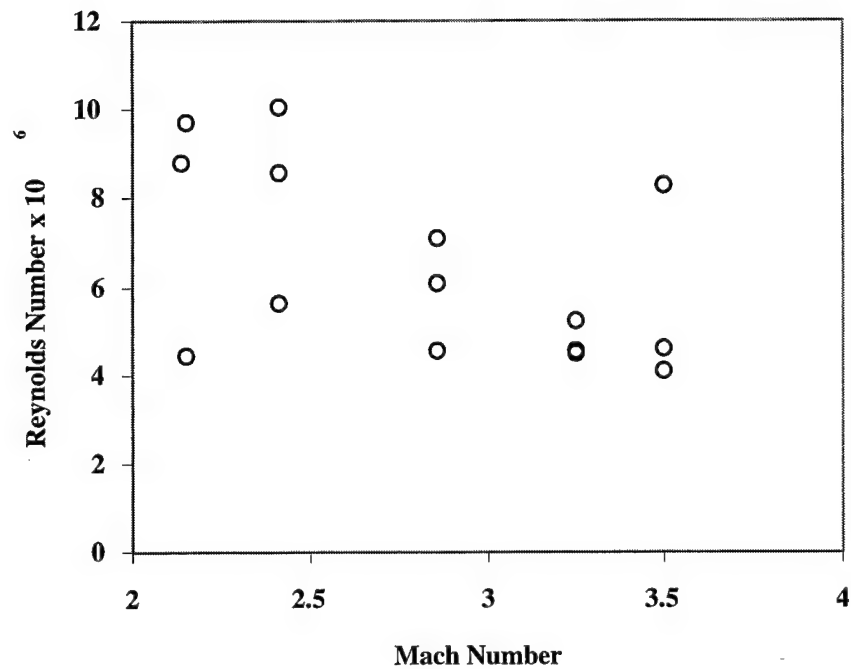
Figure 50. Slotted Fin Reynolds Number Variations

C.3 AFIT VMT Total Pressure and Temperature Variations

Wind tunnel total pressures and temperatures changed during the course of data acquisition. Figures 51 and 52 are presented to illustrate the change in stagnation parameters at Mach 2.15. As the stagnation tank inlet butterfly valve opened up, total pressure slowly rose to the desired value. Data was obtained when the tunnel started, and was taken until the supply reservoir could no longer support the tunnel Mach number setting. Because the Mach number range used in this study was high for the VMT, a constant total pressure could not be maintained due to supply reservoir volume.
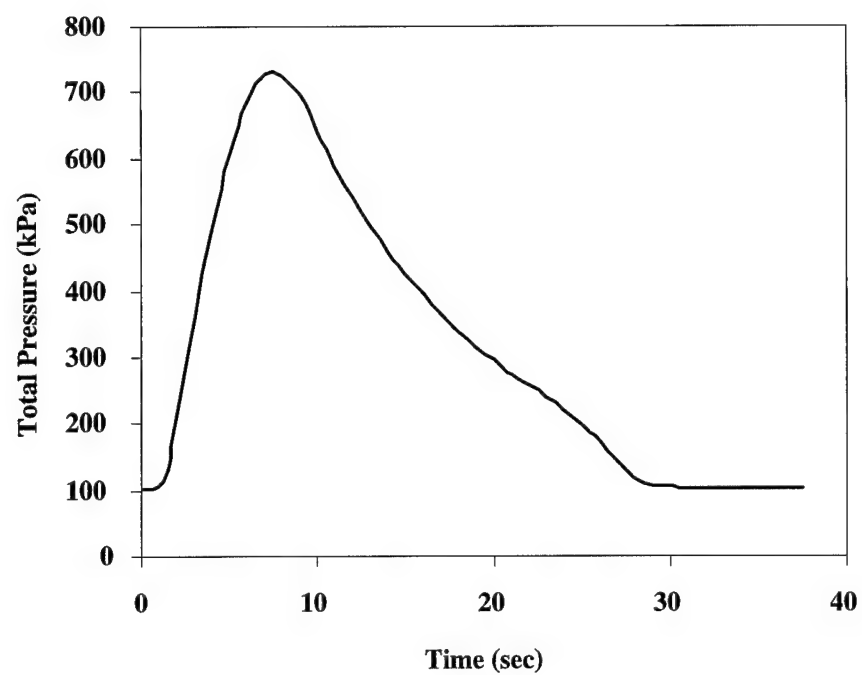
Figure 51. Total Pressure Variations at Mach 2.15

Total temperature variations were not as large, but are also presented. As the supply reservoir emptied and total pressure decreased, the perfect gas law required that stagnation temperature and density drop.
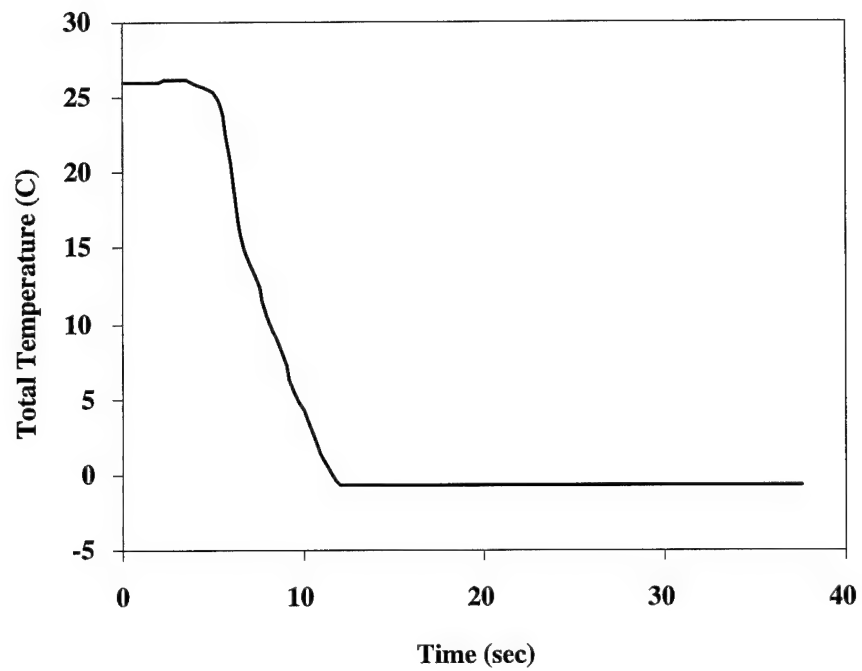
Figure 52. Total Temperature Variations at Mach 2.15

C.4 Additional Oil Flow Visualization Images

Solid fin images are presented for additional Mach numbers listed in each figure. The oil flow technique is identical to that discussed in Chapter 2.
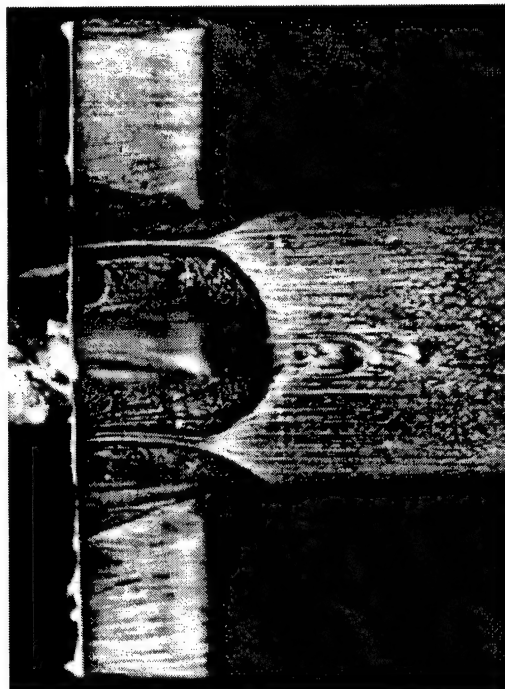
Figure 53. Solid Fin Oil Flow Pattern at Mach 2.41
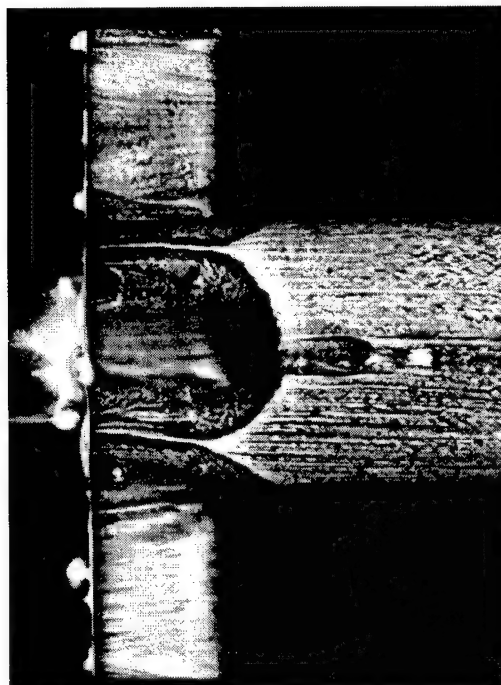
Figure 54. Solid Fin Oil Flow Pattern at Mach 3.25
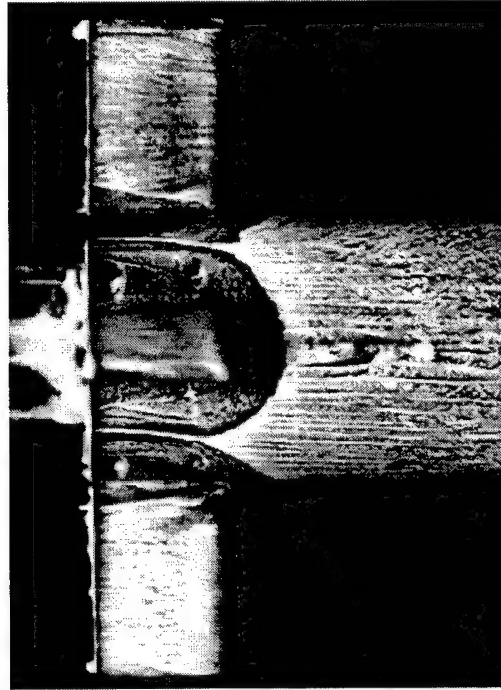
Figure 55. Solid Fin Oil Flow Pattern at Mach 3.50

Unlike PSP data, the full Mach range was explored for slotted fin oil flow patterns. The following pictures are additional to those presented in Chapter 3.

Figure 56. Slotted Fin Oil Flow Pattern at Mach 2.41
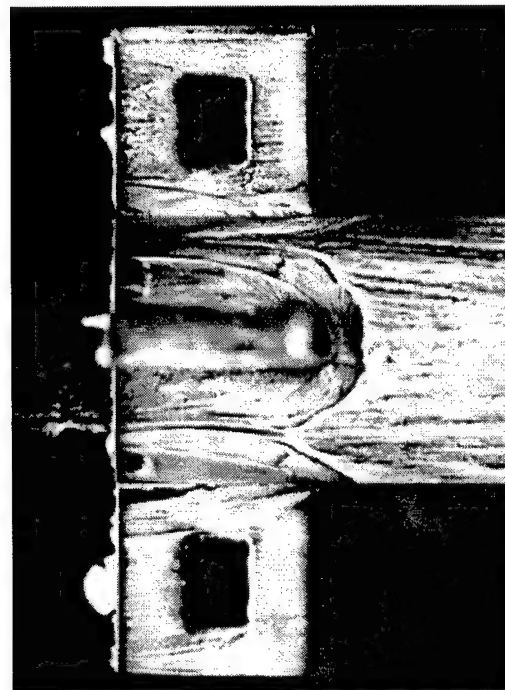
Figure 57. Slotted Fin Oil Flow Pattern at Mach 3.25
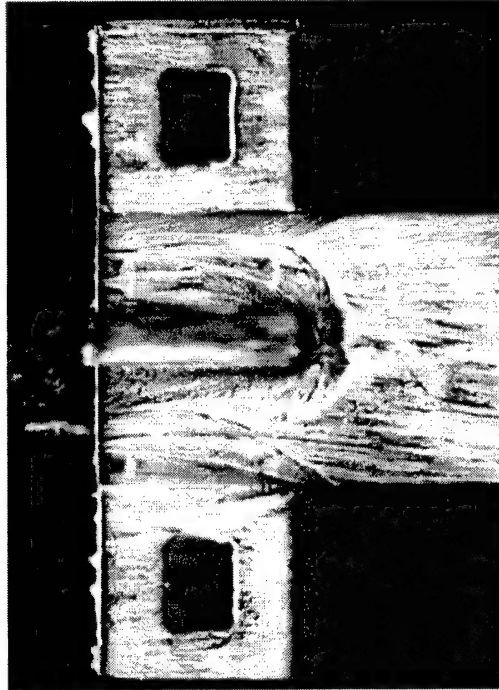
Figure 58. Slotted Fin Oil Flow Pattern at Mach 3.50

C.5 Additional Schlieren Images

Color schlieren images were attempted with the spark light source. But the color film used to take images caused a sensitivity degradation, resulting in low density gradients to be neglected. Less information was found when compared to images using a vertical knife edge. A representative color schlieren image is shown for Mach 2.15.
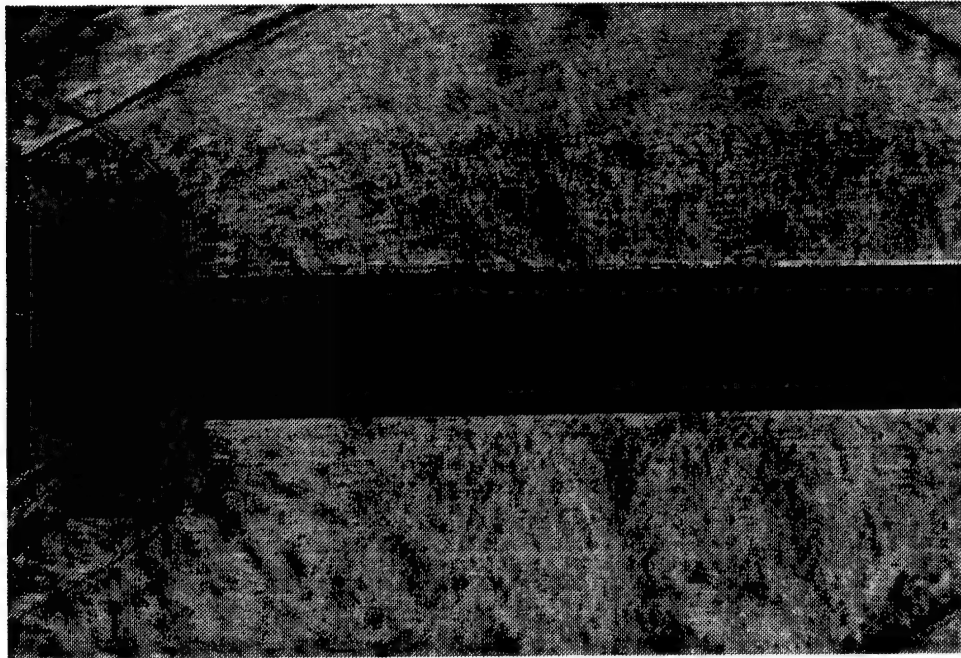
Figure 59. Slotted Fin Color Schlieren Image at Mach 2.15

Solid fin images are presented for intermediate Mach numbers not shown in Chapter 3, including continuous-wave and spark light source images. Data are presented for Mach numbers of 2.41, 3.25, and 3.50:
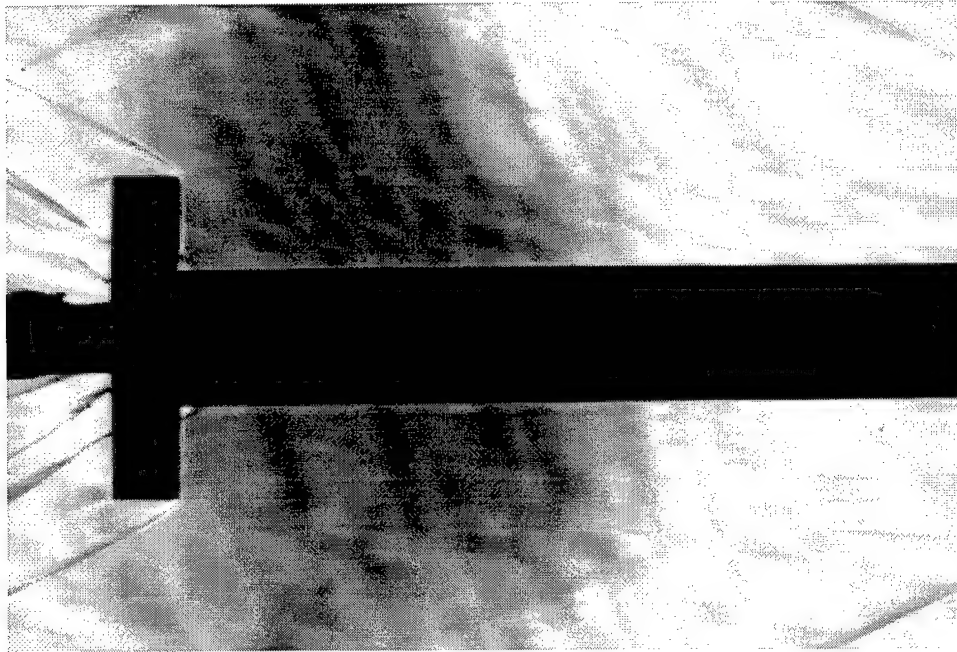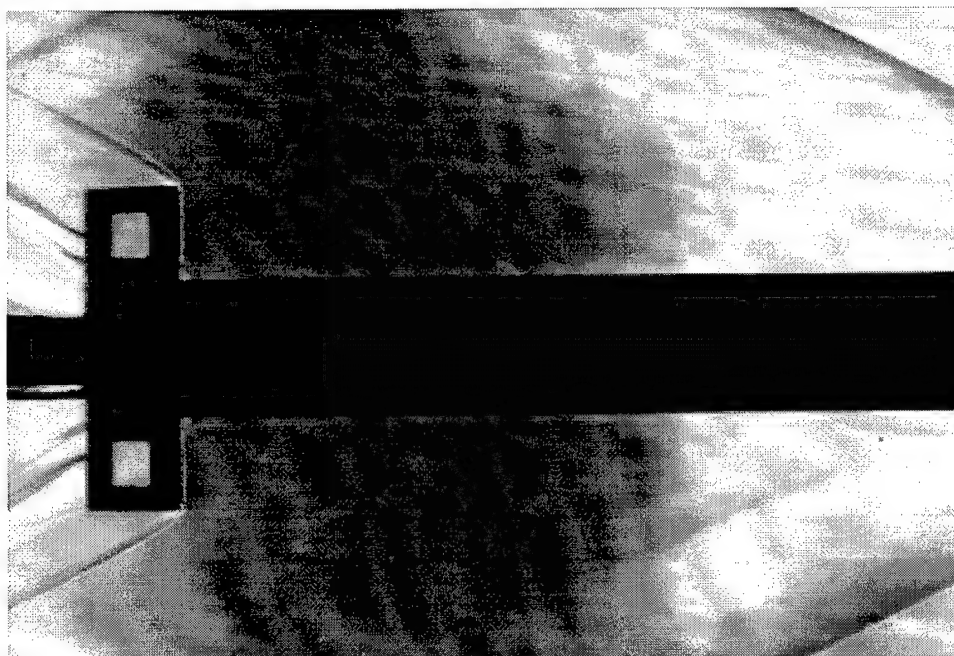
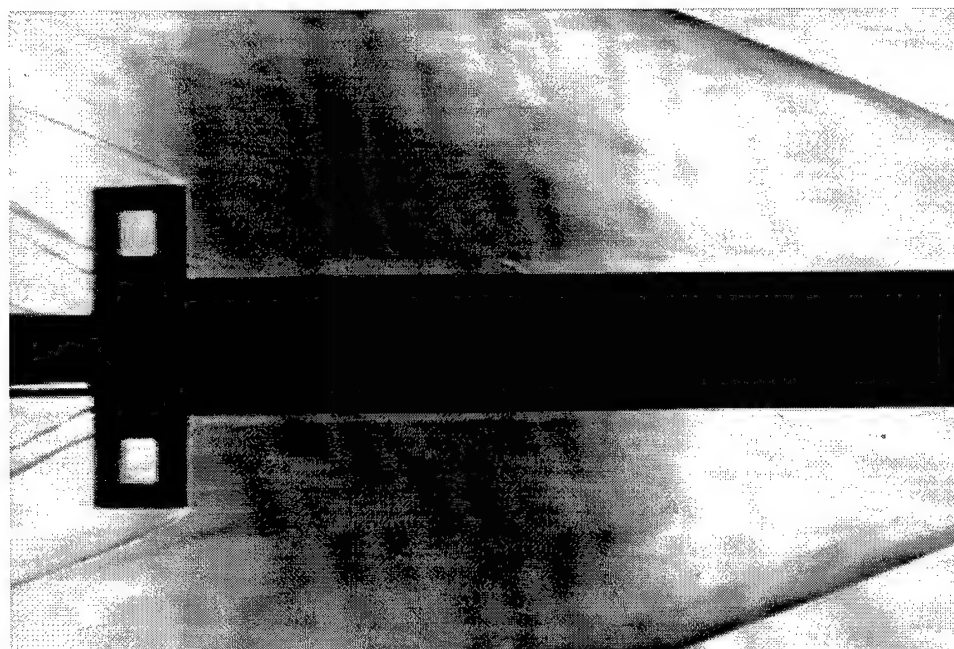Figure 60. Solid Fin Continuous-Wave Schlieren Image at Mach 2.41
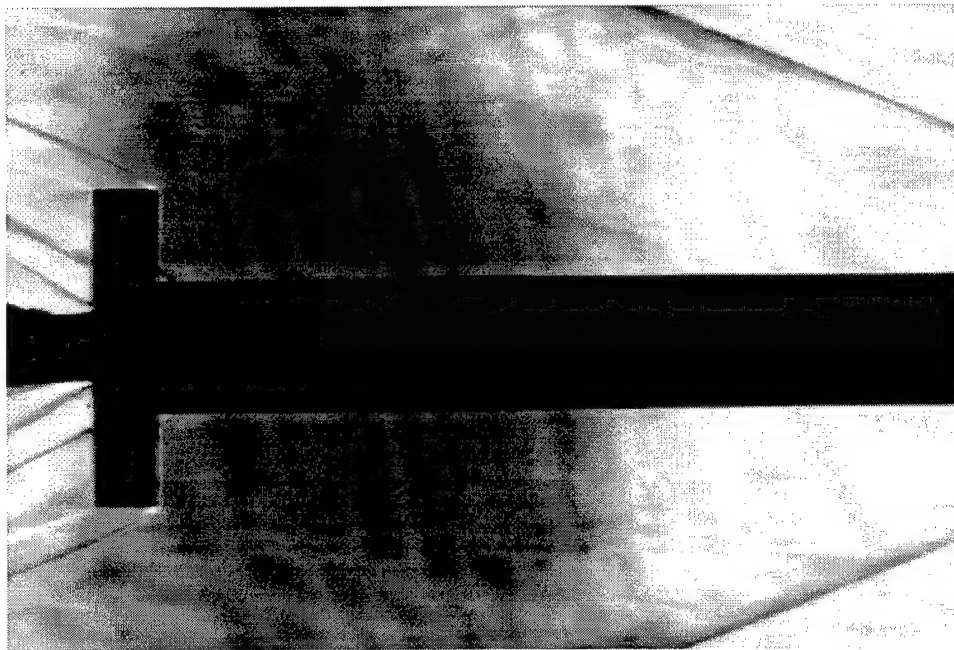
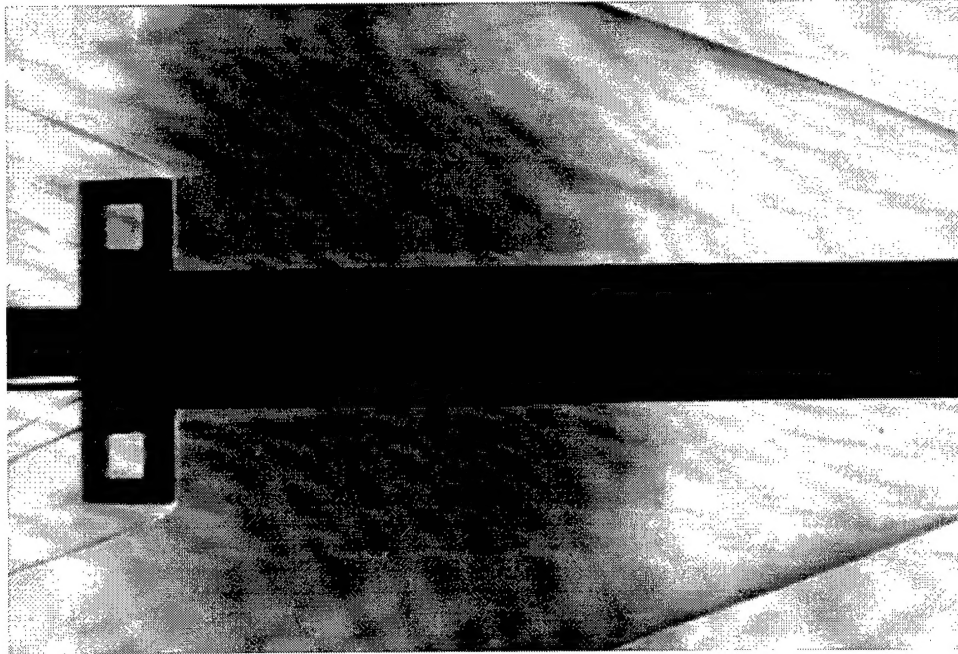Figure 61. Solid Fin Continuous-Wave Schlieren Image at Mach 3.25

89
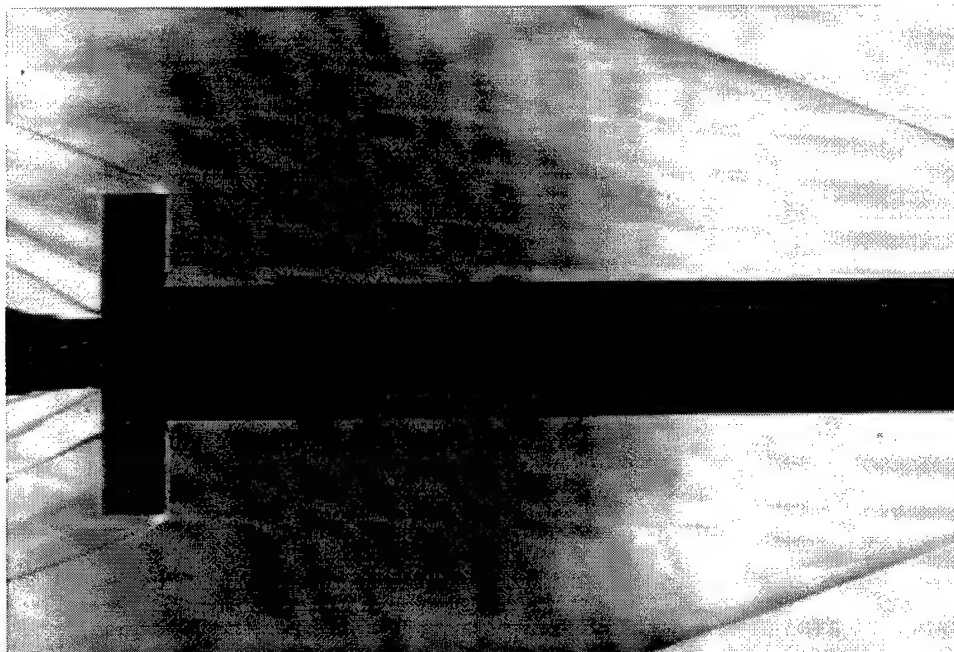
Figure 62. Solid Fin Continuous-Wave Schlieren Image at Mach 3.50
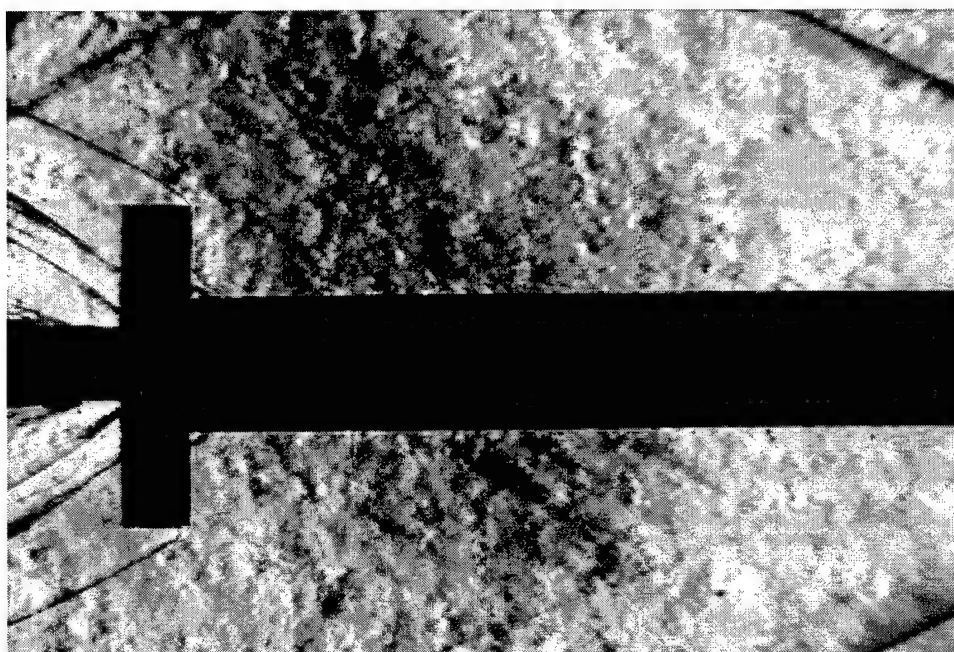
Figure 63. Solid Fin Spark Schlieren Image at Mach 2.41

90
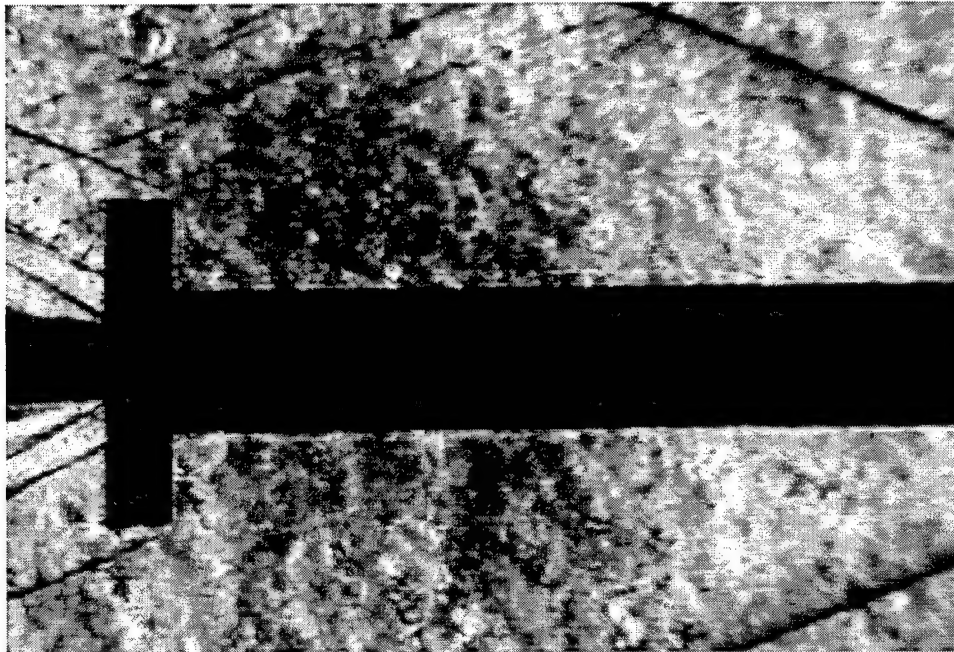
Figure 64. Solid Fin Spark Schlieren Image at Mach 3.25
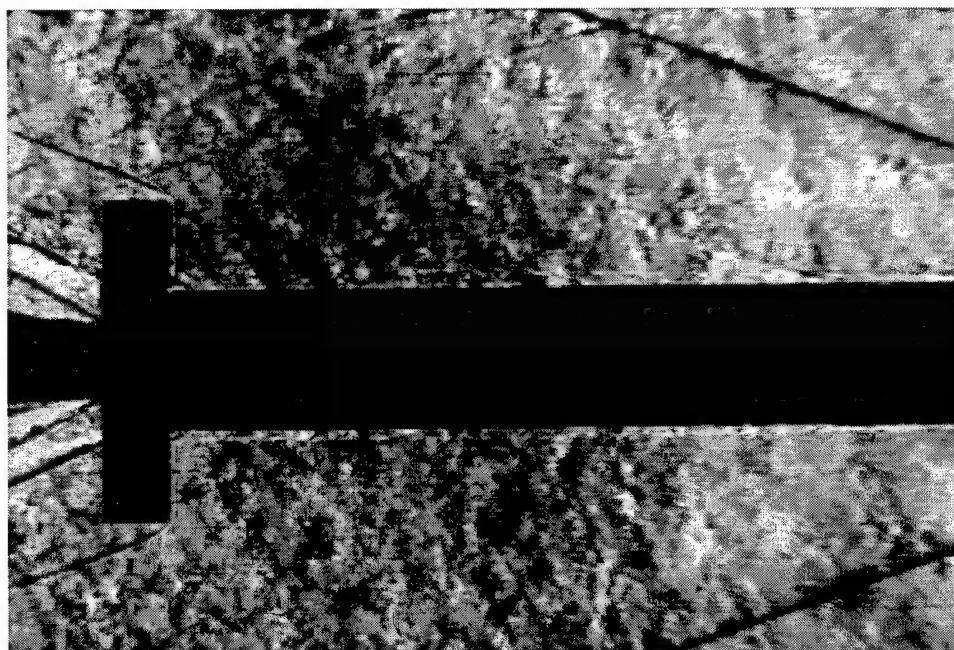
Figure 65. Solid Fin Spark Schlieren Image at Mach 3.50

Slotted fin schlieren images supplement the information presented in Chapter 3. Continuous-wave and spark schlieren images are also presented for Mach numbers of 2.41, 2.86, and 3.50:

Figure 66. Slotted Fin Continuous-Wave Schlieren Image at Mach 2.41

Figure 67. Slotted Fin Continuous-Wave Schlieren Image at Mach 3.25

Figure 68. Slotted Fin Continuous-Wave Schlieren Image at Mach 3.50
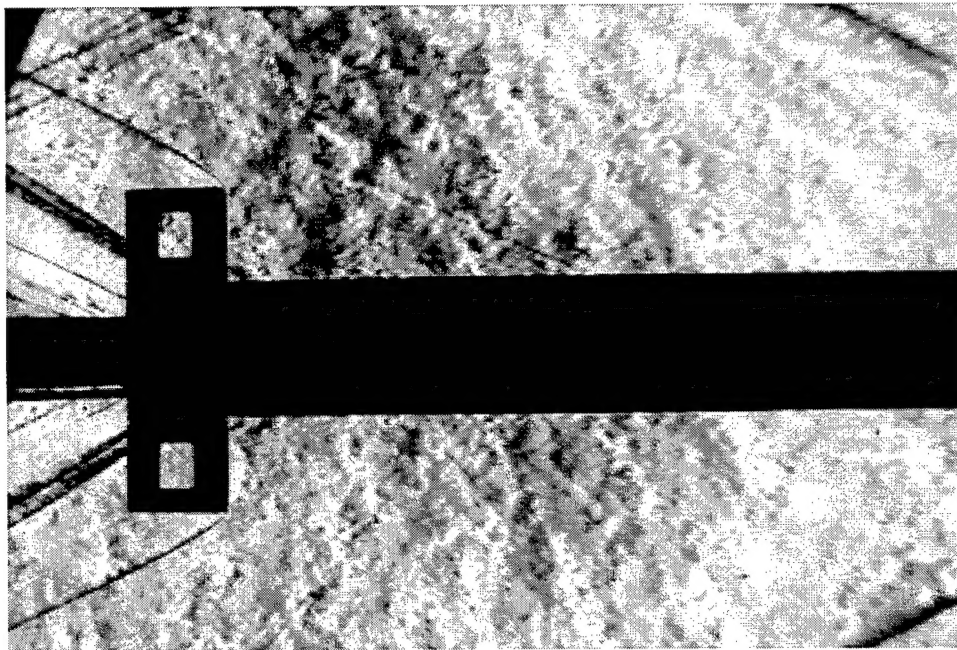
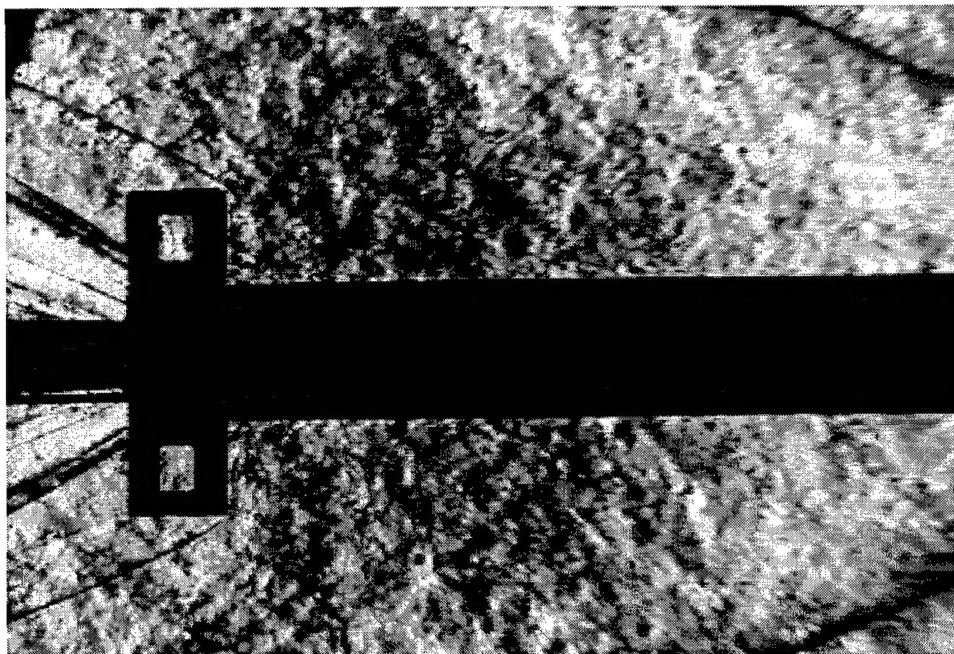Figure 69. Slotted Fin Spark Schlieren Image at Mach 2.41

93

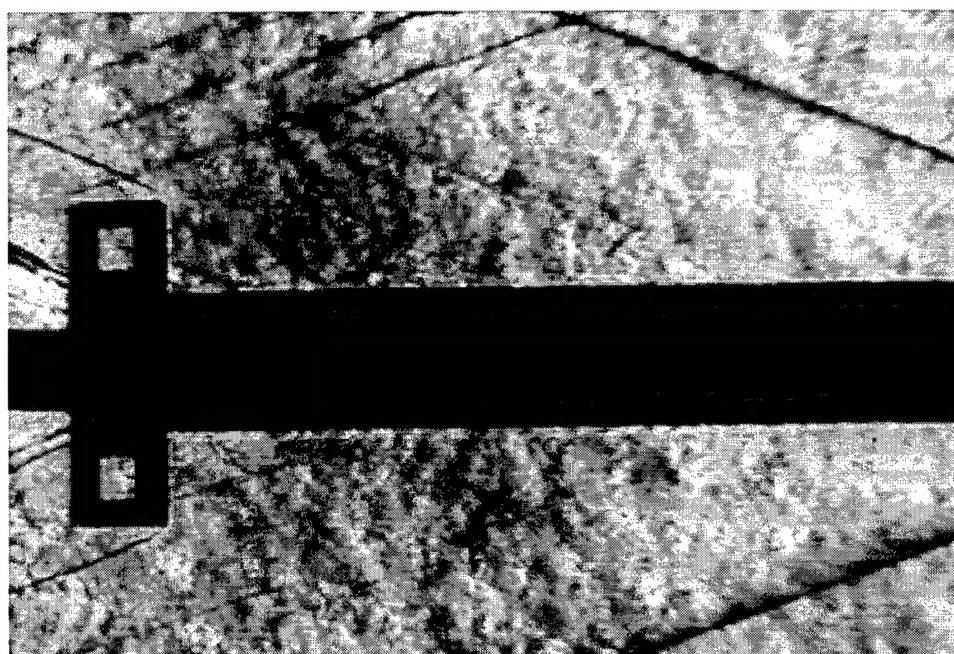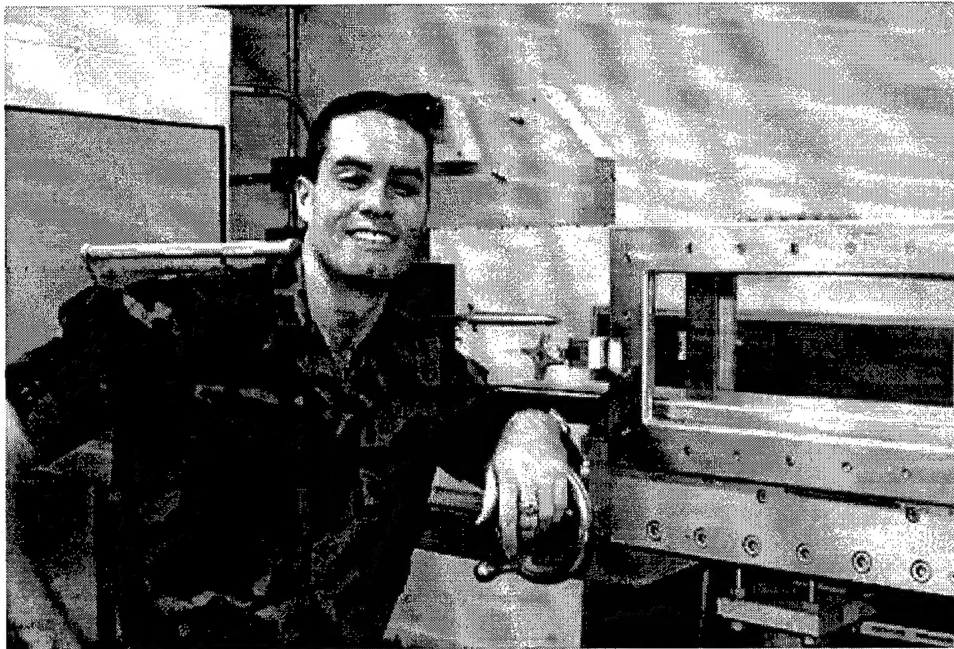Figure 70. Slotted Fin Spark Schlieren Image at Mach 2.86

Figure 71. Slotted Fin Spark Schlieren Image at Mach 3.50

Vita

Tom McIntyre was born in Dearborn, Michigan. He attended Wayne Memorial High School, in Wayne, Michigan. Tom joined the Air Force when he accepted an appointment to the United States Air Force Academy. A distinguished graduate, Tom received a Bachelor of Science Degree in Aeronautical Engineering and a minor in Spanish. He then went directly to the Air Force Institute of Technology for Aerospace Engineering. He enjoys flying, scuba diving, travelling, and the single life.

REPORT DOCUMENTATION PAGE

Form Approved
OMB No. 0704-0188

1. AGENCY USE ONLY *(Leave blank)*	2. REPORT DATE	3. REPORT TYPE AND DATES COVERED
	December 1997	Thesis

4. TITLE AND SUBTITLE
Flow Field And Loading Analysis On A Wrap-Around Fin Missile

5. FUNDING NUMBERS
C F33610-90-C-2507

6. AUTHOR(S)
Thomas C. McIntyre, Second Lieutenant, USAF

7. PERFORMING ORGANIZATION NAME(S) AND ADDRESS(ES)
AFIT/ENY
WPAFB, OH 45433

8. PERFORMING ORGANIZATION REPORT NUMBER
AFIT/GAE/ENY/97D-04

9. SPONSORING/MONITORING AGENCY NAME(S) AND ADDRESS(ES)
Mr. Gregg Abate
WL/MNA Eglin AFB, FL 32542

10. SPONSORING/MONITORING AGENCY REPORT NUMBER

11. SUPPLEMENTARY NOTES

12a. DISTRIBUTION AVAILABILITY STATEMENT
Distribution Unlimited

12b. DISTRIBUTION CODE

13. ABSTRACT *(Maximum 200 words)*
Wrap-around fin (WAF) missiles offer packaging benefits but experience rolling moments due to the curved fin design. Understanding the flow field in the vicinity of the fins is critical to future missiles. Fin pressure profiles were characterized with pressure-sensitive paint. Two rectangular four-fin constructions were tested---one solid and one with a rectangular hole (slotted fin). Tests were conducted at Mach numbers of 2.15, 2.28, 2.41, 2.86, 3.25, 3.50 and 3.83. Reynolds numbers based on missile diameter ranged from 4.0e6 to 1.3e7. The four-fin model pressure distributions agreed with CFD, verifying that a single wall-mounted fin captures relevant WAF aerodynamics. Schlieren photography and oil flow visualization supplemented pressure data, providing velocity information on the WAF surface and revealing density gradients in the fin region. Pressure sensitive paint images were edited for fin data only, saved as text matrices, and integrated with computer code to derive rolling moments and rolling moment coefficients. Solid fin data confirmed negative rolling moment magnitudes and roll-off rates measured in past experiments and in CFD predictions. Slotted fin rolling moment coefficients were slightly larger than solid fin results because of the larger fin area.

14. SUBJECT TERMS
Wrap-Around Fins, Pressure-Sensitive Paint, Rolling Moment Coefficients, Surface Pressures

15. NUMBER OF PAGES
113

16. PRICE CODE

17. SECURITY CLASSIFICATION OF REPORT	18. SECURITY CLASSIFICATION OF THIS PAGE	19. SECURITY CLASSIFICATION OF ABSTRACT	20. LIMITATION OF ABSTRACT
UNCLASSIFIED	UNCLASSIFIED	UNCLASSIFIED	UL

Standard Form 298 (Rev. 2-89) (EG)
Prescribed by ANSI Std. 239.18
Designed using Perform Pro, WHS/DIOR, Oct 94